

**NOBLE METAL CORE-SHELL  
NANOPARTICLES WITH HIGH-ENERGY  
FACETS FOR APPLICATION IN SURFACE  
ENHANCED RAMAN SCATTERING AND  
BIOSENSING**

by

**Gourab Bhattacharjee**

**Enrolment No.- PHYS05201404007**

**Saha Institute of Nuclear Physics, Kolkata**

*A thesis submitted to the*

*Board of Studies in Physical Sciences*

*In partial fulfillment of requirements*

*for the Degree of*

**DOCTOR OF PHILOSOPHY**

*of*

**HOMI BHABHA NATIONAL INSTITUTE**



**May, 2020**

# Homi Bhabha National Institute

## Recommendations of the Viva Voce Board

As members of the Viva Voce Board, we certify that we have read the dissertation prepared by Gourab Bhattacharjee entitled "NOBLE METAL CORE-SHELL NANOPARTICLES WITH HIGH-ENERGY FACETS FOR APPLICATION IN SURFACE ENHANCED RAMAN SCATTERING AND BIOSENSING" and recommend that it may be accepted as fulfilling the thesis requirement for the award of Degree of Doctor of Philosophy.

Chairman - Prof. Satyaranjan Bhattacharyya



Date: 09/09/2020

Guide/Convener - Dr. Biswarup Satpati

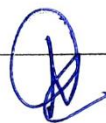


Date: 9/9/20

Co-guide - NA

Date:

Examiner - Dr. Shyamal Chatterjee



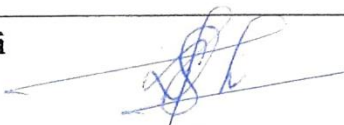
Date: 09/09/2020

Member 1 - Prof. Tapas Kumar Chini



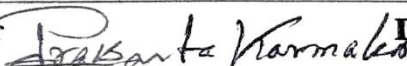
Date: 09.09.2020

Member 2 - Prof. Dulal Senapati



Date: 09.09.2020

Member 3 - Dr. Prasanta Karmakar



Date: 09/09/2020

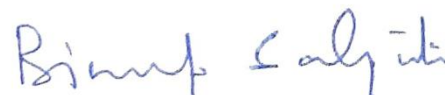
Final approval and acceptance of this thesis is contingent upon the candidate's submission of the final copies of the thesis to HBNI.

I/We hereby certify that I/we have read this thesis prepared under my/our direction and recommend that it may be accepted as fulfilling the thesis requirement.

Date: 09/09/2020

Place: Kolkata

Co-guide (if any)



Guide

## STATEMENT BY AUTHOR

This dissertation has been submitted in partial fulfillment of requirements for an advanced degree at Homi Bhabha National Institute (HBNI) and is deposited in the Library to be made available to borrowers under rules of the HBNI.

Brief quotations from this dissertation are allowable without special permission, provided that accurate acknowledgement of source is made. Requests for permission for extended quotation from or reproduction of this manuscript in whole or in part may be granted by the Competent Authority of HBNI when in his or her judgment the proposed use of the material is in the interests of scholarship. In all other instances, however, permission must be obtained from the author.



---

Gourab Bhattacharjee

## DECLARATION

I, hereby declare that the investigation presented in the thesis has been carried out by me. The work is original and has not been submitted earlier as a whole or in part for a degree / diploma at this or any other Institution / University.

*Gourab Bhattacharjee*

---

Gourab Bhattacharjee

## List of Publications arising from the thesis

### Peer reviewed journals:

1. CoreShell Gold@Silver Nanorods of Varying Length for High Surface-Enhanced Raman Scattering Enhancement.

**Gourab Bhattacharjee**, Maireyee Bhattacharya, Abhijit Roy, Dulal Senapati and Biswarup Satpati, *ACS Appl. Nano Mater.*, **2018**, 1(10), 5589–5600.

2. Core-Shell Gold @Silver Hollow Nanocubes for Higher SERS Enhancement and Non-Enzymatic Biosensor.

**Gourab Bhattacharjee**, Sumit Majumder, Dulal Senapati, Sangam Banerjee and Biswarup Satpati, *Mater. Chem. Phys.*, **2020**, 239, 122113.

### Conference proceedings:

1. Synthesis of Parallel and Antiparallel Core-Shell Triangular Nanoparticles.

**Gourab Bhattacharjee** and Biswarup Satpati, *AIP Conference Proceedings*, **2018**, 1942(1), 050112.

2. Synthesis of Core-Shell Nanocubes for Higher SERS Enhancement.

**Gourab Bhattacharjee** and Biswarup Satpati, *AIP Conference Proceedings*, **2019**, 2115(1), 030086.



---

Gourab Bhattacharjee

*To my “Family”*

## ACKNOWLEDGMENTS

Some feats cannot be accomplished alone. Similarly, this thesis would not have been accomplished without the assistance and inspiration of many people including my guide, colleagues and friends supported in many ways to the successful completion of this thesis.

First and Foremost, I would like to express my earnest gratitude to my research advisor Dr. Biswarup Satpati for his continuous encouragement, patience, inspiration and passion. His immense knowledge and experience helped me a lot during my Ph.D. course.

I am also grateful to my doctoral committee members, Prof. Satyaranjan Bhattacharyya, Prof. Tapas Kumar Chini, Prof. Dulal Senapati and Dr. Prasanta Karmakar for their useful suggestions and continuous encouragement.

Special thanks to my collaborators Dr. Maireyee Bhattacharya, Prof. Sangam Banerjee and Dr. Sumit Majumder for their helpful advices and support. I would also like to acknowledge my lab members Tanmay da, Tapas da, Abhijit, Bipasha, Suchanda, Smrutimedha, Tukai and Suman for their help and support.

A considerable amount of time of my PhD life have spent with seniors, friends and juniors. I wish to thank Achyut da, Arpan da, Sudeshna Di, Suman, Anway, Arghya, Ratnadwip, Bankim, Avik, Subha, Montu, Udit, Sandip, Astik, Sabyasachi, Abhishek, Tanmay, Moushri, Sayak, Apurba, Snehal, Bibhuti for being with me and being supportive.

I express my heartfelt gratitude and indebtedness to my parents Shri Gopal Bhattacharjee and Smt. Dipali Bhattacharjee, my sister Dipti for endless love and support. Last but not the least, I want to thank Moumita, my best friend and enemy, for being supportive and compassionate during this journey.

SINP, Kolkata

May, 2020

Gourab Bhattacharjee

# Contents

<b>Summary</b>	<b>x</b>
<b>List of Figures</b>	<b>xi</b>
<b>List of Tables</b>	<b>xiv</b>
<b>1 General introduction</b>	<b>1</b>
1.1 Introduction . . . . .	2
1.2 NPs with high energy facets . . . . .	3
1.2.1 Synthesis of noble metal NPs with high energy facets . . . . .	5
1.2.1.1 Heterogeneous nucleation . . . . .	6
1.2.1.2 Homogeneous nucleation . . . . .	8
1.2.1.3 Interfacial nucleation . . . . .	8
1.3 Core-shell NPs . . . . .	9
1.3.1 Synthesis of core-shell NPs . . . . .	10
1.3.2 Properties of core-shell NPs . . . . .	11
1.3.3 Classes of core-shell NPs . . . . .	13
1.3.4 Importance of core-shell NPs . . . . .	15
1.3.5 Core-shell HNPs . . . . .	16
1.4 Surface enhanced Raman scattering (SERS) . . . . .	18
1.4.1 SERS in metallic NPs . . . . .	19
1.4.2 Metal-metal core-shell NPs with tunable SPR . . . . .	20
1.4.3 Theory of SERS . . . . .	21
1.4.4 SERS of core-shell Au@Ag NPs . . . . .	24
1.4.5 Hot spots . . . . .	25
1.4.6 SERS in high energy facets . . . . .	26
1.5 Biosensors . . . . .	26
1.5.1 Electrochemical biosensors . . . . .	28
1.5.1.1 Enzymatic electrochemical biosensors . . . . .	29
1.5.1.2 Nonenzymatic electrochemical biosensors . . . . .	30
1.6 Outline of the thesis . . . . .	31
<b>2 Experimental methods</b>	<b>33</b>
2.1 Introduction . . . . .	34
2.2 Synthesis of NPs . . . . .	34
2.2.1 Materials . . . . .	34
2.2.2 Au@Ag nanorods (NRs) . . . . .	35
2.2.2.1 Au seed synthesis . . . . .	35
2.2.2.2 Au NBP growth . . . . .	36
2.2.2.3 Au@Ag core-shell NR growth . . . . .	36
2.2.2.4 Au@Ag core-shell NR purification . . . . .	37
2.2.3 Ag NRs . . . . .	38
2.2.3.1 Ag seed synthesis . . . . .	38

	2.2.3.2	Ag NR growth . . . . .	38
2.2.4		Au@Ag NSs and NCs . . . . .	39
	2.2.4.1	Au seed synthesis . . . . .	39
	2.2.4.2	Au TOH growth . . . . .	39
	2.2.4.3	Au@Ag core-shell NSs growth . . . . .	40
	2.2.4.4	Au@Ag core-shell NCs growth . . . . .	40
	2.2.4.5	Au@Ag hollow NCs (HNCs) and NSs (HNSs) growth . . . . .	40
2.2.5		Au@Ag nanotriangles . . . . .	41
	2.2.5.1	Au seed synthesis . . . . .	41
	2.2.5.2	Au nanotriangles growth . . . . .	41
	2.2.5.3	Au@Ag nanotriangles growth . . . . .	42
2.2.6		Au@Pd NCs and Pd NCs . . . . .	42
	2.2.6.1	Au seed synthesis . . . . .	42
	2.2.6.2	Au nanooctahedrons growth . . . . .	43
	2.2.6.3	Au@Pd NCs growth . . . . .	43
	2.2.6.4	Pd NCs growth . . . . .	43
2.3		Characterization and application tools . . . . .	44
	2.3.1	Transmission electron microscope (TEM) . . . . .	44
		2.3.1.1 Brief History . . . . .	44
		2.3.1.2 Comparison with light microscope . . . . .	45
		2.3.1.3 Interaction of electrons with matter . . . . .	47
		2.3.1.4 Components of TEM . . . . .	50
		2.3.1.5 Different modes of operations of TEM . . . . .	55
		2.3.1.6 Sample preparation for TEM . . . . .	65
	2.3.2	SERS . . . . .	67
	2.3.3	UV-vis-NIR spectroscopy . . . . .	69
	2.3.4	3D FDTD simulation . . . . .	70
	2.3.5	Cyclic voltammetry (CV) . . . . .	70
<b>3</b>		<b>Morphological characterization of nanoparticles using transmission electron microscopy</b>	<b>74</b>
	3.1	Introduction . . . . .	75
	3.2	Core-shell NPs with same shape but different size . . . . .	76
		3.2.1 Core Au NBPs . . . . .	76
		3.2.2 Au@Ag core-shell NRs . . . . .	77
		3.2.3 Ag NRs . . . . .	81
		3.2.4 Stability performance . . . . .	82
	3.3	Core-shell NPs of different shapes . . . . .	83
		3.3.1 Core Au TOH . . . . .	84
		3.3.2 Core-shell NSs . . . . .	87
		3.3.3 Core-shell NCs . . . . .	88
		3.3.4 Core-shell HNSs . . . . .	90
		3.3.5 Core-shell HNCs . . . . .	92
	3.4	Symmetric and anti-symmetric core-shell NPs . . . . .	93

3.4.1	Core Au triangles . . . . .	93
3.4.2	Au@Ag nanotriangles . . . . .	94
3.5	Core-shell NPs with shells made of Pd . . . . .	97
3.5.1	Au@Pd NCs . . . . .	97
3.5.2	Pd NCs . . . . .	99
3.6	Conclusion . . . . .	99
<b>4</b>	<b>Localized surface plasmon and near electric field studies using SERS</b>	<b>101</b>
4.1	Introduction . . . . .	102
4.2	UV-Vis-NIR spectroscopy of different NPs . . . . .	104
4.2.1	Au@Ag NRs . . . . .	105
4.2.2	Core-shell NSs, NCs, HNSs and HNCs . . . . .	112
4.3	SERS activity . . . . .	114
4.3.1	Core-shell NRs . . . . .	115
4.3.2	Calculation of SERS EF . . . . .	120
4.3.2.1	For 4-MBA . . . . .	124
4.3.2.2	For CrV . . . . .	126
4.3.2.3	For 4-MPy . . . . .	127
4.3.3	Core-shell NSs, NCs, HNSs and HNCs . . . . .	128
4.3.4	Calculation of SERS EF for 4-MBA . . . . .	130
4.4	FDTD simulation . . . . .	133
4.4.1	Core-shell NRs . . . . .	133
4.4.2	Core-shell NSs, NCs, HNSs and HNCs . . . . .	136
4.4.3	Pd NCs and Au@Pd NCs . . . . .	138
4.5	Conclusion . . . . .	140
<b>5</b>	<b>Cyclic voltammetry study and application of the nanoparticles as bio-sensors</b>	<b>142</b>
5.1	Introduction . . . . .	143
5.2	Electrochemical cyclic voltammetry study . . . . .	146
5.3	Electrochemical sensing study . . . . .	148
5.3.1	Amperometric sensing of UA . . . . .	151
5.3.2	Amperometric sensing of AA . . . . .	152
5.3.3	Long-term stability and selectivity . . . . .	153
5.4	Comparison with reported results . . . . .	156
5.5	Conclusion . . . . .	159
<b>6</b>	<b>Conclusion</b>	<b>160</b>
6.1	Summary . . . . .	161
6.2	Outlook . . . . .	164
	<b>Bibliography</b>	<b>166</b>

## Summary

Core-shell of different morphologies where the core Au NPs are bounded by high energy facets have been synthesized following the wet chemical synthesis methods. The morphological characterizations were performed using transmission electron microscopy (TEM) and the growth mechanisms of the NPs were described from the HRTEM (High Resolution TEM) images. Au@Ag nanorods (NRs) with Au nano-bipyramidal (NBP) cores of different lengths varying from 230 nm to 1200 nm were synthesized. The absorption spectra showed multiple absorption peaks for Au@Ag NRs from UV to NIR region due to the presence of higher-order longitudinal and transverse modes along with the dipolar modes. The SERS spectra showed huge enhancement. The highest enhancement was found for Au@Ag NRs of length 450 nm as the dipolar absorption band for them was closely located with the laser excitation wavelength.

Au@Ag core-shell NPs with Au trisoctahedron as cores and Ag nanospheres (NSs) and nanocubes (NCs) as shells were also synthesized. After that, the Ag shells were transformed into hollow shells by galvanic replacement reaction. The absorption spectra showed a higher contribution from Ag shell for Au@Ag NPs with solid shells and for Au@Ag NPs with hollow shells, the contribution from the coupled modes was dominant. The SERS spectra showed highest enhancement for Au@Ag hollow NCs due to the presence of sharp edges and hollow regions. All these observations were verified using finite-difference time-domain (FDTD) simulation studies. The electrochemical responses of these hollow NPs as electrodes were studied and it was found that they can be used as uric acid and ascorbic acid sensors with very high sensitivity and very small minimum detection limit. All these observations suggest that the core-shell NPs with high energy facets are very useful for both SERS and electrochemical bio-sensing.

# List of Figures

2.1	(a) Cross-sectional view of a magnetic lens, (b) path of electrons through the magnetic lens. . . . .	46
2.2	Probable signals generated when a high-energy beam of electrons interacts with a thin specimen. . . . .	48
2.3	Internal block diagram view of a TEM. . . . .	50
2.4	Schematic of (a) Thermionic emission gun, (b) field emission gun (FEG). . . . .	52
2.5	Picture of a side entry holder. . . . .	54
2.6	The two basic operating modes of the TEM (a) imaging and (b) diffraction. . . . .	56
2.7	(a) Ray diagram for SAED pattern formation, (b) relation between SAED spot spacing and camera length. . . . .	58
2.8	Schematic for (a) bright-field (BF), (b) dark-field (DF) and (c) central dark-field (CDF) imaging. . . . .	60
2.9	Position of different detectors in STEM mode. . . . .	61
2.10	Block diagram of different components present in an EDX detector. . . . .	63
2.11	Schematic of the EFTEM and EELS set-up with energy prism. . . . .	65
2.12	Drop casting on a carbon coated copper grid. . . . .	66
2.13	300 kV TEM (FEI Tecnai G <sup>2</sup> F30-ST). . . . .	67
2.14	Photograph of the UV-vis-NIR spectrophotometer. . . . .	69
3.1	(a) Schematic showing different planes present in the Au NBP, (b) TEM image of Au NBPs, (c) HRTEM image of an Au NBP with an FFT pattern of the selected area and a Fourier-filtered image in the insets. . . . .	77
3.2	Bright-field TEM images of Au@Ag NR before purification. . . . .	78
3.3	Au@Ag core-shell NRs of average lengths of (a) 230, (b) 450, (c) 700, (d) 800, (e) 1000 and (f) 1200 nm. . . . .	79
3.4	(a) HRTEM image of Au@Ag core-shell NRs. (b) and (c) Fourier-filtered images of selected areas in part (a). . . . .	80
3.5	(a) and (b) STEM-HAADF images of Au@Ag NRs of length 230 nm, (c) STEM-HAADF, (d) Ag L mapped. (e) Au L mapped. (f) Composite mapped image of an Au@Ag NR. . . . .	81
3.6	(a) Bright-field TEM and (b) STEM-HAADF images of Ag NRs of length 450 nm. . . . .	82
3.7	Bright-field TEM images of (a) Ag NRs and (b) Au@Ag NRs after two months from synthesis. . . . .	83

3.8	(a) Bright-field TEM image of Au TOH NPs, (b) SAED pattern of an Au TOH NP shown in the inset. . . . .	84
3.9	(a) A model TOH NP viewed from $\langle 110 \rangle$ direction, (b) TEM image of a synthesized TOH NP viewed along $\langle 110 \rangle$ direction. . . . .	86
3.10	An atomic model of the Au $\{221\}$ and $\{331\}$ surfaces, showing they can be visualized as the combination of $\{111\}$ terraces and $\{110\}$ step. . . . .	87
3.11	(a) Bright-field TEM image, (b) STEM-HAADF image, (c) Ag-L, (d) Au-L and (e) composite mapped images of Au@Ag NSs. . . . .	87
3.12	(a) Bright-field TEM image, (b) STEM-HAADF image, (c) Ag-L, (d) Au-L and (e) composite mapped images of Au@Ag NCs. . . . .	89
3.13	(a) Bright-field TEM image, (b) STEM-HAADF image, (c) Ag-L, (d) Au-L and (e) composite mapped images of Au@Ag HNSs. . . . .	91
3.14	(a) Bright-field TEM image, (b) STEM-HAADF image, (c) Ag-L, (d) Au-L and (e) composite mapped images of Au@Ag HNCs. . . . .	92
3.15	(a) Bright-field TEM image, (b) SAED pattern of the Au triangular NPs. . . . .	94
3.16	(a) Bright-field TEM image, (b) STEM-HAADF image, (c) Ag-L, (d) Au-M and (e) composite mapped images of the parallel core-shell nanotriangles. . . . .	95
3.17	(a) Bright-field TEM image, (b) STEM-HAADF image, (c) Ag-L, (d) Au-M and (e) composite mapped images of the anti-parallel core-shell nanotriangle. . . . .	96
3.18	(a) Relative thickness map, (b) relative thickness profile of a core-shell nanotriangle. . . . .	97
3.19	(a) Bright-field TEM, (b) STEM-HAADF images of the Au@Pd NCs. . . . .	98
3.20	(a) EDX spectra, (b) STEM-HAADF image, (c) Au-L, (d) Pd-L and (e) composite mapped images of Au@Pd NCs. . . . .	98
3.21	(a, b) Bright-field TEM images, (c) HRTEM image of the Pd NCs. . . . .	99
4.1	Absorption spectra of Au NBPs, Au@Ag core-shell NRs of different lengths and Ag NRs. . . . .	106
4.2	(a) Longitudinal SPR (LSPR) and (b) transverse SPR (TSPR). . . . .	108
4.3	Dependence of the plasmon modes on the lengths of the Au@Ag NRs. . . . .	111
4.4	Absorption spectra of Au TOH NPs and Au@Ag core-shell NSs, NCs, HNSs and HNCs. . . . .	113
4.5	SERS spectra of $2 \times 10^{-4}$ M 4-MBA mixed with the core-shell Au@Ag NRs of different lengths. . . . .	117
4.6	SERS spectra of $10^{-5}$ M CrV mixed with the core-shell Au@Ag NRs of different lengths. . . . .	118
4.7	SERS spectra of $10^{-3}$ M 4-MPy mixed with the core-shell Au@Ag NRs of different lengths. . . . .	119
4.8	SERS spectra of $2 \times 10^{-4}$ M 4-MBA obtained for Ag NRs and Au@Ag NRs of length 450 nm. . . . .	120
4.9	SERS spectra of $10^{-5}$ M 4-MBA mixed with the NPs of different morphology. . . . .	129

4.10	<i>y-z views of the electric-field distribution of (a) Au NRs, (b) Ag NRs, (c) Au@Ag NRs of length 450 nm and the corresponding EF maps for (d) Au NRs, (e) Ag NRs, (f) Au@Ag NRs of length 450 nm. . . . .</i>	134
4.11	<i>y-z views of the electric-field distribution of Au@Ag NRs of length (a) 230 nm, (b) 700 nm, (c) 800 nm, (d) 1000 nm, (e) 1200 nm and the corresponding EF maps for Au@Ag NRs of length (f) 230 nm, (g) 700 nm, (h) 800 nm, (i) 1000 nm, (j) 1200 nm, respectively. . . . .</i>	135
4.12	<i>y-z views of the electric-field distribution of Au@Ag NR of length (a) 80 nm, (b) 230 nm and the corresponding EF maps for Au@Ag NR of length (c) 80 nm, (d) 230 nm with core Au NR of length 75 nm. . . . .</i>	136
4.13	<i>y-z view of (a) the electric field distribution and (b) corresponding EF map for Au TOH NPs. . . . .</i>	137
4.14	<i>y-z views of the electric field distribution for Au@Ag (a) NSs, (b) NCs, (c) HNSs, (d) HNCs and corresponding EF maps for Au@Ag (e) NSs, (f) NCs, (g) HNSs, (h) HNCs, respectively. . . . .</i>	138
4.15	<i>(a) x-z view of electric field distribution and (b) EF map of Pd NCs, (c) x-z view of electric field distribution and (d) EF map of Au@Pd NCs. . . . .</i>	139
5.1	<i>(a) Waveform of the ramped potential applied across the electrodes in cyclic voltammetry, (b) a typical cyclic voltammogram for a reversible electrochemical system. . . . .</i>	144
5.2	<i>Cyclic voltammetry plots for Au TOH NPs and core-shell Au@Ag NSs, NCs, HNSs and HNCs, respectively at a scan rate of 0.05 V/s. . . . .</i>	147
5.3	<i>Cyclic voltammetry plots for different concentrations of UA added into the medium for Au@Ag (a) NSs, (b) NCs, (c) HNSs and (d) HNCs as electrode at a scan rate of 0.05 V/s. . . . .</i>	149
5.4	<i>Cyclic voltammetry plots for different concentrations of AA added into the medium for Au@Ag (a) NSs, (b) NCs, (c) HNSs and (d) HNCs as electrode at a scan rate of 0.05 V/s. . . . .</i>	150
5.5	<i>(a) Amperometric J–t curve and (b) corresponding response of current density for sensing UA with the linear fitted graph in the inset. . . . .</i>	151
5.6	<i>(a) Amperometric J–t curve and (b) corresponding response of current density for sensing AA with the linear fitted graph in the inset. . . . .</i>	152
5.7	<i>Long-term stability performances of the Au@Ag HNCs coated ITO electrode towards electrochemical sensing of (a) UA (2 mM) and (b) AA (0.5 mM). . . . .</i>	153
5.8	<i>Selectivity study for (a) UA and (b) AA sensing for the Au@Ag HNCs coated ITO electrode. . . . .</i>	154

# List of Tables

3.1	Calculated values of the angles of a TOH NP bounded by different crystallographic facets. . . . .	85
4.1	List of the peak positions (nm), their origin, and the peak intensity of different modes for NRs of different lengths from the UV-vis-NIR spectra . . . . .	109
4.2	Number density of NRs as SERS substrate. . . . .	123
4.3	SERS EF for Ag NR and Au@Ag NR of different lengths for 4-MBA as analyte. . . . .	125
4.4	SERS EF for Au@Ag NR of different lengths for CrV as analyte. . .	126
4.5	SERS EF for Au@Ag NR of different lengths for 4-MPy as analyte. .	127
4.6	SERS EF for Au TOH NPs and Au@Ag NPs of different morphologies for 4-MBA as analyte. . . . .	132
5.1	Comparison of the analytical performances between the proposed UA sensor with some other previously reported UA electrochemical sensors.	157
5.2	Comparison of the analytical performances between the proposed AA sensor with some other previously reported AA electrochemical sensors.	158

# Chapter 1

## General introduction

---

---

*In this chapter a brief discussion about the different properties along with the applications of the core-shell nanoparticles and nanoparticles bounded by high energy facets has been presented along with the basic principles of surface-enhanced Raman scattering (SERS) and biosensors.*

---

---

## 1.1 Introduction

The history tells us that the human started the application of nanoparticles (NPs) long ago in the bronze age without knowing anything about NPs. At that time, copper (Cu) NPs were used for coloring the glass for decoration [1]. The first known work on NPs was performed by Michael Faraday after long time, around nineteenth century. In 1857, Faraday prepared colloidal gold (Au) particles from gold chloride to explain the existence of Au particle in ruby glass [2]. Although, this work remained unnoticed for many years but latter this milestone is considered as the foundation of modern colloid science. In 1925 Richard Zsigmondy won the Nobel Prize in chemistry for studying the properties of Au colloid and inventing an ultra-microscope [3].

Nanotechnology was unknown to us till the last century. Once Nobel laureate Richard P. Feynman said during his famous lecture in 1959, “There’s Plenty of Room at the Bottom” [4]. It was Feynman, who first envisioned a technology developed by nanoobjects. From that time to today, there have been made revolutionary developments in nanotechnology. The word “nano” is supposed to be adopted from the Latin term “nannus” or the Greek expression “νῶνος” which means “dwarf” in both the cases. In 1960 at the Eleventh Conférence Générale des Poids et Mesures, the word ‘nano’ was formally approved as a SI prefix, which means  $10^{-9}$  times of the SI base unit [5].

For any object, if one or more of its dimensions fall in the nanometer range (1–100 nm), then the object is referred as NP. At this small dimension, only a few numbers of atoms can be fitted to construct the NP. Depending on the dimension of the NPs, they can be classified into four types, viz. zero-, one-, two- and three-dimensional NPs [6]. Small nanospheres, clusters are considered as zero-dimensional nanomaterials, nanowires and nanofibers are considered as one-dimensional nano-

materials, thin films, nanoplates are considered as two-dimensional nanomaterials and other faceted NPs such as nanocubes (NCs), nanopyramids etc. are considered as three-dimensional nanomaterials. Due to the higher surface to volume ratio, the NPs are very reactive and inherit a lot of interesting properties. As the shape and size of any NP is changed, its properties also change. Based on their different properties, NPs are used for various kinds of applications. Besides specific applications, the synthesis of NPs of different shapes and sizes is also very important from the fundamental point of view. All these reasons have led many people for the synthesis of different kinds of NPs following different synthesis methods.

## 1.2 NPs with high energy facets

In solid state or material physics, we study about the various physical and chemical processes taking place on any surface. So, the surface plays a very important role in having different properties in a material. A crystalline material may be bounded by surfaces of different geometry and the electronic structure of the material is dependent on the geometry of its surfaces. Hence, a crystalline material may exhibit different physical and chemical properties at different surfaces. Therefore, we can tune the properties of any crystalline material by controlling its surface structure [7–9]. For example, Pimentel et al. have found that the  $\{111\}$  surfaces of the Pt NPs catalyze normal hexane into benzene, but the  $\{100\}$  surfaces isomerize hexane [10].

Most of the noble metal NPs have face-centered cubic (*fcc*) crystal structures. The bounding facets of the NPs can be categorized into two types depending on the coordination number and packing density of the atoms on the surfaces: low energy and high high energy facets. The low energy facets are the simplest and flattest facets which are  $\{111\}$  and  $\{100\}$  for an *fcc* crystal. The high energy facets are

denoted by a set of Miller indices (hkl) where at least one index is greater than 1. For a NP with *fcc* crystal, the surface energy increases in the order of  $\gamma\{111\} < \gamma\{100\} < \gamma\{110\} < \gamma\{hkl\}$  [11]. Among different facets, as the  $\{111\}$  and  $\{100\}$  facets do not have open structures which can expose the inner layer of atoms, but they are close-packed flat surfaces. So, they have lower surface energy. Whereas,  $\{110\}$  and other high energy facets have higher surface energy as the inner layer of atoms on the surfaces are exposed and they also have a high density of atoms with low coordination numbers.

So, high energy facets are one special and interesting kind of modified surfaces which contain high density of atomic steps, kinks and ledges. These facets exhibit fascinating surface-enhanced properties which are very useful for various applications, such as in photo-electrical devices, breaking chemical bonds in catalytic reactions, fuel cells, energy conversion, automotive catalytic converters, petroleum catalytic reform and other catalytic applications [12–17]. Therefore, the synthesis of NPs with high surface energy is very useful as it improves the relevant properties of the functional materials. But, most of the noble metal NPs reported in the past decade are generally bounded by the low energy facets like  $\{111\}$  or  $\{100\}$ . As during the growth of the NPs, high energy facets are easily transformed into low energy facets due to higher rate of atom addition on the high energy facets [18]. Which makes it very challenging to synthesize noble metal NPs with high energy facets. By varying different thermodynamic and kinetic parameters during the synthesis, we can control the morphology of any metallic NP [18]. Recent studies have reported various new methods for synthesis of NPs with high energy facets [19, 20].

Usually, the noble metal NPs with high energy facets have unconventional and exotic shapes. As for example, squashed dodecahedral [21], rhombic dodecahedral [22] and bipyramidal NPs (NBPs) [23] are three types of NPs which are enclosed by  $\{110\}$  high energy facets. Other NPs with high energy facets  $\{hkl\}$  could be

categorized in four types:  $\{hk0\}$ ,  $\{hkk\}$ ,  $\{hhl\}$  and  $\{hkl\}$ . Truncated ditetragonal prism [24], concave cube [25], convex tetrahexahedron [26] and rod shaped NPs [27] are the examples of NPs bounded by high energy facets like  $\{hk0\}$ . Between these four types of NPs, the former three are single crystalline in nature, whereas the rod shaped NPs are five-fold twinned. Both the convex [28] and concave [29] trapezohedral NPs fall in the category of NPs bounded by  $\{hkk\}$  high energy facets. In the family of NPs bounded by high energy facets like  $\{hhl\}$ , the most common is the concave trisoctahedron (TOH) which is single crystalline in nature [30]. Five-fold twinned star-shaped NPs with five branches of tetragonal micro-pyramid also fall under this category [31]. Concave hexoctahedron is bounded by  $\{hkl\}$  high energy facets [32]. Apart from the NPs bounded by these four types of high energy facets, concave tetrahedral NPs are one special type of NPs which are bounded by two or more types of high energy facets discussed above [33].

### 1.2.1 Synthesis of noble metal NPs with high energy facets

Different methodologies have been developed to control the size, shape and crystal facets of the noble metal NPs. But, most of them are focused on synthesizing NPs with low energy facets  $\{111\}$  and  $\{100\}$ , as during the growth, the high energy facets are transformed into low energy facets due to the presence of highly unsaturated atoms on the surfaces [18]. Recently, several new methods have been developed for synthesizing noble metal NPs enclosed by high energy facets [34]. The synthesis methods of NPs with high energy facets can be classified into three categories based on the nucleation mechanisms: heterogeneous nucleation, homogeneous nucleation and interfacial nucleation.

### 1.2.1.1 Heterogeneous nucleation

In the synthesis method based on heterogeneous nucleation, the nucleation stage and the growth stage are separated. The seed mediated growth method falls in this category. The seed-mediated growth method is a well-established method for synthesizing noble metal NPs of controlled shape and size with higher monodispersity. In this method, the seed NPs are synthesized first. Then the seed solution is added into the growth solution which generally contains cationic surfactants like cetyltrimethylammonium bromide (CTAB), cetyltrimethylammonium chloride (CTAC), cetylpyridinium chloride (CPC) etc. [32, 35–41]. A metal precursor is added in the growth solution with a weak reductant which is usually ascorbic acid. Hence, we can see that the nucleation to form the seeds and overgrowth of the seeds into NPs are isolated. As the activation energy for the reduction of metallic ions is smaller, so the growth of the seeds happens slowly, which provides us a wider space to control the growth of the NPs [42, 43]. Using the seed-mediated growth method, high energy faceted NPs of different materials such as Au [24, 30, 44, 45], Ag [46, 47], Pd [25, 37], and core-shell heterostructure [48–50] have been synthesized. The shape, size and index of the high energy facets enclosed the NPs could be controlled by varying few parameters, such as seed structures, rate of the reaction, type of surfactants and small adsorbents and introduction of foreign metal atoms during the growth stage.

**Effect of seed structure:** The shape of the NPs can be tuned by controlling the size and crystalline structure of the seeds [51, 52]. Noble metal NPs of different shapes can be enclosed by the same high energy facet due to the different internal crystal structures of the NPs. Again, the presence of any twinned plane in the seeds affects the shape of the NPs [23, 53]. As in this case, the metal atoms tend to be deposited around the twin planes.

**Thermodynamic factors:** The NPs enclosed by high energy facets must be thermodynamically stable. In general, the high energy facets are transformed into low energy facets in the growth solution [18]. The high energy facets are forced to be stabilized by different methods, such as by selective adsorption of halides, surfactants or underpotential deposition foreign metal ions on them, which prevents them to transform into low energy facets. Recently, different kinds of NPs with high energy facets are being synthesized using the underpotential deposition of foreign metal ions on high energy facets [44, 54, 55]. It is an interesting phenomenon where metal ions are reduced on the surfaces of the NPs at a potential less than the equilibrium reduction potential of the metal. The underpotential deposition of foreign metal ions always prefer the high energy facets with more open surface structures. The monolayers formed by the foreign atoms on the high energy facets act as face-blocking agent which slows down the growth rate of these facets [44]. It was observed that as the concentration of underpotential deposition foreign metal ions during underpotential deposition had been increased, the high energy facets became more stable [44].

**Kinetic control:** By kinetic control over the growth of different NPs, we could synthesize various thermodynamically unstable facets [16, 30, 50]. By increasing the reduction rate and decreasing the diffusion rate of the precursor, we could control the deposition of metal atoms on the edges and corners of the seeds in the growth solution [25, 56, 57]. In this way, by governing the growth rate of seeds along different directions, various types of high energy facets could be formed. Some recent studies show that the core-shell NPs with high energy facets could be synthesized by controlling the growth rate only [16].

**Oxidative etching:** When any oxidative etchant such as  $\text{Fe}_3^+$ ,  $\text{O}_2/\text{Cl}^-$ ,  $\text{NH}_4\text{OH}/\text{H}_2\text{O}_2$ , etc. are added into the growth solution, it induces an anisotropic growth of the seeds [58, 59]. In the presence of oxidative etchant, the atoms on the surfaces of the metallic NPs are being oxidized, which affects the crystal structure of the NPs

and leads to the formation of high energy facets [60, 61]. The newly formed high energy facets become stable by absorbing the surfactant molecules on the surfaces.

#### **1.2.1.2 Homogeneous nucleation**

In the method based on homogeneous nucleation, both the nucleation and growth follow the same chemical reaction. Here, the NPs are grown in the same solution where the seeds have been synthesized. In this method, the metal precursor is reduced to form the atoms and then the nucleation process starts. The atoms first grow into seeds which subsequently grow into larger NPs. NPs enclosed by high energy facets also could be synthesized by varying the thermodynamic and kinetic factors discussed before. But, compared to the heterogeneous nucleation method, in this method, besides water we can explore different types of solvents for growth solution, for example ethylene glycol (EG) [62, 63], N,N-dimethylformamide (DMF) [21, 29, 64, 65], benzyl alcohol [33], 1-octylamine [66], etc. Water is the most common solvent used for the synthesis of noble metal NPs based on homogeneous nucleation where various thermodynamic parameters determine the shape and size of the NPs. Due to the wider range of solubility for both organic and inorganic compounds, non-aqueous solvents like EG, DMF are extensively used as solvents. Besides being solvent, they could also act as precursors of reducing reagents for synthesis of metallic NPs [67, 68]. But, the main disadvantage of synthesizing NPs using this method is that the uniformity of sizes is relatively bad compared to the seed-mediated growth method because here the nucleation and growth stages are in overlapping condition [39, 48].

#### **1.2.1.3 Interfacial nucleation**

In the method based on interfacial nucleation, high energy facets are generated due to the chemical reaction only on the surfaces of the NPs. The known electro-

chemical method falls in this category where the high energy facets are generated at the interface of electrode and electrolyte solution. In this method, the growth thermodynamics and kinetics during the nucleation are controlled by an externally applied periodic potential across the electrodes [69]. Due to the applied periodic potential, hydrogen or oxygen ions are periodically adsorbed and desorbed on the surfaces of the metallic NPs. The adsorbed ions on the surfaces preserve the high energy facets from transforming into low energy facets. High energy facets can be also created by replacing metallic atoms by the oxygen atoms, from the low energy faceted surfaces. Using this method, noble metal NPs with a diverse range of high energy facets could be synthesized, especially with Pt-group metals [26–28, 70].

### 1.3 Core-shell NPs

Nanomaterials have attracted huge attention for their utility and applications in the diverse areas including nanocatalysis [71, 72], integrated catalysis [73], nano-electronics [74–78], magnetite-supported catalysis [79–81], high-density information storage [82], etc., due to their unique and interesting properties. If one or more dimensions of a material falls in the nanometer range ( $\leq 100$  nm), we called it nanomaterial. Consequently, nanomaterials exhibit different properties from their respective bulk materials. Recently, NPs have become the center of attention in various fields because as we bring down the bulk materials into nanoregion, we can observe immense changes in both the physical and chemical properties of the materials. If the size of the materials brought down to nanoscale region, the surface to volume ratio increases. As a result, the surface atoms of the NPs dominate over those in their interior besides the quantum effects also start appearing.

It was observed that, as the shape of the NPs changes, the properties also vary due to the shifts of the localized surface plasmon resonance (LSPR) band. For

example, the magnetic saturation, permanent magnetization and blocking temperature of the magnetic NPs are all size dependent. Besides, it was also found that the coercivity of the magnetic NPs is shape dependent [82, 83]. This implies, the properties of the NPs change with their actual shapes.

Currently, a wide range of techniques are available for synthesizing different kinds of NPs. Though, broadly all these techniques can be divided into three categories: (i) **solid-state processes such as milling**, (ii) **condensation from vapor** and (iii) **synthesis by chemical reaction**. Using the above-mentioned techniques, not only monometallic, bimetallic NPs also could be synthesized. The developments of these different types of synthesis techniques have enabled to synthesize a variety of NPs of different shapes like cube [82, 84–90], hexagon [89–94], prism [95, 96], rod [97–105], wire [105–112], disk [113], octahedron [85, 86], tube [105, 114–117], etc. Various physical and chemical properties like electrical [118, 119] and optical properties [120, 121], catalytic activity and selectivity [86, 122–124], melting point [125], etc. are all highly dependent on the shape of the NPs. For Au or silver (Ag) NPs, both the plasmon resonance features and sensitivity to surface-enhanced Raman scattering (SERS) depend on the morphology of the NPs [126].

Initially, only the monometallic NPs had been studied which showed enhanced properties than their respective bulk materials. Later in 1980s, it was found that heterogeneous and composite NPs not only show better efficiency than monometallic NPs, but also have developed some new properties [127–129]. The first core-shell NPs were developed around 1990s [130–132].

### 1.3.1 Synthesis of core-shell NPs

The synthesis approaches of NPs can be broadly categorized into two classes: “top-down” and “bottom-up”. In the ‘top-down’ approach, a bulk material is often

used to cut, mill, and shape to get the desired shape and size. There are different techniques available for synthesizing NPs in the ‘top-down’ approach such as laser-beam processing [133], lithography [134–136], and mechanical techniques like machining, grinding, and polishing [137–140]. In the ‘bottom-up’ approach, the chemical properties of the molecules are used to self-assemble the atoms into some particular shape. Some common ‘bottom-up’ approaches are chemical synthesis, laser-induced assembly, chemical vapor deposition, colloidal aggregation, self-assembly, film deposition and growth, etc. [141–143]. Between these two types of approaches, the ‘bottom-up’ approach is mainly used for synthesizing NPs because using this approach we can synthesize much smaller sized NPs. Besides this, this approach is more cost-effective, has minimum energy loss, and we can have complete control over the growth process with absolute precision compared to the ‘top-down’ approach. For the synthesis of core-shell NPs, as our aim is to make uniform coating of the shell materials on top of the cores, the ‘bottom-up’ approach is more suitable. Again, the synthesis of core-shell NPs is a two-step process, hence a combination of these two approaches could also be used. For example, the core NPs can be synthesized following the ‘top-down’ approach and then the shell can be grown using the ‘bottom-up’ approach in order to get uniform and particular shell thickness. Recently, some core-shell NPs have been fabricated using ‘top-down’ method only. For example, Fe@C [144], Shellac@PVP [145], Au@Ag [146] and some organic core-shell NPs, such as PTX@HF, SFN@HF, PLGA@HF, PLGA@AcDX, PLGA@AcDXSP and AcDXSP@HF [147] have been synthesized using only top-down approaches.

### 1.3.2 Properties of core-shell NPs

Among the different multicomponent NPs, core-shell NPs have fascinated increasing research interest for their various outstanding properties as follows [148, 149]:

- **Versatility:** Core-shell NP is made of an inner core and an outer shell of two different materials. Hence, the combination of different properties of the core and shell materials leads to several different and enhanced properties of core-shell NPs, thus increasing their applications in the field of catalysis, optics, electronics and magnetism [150].
- **Inexpensive:** Core-shell NPs are also useful from an economic point of view. To synthesize a NP of any precious or rare material, first a NP is synthesized of any inexpensive material, and then the NP is coated with the precious and expensive one [151].
- **Tunability:** The properties of the core-shell NPs can be controlled easily and dramatically by changing different parameters such as the constituting materials, shape, size, morphology and the relative thickness between the core and shell [152, 153].
- **Stability and dispersibility:** The outer shell can protect the core NPs from any redox reaction, sintering, aggregation or from the effect of any other reagents [154].
- **Biocompatibility:** For practical bio-application, the biocompatibility is one of the important problems because the NP may be rejected by the immunity system. Hence, the biocompatibility of the NPs can be improved by encapsulating them with a biocompatible material like silica ( $\text{SiO}_2$ ), polymer, etc. Using this method, the toxicity due to the NPs can be decreased [155].
- **Controllability:** The release of the core by leaching the shell can be controlled by varying the pH, temperature or ionic strength in the medium, which is a very important condition for drug delivery [156].

Besides all of these properties, the plasmonic property is one of the most important physical properties for the noble metal NPs which is described as the

resonant interaction between the electromagnetic radiation falling on the NPs due to their free electron like metal structure. The plasmonic properties can be well visualized in Au, Ag, and Cu NPs [157–160].

### 1.3.3 Classes of core-shell NPs

The core-shell NPs can be broadly categorized into four classes depending on the types of core and shell materials. They are the combinations of inorganic-inorganic, organic-inorganic, inorganic-organic and organic-organic materials respectively. The choice of the core and shell materials of the core-shell NPs is generally done depending on the application we want to perform. Recently, core-shell NPs with multiple core NPs [161–163] and with multiple layers of shell materials [164–167] have been synthesized for their unusual plasmonic properties. Among all those types of core-shell NPs, NPs with both inorganic core and shell are most important for their wide range of applications in various fields such as catalysis, information storage, biological labeling, optical bioimaging, optoelectronics, quantum dots, semiconductor physics, fluorescence imaging etc. The inorganic-inorganic core-shell NPs can be categorized into two classes: both the core and shell are made of metal or metal oxides and one of the core or shell is made of silica.

The main advantage of silica (as one of the materials in core-shell NPs) is that it increases the suspension stability and reduces the bulk conductivity of the system. Besides being the most chemically inert material, silica protects the surface preventing the redox reaction without any interference. Again, as silica is optically transparent, it can control the position and amplitude of the surface plasmon absorbance band and so the chemical reactions can be analyzed spectroscopically. For all of these reasons, silica has been used as shell on different types of core inorganic materials such as metals [168–181], metal oxides [182–185], metal salts [181, 186–190], binary inorganic composites [176, 180, 191], etc. For magnetite particles as

core and the silica shell makes them well dispersed and more biocompatible which make them useful in various biological applications [182–184, 192].

The inorganic-inorganic core-shell NPs are very useful for their applications in the field of solar energy absorption, catalysis, permanent magnetism, etc. [193–200]. For core-shell NPs with both of them made of metal or metal oxides, Au as shell material has received special attention for their enhanced physical and optical properties with biocompatibility and bioaffinity through functionalization of amine or thiol terminal groups [201, 202]. Besides, the Au shell provides the chemical stability of the NPs by protecting the core material from oxidation and any type of corrosion.

On the other hand, magnetic NPs are important for their wide range of applications [182–184, 192, 193, 198]. But there are some disadvantages for using magnetic NPs such as:

- they have a high tendency of agglomeration,
- they easily get biodegraded when exposed to any biological systems,
- they are not stable enough resulting the change in shape in the presence of external magnetic fields.

By encapsulating the magnetic NPs as cores inside non-magnetic shells, removes all of those disadvantages and they can be used in different biocomponent applications such as magnetically guided site-specific drug delivery systems as well as magnetic resonance imaging (MRI) contrast agents and in the magnetic separation of oligonucleotides [202]. Nowadays, core-shell NPs are also being used for environmental applications like absorbing toxic materials, such as  $\text{SO}_2$  and  $\text{H}_2\text{S}$  from the air [203, 204].

### 1.3.4 Importance of core-shell NPs

Core-shell NPs being highly functional materials, are progressively appealing more and more attention in the fields of materials chemistry and also in many other fields like biomedical, catalysis, electronics, optics, pharmaceutical, etc. Core-shell NPs have improved and quite different properties than their respective core and shell materials. As the shell material completely shields the core, the reactivity of the core decreases and the thermal stability increases, which implies that the overall stability and dispersibility of the core NP increases. Hence, by encapsulating the core material with desired shell material, we can manipulate the properties of the NPs for specific applications [71, 205]. The purpose of synthesizing core-shell NPs are many folds, such as the ability to increase the stability, functionality, and dispersibility of the NPs, surface modification, reduction in consumption of precious materials, controlled release of the core, and so on.

The core-shell NPs are extensively used in diverse applications in various fields such as catalysis, [71, 206], enhancing photoluminescence, [207–209], biomedical [210–213] and pharmaceutical applications [205], electronics [130, 214, 215], creating photonic crystals [216], controlled drug delivery [217, 218], bioimaging [211, 218–224], targeted drug delivery [211, 217, 218, 222, 225], tissue engineering applications [217, 226], cell labeling, [211, 227, 228], information storage units [229–232], biomedical sensors [182, 191, 233], etc.

If the frequency of the incident electromagnetic radiation matches with the resonant frequency of collective oscillating electrons, then the incident radiation resonantly interacts with the noble metal NPs resulting an enhancement in the electromagnetic field around the NPs. This phenomenon is known as the LSPR which is mostly visible for the noble metal core-shell NPs [99]. The plasmonic core-shell NPs have a wide range of applications in various fields such as photocatalysis [103,

104, 114, 115], solar cell [100–102], sensor [116, 117, 230], biomedical imaging [83, 234], and diagnosis [229, 235, 236] for their attractive optical properties and huge advantages in improving the performance of equivalent processes or devices. Due to the huge absorption in visible band, plasmonic core-shell NPs are used in energy conversion in the solar cells or to drive photocatalysis [237–241]. They are also used as sensors since the LSPR property is very sensitive to the surrounding condition [242–245]. The plasmonic core-shell NPs are expansively used in photothermal therapy because we can tune the LSPR band into the biologically suitable near-infrared (NIR) region [246–249]. By labeling with the reporter molecules, they can also be used for biological imaging [250, 251].

Again, core-shell NPs are used as templates for synthesizing core-shell hollow NPs (HNPs). By removing the core using dissolution or calcination, HNPs are prepared. The HNPs have applications in various fields for different purposes such as lightweight structural materials [252, 253], adsorbents [254], microvessels, catalytic supports [255], electric and thermal insulators [256].

### 1.3.5 Core-shell HNPs

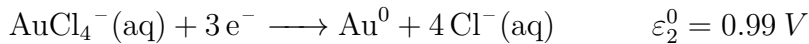
Core-shell NPs have enhanced properties over the monometallic NPs. But the main disadvantage of the core-shell NPs is their storage capacity. For this reason, the HNPs have been designed by taking away the core. These empty spaces created inside the HNPs can be used for many purposes for their huge storage capacities. For example, in biological systems, they can be used for loading and carrying drugs, peptides, genes, biomolecules etc. [257]. The monometallic HNPs do not contain any cores. But the core-shell HNPs contain cores, and the empty spaces are created between the internal core and the shell wall or by inserting a core of different materials inside a monometallic HNP. These core-shell HNPs are also known as yolk-shell or rattle-type NPs [258]. Core-shell HNPs possess collective

properties of both the solid cores and the hollow shells. Besides, the outer shell acts as a shield to the internal core which protects it from any type of damages, leakages or aggregations so that catalytic efficiency of the core does not decrease. These empty spaces inside the core-shell HNPs work as nanoreactor. Any active material can be loaded into these empty spaces for catalytic reactions. As the core-shell HNPs have higher surface area, so they can be used as good SERS substrate for much larger enhancement [259, 260]. By tuning the volume of the empty spaces, both the optical properties and density can be varied over a wide region. By changing the density, the refractive index of the NPs can be tuned. Nowadays, these core-shell HNPs are being used for various applications, such as making lithium-ion batteries, fabricating imaging markers for cancer, capturing hazardous materials, etc. [261–266].

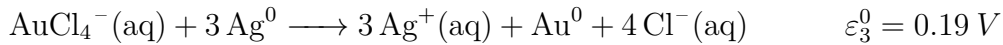
There are numerous approaches to synthesize HNPs, such as galvanic replacement, Ostwald ripening, the Kirkendall effect and oxidative etching [267–269]. Among these methods, galvanic replacement reaction is the most interesting and used method for synthesizing HNPs as it permits to easily control the shapes, sizes, compositions and internal structures of the NPs. Besides, large pore volume can be created using this method which leads to a high surface to volume ratio [269, 270]. Moreover, the galvanic replacement reaction is quite versatile and can be applied to almost all metallic NPs. In this process, the atoms in a metallic NP known as sacrificial template are spontaneously replaced by the atoms of another metal precursor which has a higher reduction potential. This method is extensively applied to synthesize metallic HNPs as the pore volume can be controlled very easily and NPs with ultrathin walls can be synthesized. This is a one-step oxidation-reduction redox process, where the composition and the pore volume of the HNPs can be easily controlled by regulating the molar ratios of the sacrificial template and metal precursor [269, 270].

During this reaction, the electrons from the atoms in the metal NPs are trans-

formed to ions in the metal precursor present in the solution [269, 270]. The reaction is driven spontaneously by the difference in the reduction potentials of both the metals. In this thesis work, the Ag shell of the Au@Ag core-shell NPs were transformed into hollow shell by the galvanic replacement reaction using HAuCl<sub>4</sub> as metal precursor. The galvanic reactions can be expressed as [271]:



Here, the values besides the equations indicate the reduction potential with respect to the standard hydrogen electrode (SHE) potential. The final balanced equation:



Hence, one Au atom replaces three Ag atoms and thus transforms the shell into hollow shell. The composition and pore size of the HNPs were controlled by adjusting the molar ratio between Au@Ag NPs and HAuCl<sub>4</sub> precursor added into the reaction medium.

## 1.4 Surface enhanced Raman scattering (SERS)

The recent developments in nanotechnology have unlocked several scopes in various fields [71, 128, 129, 272], such as catalysis [273–275], optics [276, 277], microelectronics [278–281], biomedicine [157, 282, 283], manufacturing technology [284], computer technology [285, 286], energy [287, 288], and environmental science [289–291] for the unique properties of the NPs compared to bulk of those materials. In the initial stages, only the NPs made of a single material were studied extensively and it was found that they have several superior properties, such as tunable optical properties, excellent catalytic performance, higher ratio of surface atoms and ease of processing. With fast development of the synthesis and characterization techniques

in nanotechnology, around 1980s, it was observed that NPs with multiple materials have much better properties compared to the NPs made of single material. Core-shell NPs have gained one of the most important places in nanotechnology in recent years for their applications in different fields for the diversities in their structure and composition [292, 293].

### 1.4.1 SERS in metallic NPs

Raman spectroscopy is a powerful vibrational optical spectroscopic technique originating due to the inelastic scattering of the photons by the metallic atoms. It gives us the specific fingerprint information about various target molecules [294]. But it was found that the detection sensitivity of the Raman spectroscopy is very low compared to other spectroscopic methods like infrared fluorescence emission and absorption spectroscopy [295]. On the other hand, a highly intense Raman signal was obtained from the molecules absorbed on the metallic surfaces, which is known as SERS [296, 297]. Thus, the discovery of SERS has made huge contribution for sensing any chemical of very low concentration with ultrahigh sensitivity. Besides, SERS can also be used for in-situ studies in aqueous and electrochemical environments with very high sensitivity and spectral resolution in a nondestructive method. Recently, SERS is being also used for in-situ monitoring of some reactions and biological processes [298–300].

The main advantage of SERS is that it only provides the information of the desired adsorbed molecules on the physical, chemical, and biological surfaces. Again, the signals only from the molecules absorbed on the surfaces of the metallic NPs are enhanced, while unabsorbed molecules in the solution do not offer any enhancement. Thus, SERS can also provide the information like orientation, surface bonding and conformation of the absorbed molecules on the surfaces.

Moskovits first explained SERS using the SPR of metallic NPs [301]. It was observed that the metals of Group 1B for example, Cu, Ag and Au exhibit huge SERS enhancement. In addition, few free-electron-like metals and some alkalis could also generate reasonable SERS enhancement. The SERS enhancement strongly depends on the matching of LSPR band with the excitation wavelength. If the excitation wavelength matches with the LSPR band of the NPs, then maximum SERS enhancement is obtained. Recently, single-molecule SERS (SMSERS) has been achieved which has solved the limitation of molecule generality and became one of the most capable tools for trace analysis in biological and medical sciences in addition to security and environmental protection with single-molecular sensitivity [302–304].

#### **1.4.2 Metal-metal core-shell NPs with tunable SPR**

The plasmonic NPs, such as Au, Ag NPs could produce enhanced electric field around them when interacting with the incoming electromagnetic wave. This leads to a massive enhancement of the Raman signals of molecules absorbed on the surfaces of the NPs and the enhancement reaches its maximum when the frequency of the incident electromagnetic radiation matches with the LSPR frequency, which is the frequency of the oscillating electrons of the surfaces of the NPs. Thus, the enhancement is very sensitive to the electronic structure of NPs [305–308]. As the electronic structure of NPs, i.e., the LSPR frequency is strongly influenced by the shape, size and constituting material of the NPs, so the SERS enhancement is strongly dependent on these parameters. Hence, by tuning these parameters, we can vary the SPR properties of the NPs according to their specific applications. But it is quite difficult to vary the LSPR band over a wide region for any NPs by tuning its shape and size. In this context, core-shell NPs provide us huge advantages for tuning the LSPR band over a wide region from UV to NIR region easily and independently

by manipulating the shape, size and composition as well as the relative thickness of the core and shell materials to get huge SERS enhancement [309, 310].

### 1.4.3 Theory of SERS

SERS enhancement is a combination effect of electromagnetic enhancement and chemical enhancement. The electromagnetic enhancement can be explained from the LSPR properties of the NPs. The linear Raman intensity for the  $k^{th}$  vibrational mode of a molecule can be given by the Placzek's polarizability theory as [311]

$$I^k = \frac{2^7 \pi^5}{3^2 c^4} I_0 (\nu_0 - \nu_k)^4 \sum_{\rho\sigma} |(\alpha_{\rho\sigma})_k|^2 N A \Omega Q T_m T_0 \times G \quad (1.1)$$

where  $I_0$  is the intensity of the incident radiation,  $\nu_0$  and  $\nu_k$  are the frequency of the incident radiation and  $k^{th}$  vibrational mode, respectively,  $N$  is the number density of the adsorbates molecules,  $A$  is the surface area illuminated by the incident laser radiation,  $\Omega$  is the solid angle of the collection,  $Q$  is the detector efficiency,  $T_m$  is the throughput of the dispersion system,  $T_0$  is the transmittance of the collection optics,  $(\alpha_{\rho\sigma})_k$  is the enhanced polarizability derivatives and  $G$  is the enhancement factor (EF), respectively.

Using the antenna theory, the total Raman  $I(\omega_R)$  at the scattering frequency  $\omega_R$  can be expressed as [312–314]

$$I(\omega_R) \propto |g_1(\omega_0, r_m)|^2 \times |g_2(\omega_R, r_A) \alpha_m^I(\omega_R, \omega_0) E_0(\omega_0)|^2 \quad (1.2)$$

where  $g_1(\omega_0, r_m)$  is the EF of incident electric field strength at the position  $r_m$  by some optical resonance processes in the antenna,  $g_2(\omega_R, r_A)$  is a factor depends on the relative position  $r_A$  and elastic polarizability of the antenna,  $\alpha_m^I(\omega_R, \omega_0)$  is the Raman polarizability derivatives which implies the modulation efficiency of the

incident photons to the inelastically scattered photons and  $E_0(\omega_0)$  is the incident electric field strength, respectively. Hence, we can see that the total Raman intensity  $I(\omega_R)$  depends on two factors, the local field enhancement  $g_1(\omega_0, r_m)$  and the apparent Raman polarizability derivatives  $\alpha_m^I(\omega_R, \omega_0)g_2(\omega_R, r_A)$ . The apparent Raman polarizability derivative is proportional to the volume of the antenna-molecule system.

When the NPs support SPR, then those NPs are named as plasmonic NPs [315, 316]. A plasmonic NPs must have nanocurved surfaces or nanorecives for showing the SPR effect. The surface plasmon can be categorized into two types: (i) **localized surface plasmons (LSP)** and (ii) **propagating surface plasmons (PSP)**. From the name, we could understand that for LSP, the coherent electrons oscillate around the surfaces of the NPs and for PSP, the coherent electrons oscillate as a longitudinal wave at the surfaces of the NPs [317].

For all metallic NPs with a negative real ( $\Re(\epsilon_M)$ ) and positive imaginary ( $\Im(\epsilon_M)$ ) part of dielectric constant ( $\epsilon_M$ ) could be considered as plasmonic NPs in certain regions of wavelength [318–320]. If a metallic NP of dielectric constant  $\epsilon_M$  is excited by an incoming electromagnetic radiation from  $\hat{z}$  direction with frequency  $\omega_0$  and electric field strength  $E_0(\omega_0)$ , then using electrostatic approximation the local electric field around the NPs,  $E_{loc}(\omega_0, r_m)$  can be given by [321, 322]

$$E_{loc}(\omega_0, r_m) = E_0(\omega_0)\hat{z} - E_0(\omega_0)\frac{\epsilon_M - \epsilon_d}{\epsilon_M + 2\epsilon_d}\left[\frac{\hat{z}}{r^3} - \frac{3z}{r^5}(x\hat{x} + y\hat{y} + z\hat{z})\right] \quad (1.3)$$

where  $\epsilon_d$  is the dielectric constant of the surrounding bulk dielectric medium. And the corresponding intensity of the frequency-dependent LSPR spectrum ( $I_{LSP}(\omega_0)$ ) could be given by [317, 323]

$$I_{LSP}(\omega_0) = \frac{24\pi^2 N a^3 \epsilon_d^{3/2}}{\lambda \ln(10)} \left[ \frac{\Im(\epsilon_M(\omega_0))}{(\Re(\epsilon_M(\omega_0)) + 2\epsilon_d)^2 + (\Im(\epsilon_M(\omega_0)))^2} \right] \quad (1.4)$$

From the equation 1.3 and 1.4 we could see that both  $E_0(\omega_0)$  and  $I_{LSP}(\omega_0)$  will be maximum when  $(\epsilon_M + 2\epsilon_d)$  will vanish. Therefore, the materials with moderately negative  $\Re(\epsilon_M)$  and positive but very small  $\Im(\epsilon_M)$  could only produce strong LSPR and huge local field enhancement thus resulting in enormous SERS enhancement [322]. So, by comparing the values of the dielectric constant, we can find out that only Au, Ag and Cu could meet these criteria. So, NPs of constituting materials Au, Ag and Cu only support strong SPR and produce huge SERS enhancement [320, 321, 324].

Generally, NPs supporting LSP are used as SERS-active substrates instead of NPs supporting SPP since the local EM enhancement for LSPR is much stronger [323]. The LSP of plasmonic NPs is normally excited by any incident light, where the electromagnetic field is focused at the edge, tip and crevice of the NPs, thus enhancing the local electromagnetic field by some orders of magnitude [313]. In addition, the LSP could also be excited by any local oscillating source, like an oscillating molecular electric dipole, quadrupole, etc., which has the ability to reradiate the local EM field into the far-field region.

The SERS enhancement is primarily due to the electromagnetic field enhancement for the LSPR [313]. Besides, there may have also a contribution from the chemical enhancement. Generally, there are five types of chemical effects which contribute to the Raman enhancement and they are listed below:

- Ground state interaction for example chemisorption and surface-complexation [325–328].
- Resonant Raman process for example chemisorption-induced molecular resonance and resonance of analyte molecules [329–332].
- Electron transfer from the atoms of the metallic NPs due to the interaction with photons [333–337].

- Transient electron-enriched states [338, 339], electron transfer between the NPs and analytes [340].
- Voltage-enhanced Raman in molecular junctions [341–343].

In general, the enhancement due to the chemical effects is very small compared to the electromagnetic field enhancement due to LSPR [344, 345].

#### 1.4.4 SERS of core-shell Au@Ag NPs

As discussed above, NPs of constituting materials Au, Ag and Cu show maximum SERS enhancement. Among these three types of NPs, Au and Ag NPs are commonly used as SERS substrates [346]. The reasons are:

- The LSPR band of those NPs can be tuned over a wide region (UV-vis-NIR) easily by changing their sizes and shapes.
- For well-developed and simplified synthesis methods of Au NPs and Ag NPs, it is comparatively easy to synthesize NPs of various shapes and sizes with various complex geometry according to their applications in various fields of nanotechnology [347, 348].
- By varying the shape and size of the NPs, the scattering or absorption cross-section can be tuned.

However, there are some disadvantages of choosing both Au and Ag NPs as SERS substrate. For Ag and Au NPs of identical morphology, Au NPs show comparatively lower SERS enhancement than Ag NPs. Again, Ag NPs suffer from lower stability, homogeneity and biocompatibility and easily get aggregated [349, 350]. As Ag gets easily oxidized and becomes toxic, so Ag NPs are not suitable for *in vivo* applications [308]. In this context, Au@Ag core-shell NPs are more suitable for

SERS substrates, as they have the combined properties of both Au and Ag. The core Au NPs increase the stability and homogeneity of the NPs and the Ag shells increase the SERS enhancement of the system. As the shells are made of Ag, so the Au@Ag NPs show Ag-like optical properties with metal-enhanced fluorescence [351, 352]. Again, as the lattice mismatch between Au and Ag crystals are very small (nearly 0.2%) [52], it is very easy to grow Ag on top of Au relative to other materials. Hence, the synthesis methods of Au@Ag NPs are well-developed and simplified and it is very easy to synthesize in various geometry according to their applications. Above all, the optical properties and the LSPR bands of the Au@Ag NPs largely depend on the shape, size and relative thickness between the core and shell. Hence, the properties can be easily tuned by varying the relative sizes between core and shell, which is much easier than changing shape of the NPs [353, 354]. Moreover, the lattice mismatch between the core Au and shell Ag generates a strain in the NPs, which also contributes into higher SERS enhancement. All these facts drive the researchers to use the core-shell Au@Ag NPs as SERS substrates.

### 1.4.5 Hot spots

We know that the SERS EF is proportional to the fourth power of the local electric field strength around the NPs [312, 355–358]. The electromagnetic field around the plasmonic NPs is not uniformly distributed rather it is highly localized in the spatially sharp regions like edges, tips, nanogaps of the NPs [359–368]. These regions with highly focused electric fields are known as SERS hot spots. These hot spots are categorized into three classes:

- **First-generation hot spots:** The hot spots generated at the tips and edges of any single NPs are called first-generation hot spots. These hot spots exhibit reasonable SERS activity [313].

- **Second-Generation hot spots:** The hot spots generated at the nanogaps of the coupled NPs or nanopatterned surfaces are called second-generation hot spots. They exhibit very high SERS activity [313].
- **Third-generation hot spots:** The hot spots generated at the extremely narrow region of the hybrid nanostructures are called third-generation hot spots [313].

#### 1.4.6 SERS in high energy facets

The noble metal NPs with high energy facets generally contain many highly anisotropic edges and tips and they act as hot spots during the SERS and the local electromagnetic field is increased at those places [369]. Hence, the noble metal NPs with high energy facets can act as good SERS substrates. Besides, the atomic steps, kinks and ledges present in the NPs act as active sites for adsorption of the analyte molecules on their surface which helps in increasing the SERS intensity. If noble metal NPs with high energy facets are constructed as superstructures, the narrow junctions between the NPs also act as hot spots and the electromagnetic field is highly enhanced. The enhancement depends on the arrangement pattern and distance between two adjacent NPs [369, 370].

### 1.5 Biosensors

A sensor is a device which can respond to any event or change in the environment and generates an equivalent and analytically useful signal easily readable and understandable to the observer. There are variety of sensors are available to us which can detect different parameters such as heat, light, motion, pressure, moisture, etc. The sensors can be categorized into two different classes depending on the measure-

ment mechanism: physical and chemical sensors. Different physical parameters such as temperature, pressure, mass, distance, etc. are measured by the physical sensors. While different chemical quantities such as composition, concentration, presence of any particular ion, partial pressure, activity, etc. of any chemical substances are measured by the chemical sensors.

A biosensor is one type of chemical sensor which can detect the concentration of any chemical substance related to any biological component. The first biosensor was developed by Leland Clark, who is known as the father of biosensors for the development of the oxygen electrode for sensing glucose [371]. Currently, biosensors are widely used in different areas such as pharmaceutical, food and agriculture, environmental, industrial treatment, etc. The desired properties of a good biosensor are:

- **Selectivity:** A biosensor should detect the preferred substance we want to detect, not any other substances.
- **Sensitivity:** The biosensor should be very sensitive to the parameters it is measuring and any small changes of the input value should be detected.
- **Low detection limit:** The biosensor should detect a very small amount of substance in the medium.
- **Fast response time:** The response time should be very fast so that if the value of the parameter changes with time, it should be able to detect the changes.
- **Repeatability:** The output of the biosensor should be consistent over repeated measurement of same input quantity.
- **Long term stability:** The biosensors should work for maximum days either it would not be cost effective.

- **Easy preparation and operation:** The preparation and the operation of the biosensor should be easy and the volume of the biosensors should be minimum so that the sensor could be prepared and operated from any place without any professional individual.

Depending on the type of receptors, the biosensors can be classified into six groups, they are enzymatic, nonenzymatic, immune, DNA, genomic and aptamer biosensors, respectively. Based on the detection mechanism, the biosensors can be categorized into four groups, they are electrochemical, thermal or calorimetric, optical and piezoelectric biosensors, respectively.

### 1.5.1 Electrochemical biosensors

The main advantage of the electrochemical biosensors is that the output of the sensors is an electrical signal which is very easy to analyze. The electrical signal is generated due to the transfer of ions produced from the interaction between the receptor and the substance we want to detect. The electrochemical biosensors are mostly used compared to the other types of biosensors as they have high sensitivity, selectivity, robustness and repeatability with a very fast response time. Besides, they are small in terms of size, which makes them useful in terms of portability. In terms of the input electrical signals, the electrochemical biosensors can be categorized into three groups: amperometric, voltammetric or potentiometric and conductometric biosensors. Depending on the types of receptors, the electrochemical biosensors can be classified into two classes; enzymatic and nonenzymatic electrochemical biosensors, respectively.

### 1.5.1.1 Enzymatic electrochemical biosensors

In the enzymatic electrochemical biosensors, a suitable environment is required to maintain the activity of the enzyme used for sensing. For sensing a biological substance, it has to be attached to the transducer with maintained enzyme activity which is known as immobilization of the enzymes. Due to this immobilization process, some ions are generated in the medium which produces an equivalent electrical signal. This immobilization process is highly dependent on the local chemical and thermal environment of the sensors. Depending on the various factors like types of the biological substances, transducers, physicochemical characteristics of the enzyme and operating conditions, the enzymes can be immobilized by various processes [372–374], such as:

- **Adsorption:** It is the most simple and fastest method to prepare immobilized enzymes. The adsorption can be roughly categorized into two classes, physical and chemical adsorption respectively. The physical adsorption takes place primarily via van der Waals interaction. The chemical adsorption occurs following the formation of covalent bonds. The chemical adsorption process is stronger compared to the physical adsorption process.
- **Covalent bonding:** In this process, covalent bonds are formed between a functional group of the enzyme and the substance or transducer. The formation of the covalent bonds occurs at low temperature with low ionic strength and pH in the medium.
- **Entrapment:** In this process, the enzyme is mixed with a monomer solution which is polymerized to a gel. This gel is used to entrap the enzyme.
- **Cross linking:** In this process, a cross linking chemical is used to chemically link the biomaterial with a supporting material or a solid supporter to increase the absorption and stabilize the adsorbed biomaterial.

The enzymatic electrochemical biosensors are highly selective for the target analyte. But the main disadvantage of using these types of biosensors is that the immobilization of the enzyme is very tricky. They also suffer from poor long term stability, besides difficulties in storage and handling.

#### **1.5.1.2 Nonenzymatic electrochemical biosensors**

With various disadvantages of using enzymatic electrochemical biosensors, there is an additional problem regarding the interference by the compounds, which decreases the selectivity of the sensors. For this reason, the enzymatic electrochemical biosensors are not suitable for pharmaceutical applications, as here sometime simultaneous detection of different analyte molecules is necessary [375, 376]. To overcome these disadvantages, nonenzymatic biosensors have been developed. The use of enzymes decreases the stability of the sensors. Hence, the nonenzymatic biosensors are very stable compared to the enzymatic biosensors. But these types of sensors have low sensitivity and the response time is also very large and thus not appropriate for analytical applications [377]. To overcome these disadvantages, the working electrodes are modified. To achieve higher stability, selectivity, electrocatalytic activity and reproducibility, nanomaterials are used as electrodes due to their higher surface area, reduced interfacial resistance and improved electron transport properties. Nowadays, modified electrodes with different types of noble metal NPs such as Au, Pt NPs and carbon-based nanomaterials such as graphene, carbon nanotubes, quantum dots, etc. are being used as nonenzymatic electrochemical biosensors [378, 379].

The electrocatalytic performance of the nonenzymatic biosensors is governed by various parameters such as potential applied across the electrodes, scan rate, concentration and amount of analytes, accumulation time, types of electrolytes and pH of the medium. The potential applied across the electrodes controls the rate of

reaction in the electrodes [380, 381]. As the current passes through the electrolyte medium, so the electrochemical behaviors of the biosensors depend on the properties of the electrolyte. Proper choice of electrolytes for sensing a particular biomolecule can improve the chemical sensitivity, stability and efficiency of the biosensors.

## 1.6 Outline of the thesis

This thesis work is concerned with the synthesis and characterization of core-shell NPs with high energy facets. The seed mediated growth method has been employed for synthesizing Au NPs of different shapes enclosed by high energy facets. Then, Ag has been grown on top of the Au NPs to get core-shell NPs of different morphologies. To investigate the shape and size of the synthesized NPs, transmission electron microscopy (TEM) has been performed. The crystalline structures and compositions of the synthesized core-shell NPs have been confirmed using the higher resolution transmission electron microscopy (HRTEM) and energy dispersive X-ray (EDX) technique in TEM. The plasmonic properties of the NPs were studied by acquiring the absorption spectra. The electric field distributions around the NPs were studied via collecting the SERS spectra which have been verified by the finite-difference time-domain (FDTD) simulation studies. Finally, the core-shell NPs were transformed into core-shell HNPs by galvanic replacement reaction and they were used as electrochemical biosensors for sensing uric acid (UA) and ascorbic acid (AA). Following this introductory chapter, this thesis contains five more chapters.

- **Chapter 2** describes the detail chemical synthesis procedures to synthesize core-shell NPs of various morphologies enclosed by high energy facets. The basic principle of operation of TEM has been briefly described. The basic working principles of all the experimental techniques we have used in characterization and application are briefly discussed.

- **Chapter 3** deals with the morphological studies of the synthesized NPs using the TEM. The shape, size and purity of the NPs were studied in bright-field imaging mode. The crystalline structure, growth direction was found out using the HRTEM images. The composition of the NPs was verified by the EDX technique.
- **Chapter 4** explores the plasmonic properties of the NPs from the acquired absorption spectra. The electric field around the NPs was analyzed from the SERS spectra. The FDTD simulation results were presented for verification of SERS results.
- **Chapter 5** presents the applications of the core-shell NPs along with the core-shell HNPs as an electrochemical biosensor for sensing UA and AA using cyclic voltammetric (CV) and amperometric studies.
- Finally in **Chapter 6** a summary of the thesis along with the scope for future study has been presented.

# Chapter 2

## Experimental methods

---

---

*This chapter contains the brief description of the synthesis procedure of the core-shell nanoparticles along with the brief description about the different experimental instruments and techniques used, like TEM, SERS, UV-vis-NIR, FDTD and CV.*

---

---

## 2.1 Introduction

Different kinds of NPs have been synthesized by seed mediated wet chemical growth method, where firstly a seed solution was prepared, then the seed solution was mixed into a growth medium to grow the seeds into NPs of desired shape and size. In this chapter we have briefly discussed about the synthesis procedure of those synthesized NPs. The shape and size of the synthesized NPs were verified using transmission electron microscopy (TEM). Using the high resolution transmission electron microscopy (HRTEM), we have found the growth direction and the bounding facets of the NPs. The energy dispersive X-ray (EDX) study in the TEM confirms the compositional details of the NPs. The SERS experiment was performed with the NPs and found very high EF, which was also verified using the FDTD simulation. The FDTD simulation also provides us the local electric field map near the NPs when excited with a light source. Finally the electrochemical sensing studies were performed using the cyclic voltammetric and amperometric methods. We have briefly discussed about all the characterization tools and application tools below.

## 2.2 Synthesis of NPs

### 2.2.1 Materials

1-Hexadecyltrimethylammonium chloride (CTAC; 97%) was purchased from Alfa Aesar. 4-Mercaptobenzoic acid (4-MBA; technical grade, 90%), crystal violet (CrV; dye content  $\geq 90\%$ ), 4-mercaptopyridine (4-MPy; 95%), gold chloride trihydrate ( $\text{HAuCl}_4 \cdot 3\text{H}_2\text{O}$ ;  $\geq 99.9\%$  trace metals basis), cetylpyridinium chloride (CPC; 98%), palladium chloride ( $\text{PdCl}_2$ ; 99%) and sodium borohydride ( $\text{NaBH}_4$ ; hydrogen storage grade, 98%) were bought from Sigma-Aldrich. Sodium citrate tribasic dihy-

drate or trisodium citrate (extrapure AR, 99%), cetyltrimethylammonium bromide (CTAB; extrapure AR, 99%), L-ascorbic acid (AA; extrapure AR, 99.7%), silver nitrate ( $\text{AgNO}_3$ ; extrapure, 99.5%), sodium hydroxide (NaOH; 98.0%) and uric acid (UA) were obtained from SRL Chemical. Hydrochloric acid (HCl; 37%) was bought from Merck Millipore. All the chemicals were used as purchased. Ultrapure water (resistivity:  $18.2\text{M}\Omega\cdot\text{cm}$ ) was used for the synthesis of all types of NPs.

## 2.2.2 Au@Ag nanorods (NRs)

To synthesize Au@Ag NRs, at first Au seeds were synthesized. Then it was grown to Au NBPs and Ag is coated on top of them. The synthesized Au@Ag NPs are a mixture of Au@Ag NPs with spherical and rod like shells of Ag. To get the pure Au@Ag NRs, we followed a purification process.

### 2.2.2.1 Au seed synthesis

The Au NBP cores were synthesized following the seed-mediated growth method reported by Weizmann et al. [382]. An aqueous solution was prepared by adding 125  $\mu\text{L}$  of  $10^{-2}$  M  $\text{HAuCl}_4$  solution and 250  $\mu\text{L}$  of  $10^{-2}$  M trisodium citrate solution into 9.625 mL of water. Then 150  $\mu\text{L}$  of  $10^{-2}$  M freshly prepared ice-cold  $\text{NaBH}_4$  solution was injected quickly into the previously prepared solution under constant magnetic stirring. The colorless solution quickly became light purple in color indicating that the citrate-stabilized seed has been formed. After 1 min the stirring was stopped and the resulting seed solution was kept at room temperature for 2 h undisturbed before use so that the extra  $\text{NaBH}_4$  dissociates from the solution completely. The seed solution should not be used after 5 h as the seeds would be overgrown. Now this seed solution could be used for the growth of the NBPs.

### 2.2.2.2 Au NBP growth

2 mL of the previously prepared seed solution was then added to a growth solution made of adding 2 mL of  $10^{-2}$  M  $\text{HAuCl}_4$ , 400  $\mu\text{L}$  of  $10^{-2}$  M  $\text{AgNO}_3$ , 800  $\mu\text{L}$  of 1 M  $\text{HCl}$  and 320  $\mu\text{L}$  of  $10^{-1}$  M AA consecutively in the above sequence into 40 mL of  $10^{-1}$  M CTAB solution. The resultant solution was mixed well by a magnetic stirrer for 10 s and left undisturbed overnight in ambient condition. The color of the resultant solution was changed from colorless to purple which confirmed that NBPs had been produced. To get the surfactant-free concentrated Au NBPs, the solution was centrifuged twice for 20 min at 6000 rpm [382].

### 2.2.2.3 Au@Ag core-shell NR growth

To synthesize Au@Ag NRs, Ag was overgrown on top of the Au NBPs. To get Au@Ag NRs of variable length, here we had prepared a set of 6 growth solutions independently. At first we had taken 30 mL of  $\times 10^{-2}$  M CTAC solution in six beakers and mixed 200  $\mu\text{L}$  of the prepared Au NBPs solution separately in each beaker. Now 3, 5, 7, 8, 10 and 12 mL of  $10^{-2}$  M  $\text{AgNO}_3$  were added into the CTAC solutions separately and subsequently 1.5, 2.5, 3.5, 4, 5 and 6 mL of  $10^{-1}$  M AA were mixed to the solutions respectively under constant magnetic stirring condition. Now the resultant colorless solutions were heated at  $60^\circ\text{C}$  for 4.5 h in a dry oven in stirring condition. During this period of time, Ag was overgrown on top of the Au NBPs and a mixture of Au@Ag core-shell spherical NPs and NRs were formed. The solutions were then centrifuged separately at 3000–6000 rpm for a period of 20 min depending on the size of the NRs [383].

#### 2.2.2.4 Au@Ag core-shell NR purification

After the completion of the growth process, the product was a mixture of two types of NPs: nanospheres (NSs) and NRs. We had performed a purification process to get pure NRs. 30 mL of  $5 \times 10^{-2}$  M CTAB solution was taken in a beaker and the centrifuged NPs were added to this solution. The solution was mixed properly and left undisturbed for 4 h at ambient condition. In the solution, the Au@Ag NRs and Au@Ag nanospheres are surrounded by the CTAB surfactant micelles. There exists an attractive force between the NPs in the solution, known as depletion interaction force [384, 385]. The depletion interaction potential for side-by-side arrangement leads to maximum interaction potential, which is given by

$$U = -(2a_m)Ld'\Pi_m \quad (2.1)$$

Where,  $\Pi_m = C_m N_0 k_B T$ . Here,  $k_B$  and  $N_0$  are the Boltzmann's constant and Avogadro's number, respectively.  $a_m$  and  $C_m$  are the radius and molar concentration of the surfactant micelle.  $L$  and  $d'$  are the length and effective edge length of the NPs. The effective edge length of the NPs depends on the cross-sectional shape of the NPs. Hence, from the equation 2.1, we can observe that the interaction potential between the NRs would be very higher compared to the nanospheres. As a result, the NRs come closer to each other, and start flocculating, followed by gravitational sedimentation. For lower depletion interaction potential, the Au@Ag nanospheres remains suspended in the solution. After 4 h, we had clearly observed a precipitation of Au@Ag NRs at the bottom of the beaker. The supernatant was removed carefully so that the solution remained undisturbed. The precipitation was collected and centrifuged at 3000–6000 rpm for 20 min to get surfactant-free core-shell NRs [386].

### 2.2.3 Ag NRs

To synthesized Ag NRs, Ag seeds were synthesized and they are grown to Ag NRs.

#### 2.2.3.1 Ag seed synthesis

Ag NRs were also synthesized following the seed-mediated growth method. To synthesize citrate-stabilized Ag seed solution, 600  $\mu\text{L}$  of  $10^{-2}$  M ice-cold  $\text{NaBH}_4$  solution was quickly mixed with a solution containing 19 mL water, 0.5 mL of  $10^{-2}$  M  $\text{AgNO}_3$  and 0.5 mL of  $10^{-2}$  M trisodium citrate under continuously stirring condition. After the resultant solution mixed well, it was left undisturbed in dark for 2 h at ambient condition. The seed solution could be used for NR growth within 2 to 5 h [387].

#### 2.2.3.2 Ag NR growth

To grow the Ag seeds into Ag NRs, 180  $\mu\text{L}$  of the prepared seed solution was added in 30 mL of  $10^{-1}$  M CTAC solution and subsequently added 800  $\mu\text{L}$  of  $10^{-2}$  M  $\text{AgNO}_3$  and 400  $\mu\text{L}$  of  $10^{-1}$  M AA respectively under continuous stirring condition. The resultant solution was then heated at 60  $^\circ\text{C}$  for 4.5 h in an oil bath under stirring condition. The final product was similar to the ‘Au@Ag core-shell NR growth’ process, i.e., a mixture of Ag NRs and Ag NSs. We collected the product after centrifuged it twice at 5000 rpm for 20 min. To get the pure Ag NRs out from the mixture, we followed the same purification method that we have followed in the case of Au@Ag NRs [387].

## 2.2.4 Au@Ag NSs and NCs

To synthesize Au@Ag NPs with Au TOH NPs as the core, first Au TOH NPs were synthesized from Au seeds and then they are grown to Au TOH NPs. After that, Ag was grown on top of Au TOH NPs in two different surfactant medium and we got two different kinds of NPs: NCs and NSs. By galvanic replacement reaction, they were transformed into core-shell HNPs.

### 2.2.4.1 Au seed synthesis

Au TOH NPs were synthesized following the seed-mediated growth method. To get the colloidal Au seed solution, a growth solution was prepared by adding 250  $\mu\text{L}$  of  $10^{-2}$  M  $\text{HAuCl}_4$  into 10 mL of  $10^{-1}$  M CTAC solution. Then a freshly prepared 30  $\mu\text{L}$  of  $10^{-2}$  M ice-cold  $\text{NaBH}_4$  solution was quickly added into the growth solution under constant stirring condition. After 10 s, the stirring was stopped and the resultant seed solution was kept in dark undisturbed at room temperature. After 2 h, the resultant seed solution was diluted 1000-fold with  $10^{-1}$  M CTAC solution. This diluted seed solution was used for the growth of Au TOH NPs [388].

### 2.2.4.2 Au TOH growth

To grow Au TOH NPs from the synthesized Au seeds, a growth solution was prepared by adding 2 mL of  $10^{-2}$  M  $\text{HAuCl}_4$  and 4 mL of  $10^{-1}$  M AA respectively into 40 mL of  $10^{-1}$  M CTAC solution. The growth of the Au TOH NPs was initiated by adding 0.4 mL of the previously prepared diluted seed solution into the prepared growth solution. The resultant solution was mixed well and then kept at room temperature undisturbed for 4 h. After that the solution was centrifuged at 4000 rpm for 20 min, twice and the concentrated Au TOH NPs were collected [388].

#### 2.2.4.3 Au@Ag core-shell NSs growth

We had grown Ag NSs on the top of the Au TOH NPs to get the Au@Ag core-shell NSs. At first, a growth solution was prepared by adding 2 mL of  $10^{-1}$  M AA, 1 mL of  $10^{-2}$  M  $\text{AgNO}_3$  respectively into 40 mL of  $4 \times 10^{-2}$  M aqueous solution of CTAB. 250  $\mu\text{L}$  of the as centrifuged concentrated Au TOH NPs were added into the growth solution followed by dropwise addition of 200  $\mu\text{L}$  of 1 M NaOH solution under continuous stirring condition. The resultant solution was stirred for 2 min for mixing the solution and then left undisturbed for 5 h at room temperature to complete the growth process. To collect the Au@Ag NSs, the solution was centrifuged twice at 3000 rpm for 20 min.

#### 2.2.4.4 Au@Ag core-shell NCs growth

To synthesize Au@Ag core-shell NCs, 250  $\mu\text{L}$  of the as centrifuged concentrated Au TOH NPs were added into a growth solution a growth solution composed of 1 mL of  $10^{-2}$  M  $\text{AgNO}_3$  and 30 mL of  $8 \times 10^{-2}$  M aqueous solution of CTAC under constant stirring condition. Then 500  $\mu\text{L}$  of  $10^{-1}$  M AA was added into the solution. The resultant solution was then stirred for 4.5 h at  $60^\circ\text{C}$ . After that, the solution was cooled down and centrifuged for 20 min at 3000 rpm, twice to get the Au@Ag NCs.

#### 2.2.4.5 Au@Ag hollow NCs (HNCs) and NSs (HNSs) growth

The Au@Ag core-shell NPs with hollow Ag shells were synthesized following the galvanic replacement reaction. Both the prepared and centrifuged 100  $\mu\text{L}$  of the Au@Ag NSs and NCs were dispersed in 3 mL of  $10^{-1}$  M CTAB separately under continuous stirring condition. Then 200  $\mu\text{L}$  of  $5 \times 10^{-4}$  M  $\text{HAuCl}_4$  solutions were dropwisely added separately into both solutions. The reactions were stopped after 1

h by centrifuging both the solutions at 3000 rpm for 20 min and the Au@Ag HNSs and HNCs were collected.

## 2.2.5 Au@Ag nanotriangles

To synthesized Au@Ag nanotriangles, at first Au triangles were synthesized from the Au seeds. Then Ag was grown on the top of them under different conditions and we got Au@Ag nanotriangles with two different symmetries.

### 2.2.5.1 Au seed synthesis

The Au nanotriangles were synthesized following the seed-mediated growth method. A growth solution was prepared by adding 1 mL of  $10^{-2}$  M HAuCl<sub>4</sub> and 1 mL of  $10^{-2}$  M tri-sodium citrate solution into 36 mL of water. Then 1 mL of  $10^{-1}$  M of freshly prepared ice-cold NaBH<sub>4</sub> solution was quickly added to the growth solution under stirring condition. After 1 min, the stirring was stopped and the resulting solution was kept at room temperature for 2–4 hours in order to complete the hydrolysis of unreacted NaBH<sub>4</sub> [389].

### 2.2.5.2 Au nanotriangles growth

To grow Au nanotriangles from the synthesized Au seeds, three growth solutions were prepared. The first two growth solutions (labeled as A and B) were prepared by adding 250  $\mu$ L of  $10^{-2}$  M HAuCl<sub>4</sub>, 50  $\mu$ L of  $10^{-1}$  M NaOH and 50  $\mu$ L of  $10^{-1}$  M AA respectively into 9 mL of saturated CTAB solution. A final growth solution (labeled as C) was prepared by adding 2.5 mL of  $10^{-2}$  M HAuCl<sub>4</sub>, 500  $\mu$ L of  $10^{-1}$  M NaOH and 500  $\mu$ L of  $10^{-1}$  M AA respectively into 90 mL of saturated CTAB solution. The nanotriangles formation was initiated by adding 1 mL of the seed solution to the growth solution A and mixed the solution well. Then 1 mL of

the growth solution A was added to the growth solution B and mixed well. Finally, the whole growth solution in B was added to the growth solution C and kept it for 30 min undistributed at room temperature. The resultant solution was then centrifuged at 7000 rpm for 20 minutes twice to get the Au nanotriangles [389].

### **2.2.5.3 Au@Ag nanotriangles growth**

To synthesized Au@Ag nanotriangles with parallel and anti-parallel symmetry, two growth solutions were prepared. The first one contained 40 mL of  $3.88 \times 10^{-2}$  M CTAB, 2 mL of  $10^{-1}$  M AA and 1 ml of  $10^{-2}$  M  $\text{AgNO}_3$ , respectively. The second growth solution contained 40 mL of  $3.88 \times 10^{-2}$  M CTAB, 5 mL of  $10^{-1}$  M AA and 2.5 ml of  $10^{-2}$  M  $\text{AgNO}_3$ , respectively. Then, 500  $\mu\text{L}$  of the centrifuged Au nanotriangle solutions were added to both growth solutions separately followed by dropwise addition of 200  $\mu\text{L}$  of 1 M NaOH into both solutions under continuous stirring condition. After 2 h, the stirring was stopped, and both the solutions were centrifuged at 5000 rpm for 30 minutes, twice, and the Au@Ag nanotriangles were collected.

## **2.2.6 Au@Pd NCs and Pd NCs**

The core-shell Au@Pd NPs were synthesized via wet chemical seed-mediated synthesis method. Au nanooctahedrons were synthesized from Au seeds, and after that Pd shells were grown on Au nanooctahedrons.

### **2.2.6.1 Au seed synthesis**

To prepare the Au seeds, 600  $\mu\text{L}$  of  $10^{-2}$  M freshly prepared ice-cold  $\text{NaBH}_4$  solution was quickly injected in a solution containing 5 mL of  $5 \times 10^{-4}$  M  $\text{HAuCl}_4$  and 5 mL of  $1.5 \times 10^{-1}$  M CTAB under continuous stirring condition. After 10 s,

the stirring was stopped and the seed solution was left undisturbed for 2 h at room temperature. The seed solution was diluted 100 fold into water medium before use.

#### **2.2.6.2 Au nanooctahedrons growth**

To grow the Au seeds into Au nanooctahedrons, a growth solution was prepared by adding 100  $\mu\text{L}$  of  $10^{-2}$  M  $\text{HAuCl}_4$ , 2 mL of  $2 \times 10^{-1}$  M CTAB and 1.5 mL of  $10^{-1}$  M AA, respectively into 20 mL water. Then 300  $\mu\text{L}$  of the diluted seed solution was added to the growth solution and mixed well. The resultant solution was left undisturbed for 8 h at room temperature to complete the growth process.

#### **2.2.6.3 Au@Pd NCs growth**

To prepare Au@Pd NCs, at first  $10^{-2}$  M  $\text{H}_2\text{PdCl}_4$  aqueous solution was prepared by adding 44.5 mg of  $\text{PdCl}_2$  into 25 mL of  $2 \times 10^{-2}$  M HCl at room temperature under continuous stirring condition until the solution became homogeneous. Then, 500  $\mu\text{L}$  of  $10^{-1}$  M AA and 1 mL of  $10^{-2}$  M as-prepared  $\text{H}_2\text{PdCl}_4$  solution were added into the Au nanooctahedron solution prepared before. The resultant solution was mixed well and left undisturbed for 6 h at room temperature to complete the growth process. The solution was centrifuged at 5000 rpm for 20 min to collect the Au@Pd NCs.

#### **2.2.6.4 Pd NCs growth**

To synthesize Pd NCs, 5 mL of  $2 \times 10^{-2}$  M cetylpyridinium Chloride (CPC) and 1 mL of  $10^{-2}$  M  $\text{H}_2\text{PdCl}_4$  were mixed with 1 mL of  $\text{H}_2\text{O}_2$  and the mixture was heated at  $80^\circ\text{C}$  at continuous stirring condition. After that 500  $\mu\text{L}$  of  $2 \times 10^{-2}$  M AA was added to the solution. After 30 min of heating and stirring, the solution was left undisturbed for 1 h to cool down. The Pd NCs were collected from the

solution by centrifuging it at 5000 rpm for 20 min [390].

## **2.3 Characterization and application tools**

The synthesized NPs had been characterized by different instruments. The morphology, shape and size, composition and structural properties have been investigated by transmission electron microscope (TEM). The UV-vis-NIR absorption spectra were recorded to find out the presence of different modes of LSPR. The SERS experiment was carried out to support the field enhancement under LSPR conditions and to find out the EF using the NPs. To support the SERS results, 3D FDTD simulation had been carried out. Lastly, as an application, the NPs had been used as amperometric biosensors for sensing UA and AA using an electrochemical workstation. In this section, the working principle and operation of the tools used have been discussed.

### **2.3.1 Transmission electron microscope (TEM)**

#### **2.3.1.1 Brief History**

In 1924 French physicist Louis de Broglie gave his groundbreaking theory that electron has wave nature and concluded that all the matters have wave properties and for that he got Nobel Prize in Physics. Following de Broglie's theory, in 1927 two research groups, Davisson and Germer and Thomson and Reid, independently carried out electron-diffraction experiments, which proved the wave properties of the electrons. Knoll and Ruska quickly took this idea and developed the first electron microscope in 1932, for which Ruska won the Nobel prize in physics. Within a year, further development of the electron microscope suppressed the resolution limit of light microscope. The commercial TEMs were started developing in 1939 by Siemens

and Halske in Germany. The electron microscope for material science researches started developing from mid 1950s. Nowadays, different types of TEMs are widely available over the world made by many companies such as FEI, Hitachi, JEOL, Philips, RCA, etc.

### 2.3.1.2 Comparison with light microscope

If it is asked ‘what is a microscope?’, most of the people generally would answer that it is a tool for magnifying objects. But the most important property of a microscope is its resolving power, which is the smallest distance between two points that could be distinguished. With our naked eyes, the smallest distance that we could resolve is 0.1 – 0.2 mm. For an optical microscope, glass lenses are used for magnification. The smallest distance that an optical microscope could resolve is given by the Rayleigh criterion. If  $\lambda$  be the wavelength of the illuminating light in the microscope, the smallest distance it could resolve is

$$\delta = \frac{0.61 \lambda}{\mu \sin \beta} \quad (2.2)$$

where  $\beta$  is the semi-angle of the magnifying lens and  $\mu$  is the refractive index of the viewing medium. Now, the wavelength of the visible light falls in the range of 400–700 nm. So from the equation 2.2, the smallest distance a light microscope could resolve will be around 200–350 nm which is about 1000 atom’s diameters. Therefore, many features of the materials below the scale 200–350 nm will not be distinguishable in the optical microscope.

To overcome this limitation, TEM has been invented. In TEM, by increasing the energy of the emitted electrons, we could resolve an object in sub-nanometer range. If  $V$  be the voltage of the electron gun, then the wavelength of the emitted

electrons would be given by

$$\lambda = \frac{h}{p} = \frac{h}{\sqrt{2meV}} \quad (2.3)$$

where,  $m$  and  $e$  are the mass and charge of the electrons, respectively. If the accelerating voltage of the electrons exceeds 100 KeV, then the velocity of the electrons reaches around  $0.5c$ , where  $c$  is the velocity of light in vacuum. So, considering the relativistic effect, the wavelength of the emitted electrons will be given by,

$$\lambda = \frac{h}{\sqrt{2meV \left(1 + \frac{eV}{2mc^2}\right)}} \quad (2.4)$$

Therefore, from equation 2.4, we could find out that for an electron of energy 100 KeV, the wavelength is 3.72 pm ( $3.72 \times 10^{-12}$  m), which is much smaller than the diameter of an atom. Thus, the resolving power of a TEM is very high compared to an optical microscope.

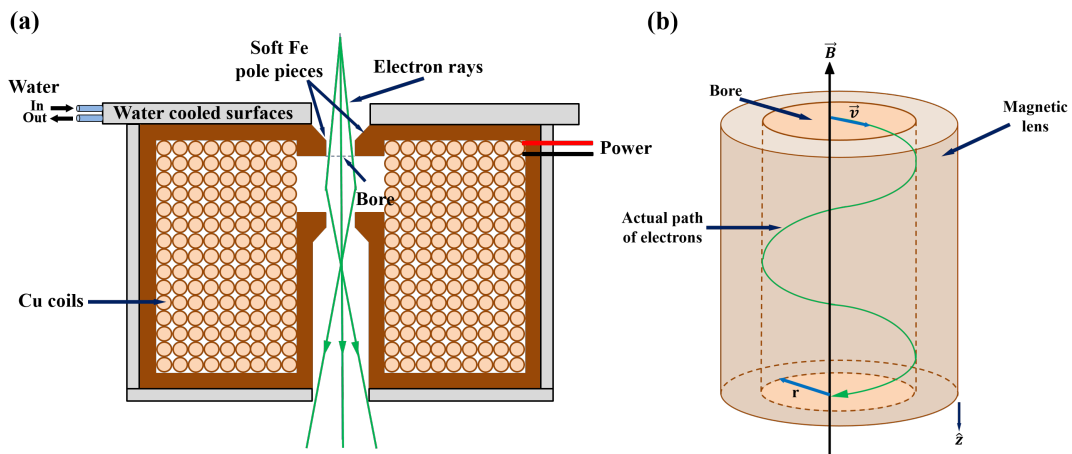


Figure 2.1: (a) Cross-sectional view of a magnetic lens, (b) path of electrons through the magnetic lens.

In both optical microscope and electron microscope, lenses are used for magnification. For the optical microscope, the lenses are made of glass. As the light rays pass through the glass lens, due to the change in refractive index in the optical path,

the rays get focused. But it is quite a hard task to focus the electron beam. For focusing the electron beam, magnetic lenses are used in TEM. Due to the presence of a magnetic field, the electrons experienced a force, called the Lorentz force, for which the direction of the electron beam changes. In the Figure 2.1(a), we have presented a cross-sectional view of a magnetic lens. It is made of a cylindrical core of soft magnetic material (like soft iron) with a hole drilled through its center. The cylindrical core is called pole piece and the hole is called the bore of the pole piece. A copper coil is attached around the pole piece. The electron beam passes through the hole or bore of the pole piece. If a current is being passed through the coil, a magnetic field is generated at the bore of the pole piece and thus the path of the electron beam is being controlled with the current. The trajectory of the electron beam through the bore of the pole piece is helical in nature which is presented in the Figure 2.1(b). If  $B$  be the magnetic field at the bore of the pole piece,  $e$ ,  $m$  and  $v$  be the charge, mass and velocity of the electrons, then the radius  $r$  and the cyclotron frequency  $\omega$  is given by

$$r = \frac{mv}{eB} \quad \text{and} \quad \omega = \frac{eB}{m} \quad (2.5)$$

Here, we have neglected the effects from other electrons. The actual path of the electrons inside the magnetic lens is way more complex. As we need to flow a large amount of current through the copper coil for higher magnification, the coil gets heated due to Joule heating. Therefore, the coil is cooled down by cold water flow from a chiller.

### 2.3.1.3 Interaction of electrons with matter

Electrons are one type of ionizing radiation. So, when electrons interact with the specimen, many phenomenons could be observed. In the Figure 2.2, we have presented the probable signals generated when a high-energy beam of electrons in-

teracts with a thin specimen.

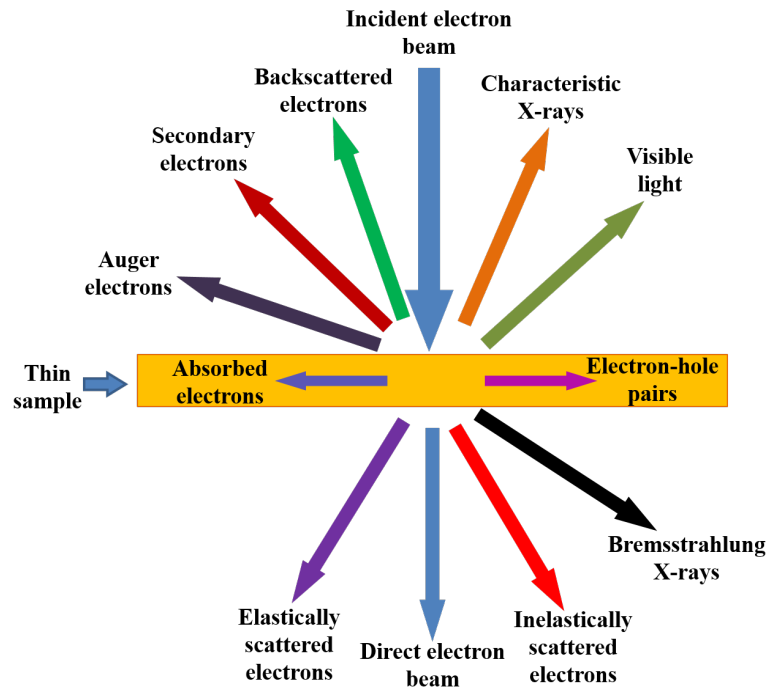


Figure 2.2: Probable signals generated when a high-energy beam of electrons interacts with a thin specimen.

**Unscattered electrons:** The unscattered electrons or direct beam are the electrons which have transmitted without any interaction with the specimen atoms they are interacting with. The energy of the direct beam is unchanged.

**Elastically scattered electrons:** Some of the electrons in the beam get elastically scattered from the specimen atoms. They do not lose any energy. The unscattered and elastically scattered electrons are used for TEM imaging.

**Inelastically scattered electrons:** Some of the electrons get inelastically scattered from the specimen atoms and lose some energy. The lost energy is absorbed by the specimen. Inelastically scattered beams are used in energy filtered transmission electron microscopy (EFTEM) and electron energy-loss spectrometry (EELS).

**Secondary and back-scattered electrons:** As the energy of the electron beam is higher than the work function of the specimen, some of the electrons are knocked out

of the specimen atoms. They are called secondary electrons. A very small number of electrons get scattered at  $180^\circ$  and come backward, they are called back-scattered electrons. Using these two types of electrons, scanning electron microscopy (SEM) is performed.

**Characteristic X-ray and Auger electrons:** Due to the inelastic collision between the specimen atoms and electrons, the electrons in the specimen atoms go to excited states. When they come back to lower states, they emit characteristic X-rays. Acquiring the characteristic X-rays, we could know the elements present in the specimen. This technique is known as energy-dispersive X-ray spectrometry (EDX). Again, the emitted X-ray could be absorbed by some other electrons in the same atom and be knocked out of the atom. These electrons are called Auger electrons.

**Bremsstrahlung X-ray:** When the electrons pass through the specimen, they are decelerated due to interaction with the electron clouds in the specimen atoms. Thus the electrons lose some of their kinetic energy and these energies are radiated as X-rays. This is known as bremsstrahlung X-ray which has a continuous spectrum of energy.

**Visible light:** When the incoming electrons with high energy interact with the specimen, many secondary low energy signals like X-ray, Auger electrons, secondary electrons are generated which are discussed above. Some of the electrons in the specimen absorb energy from these secondary signals and jump to the conduction band from the valance band. Due to the recombination of electron-hole pairs in the conduction band, photons with wavelength in the visible region are generated. These photons are used in cathodoluminescence (CL) spectroscopy for the characterization of the specimen.

Apart from these signals, some of the electrons are absorbed in the specimen. Electron-hole pairs may also be generated in the specimen due to the interaction of the incoming electron beam with the specimen.

### 2.3.1.4 Components of TEM

A TEM is a big instrument with lots of attachments. In the Figure 2.3, we have presented an internal block diagram view of a TEM. The main components are briefly described below.

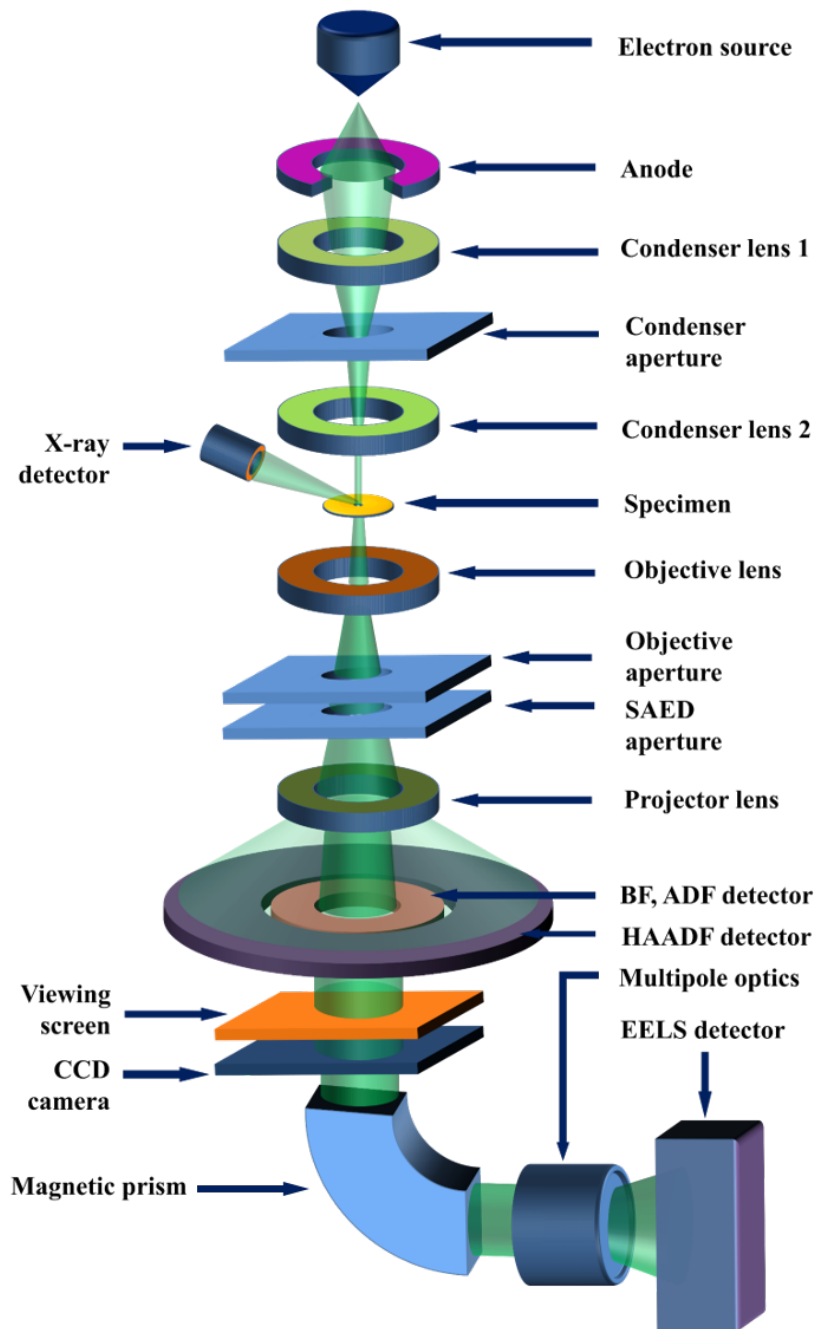


Figure 2.3: *Internal block diagram view of a TEM.*

**Electron gun:** In an electron microscope, the electrons are emitted from the electron gun. Two kinds of electron guns are used in a TEM; **thermionic emission gun** and **field emission gun**. Thermionic emission gun is one of the simplest and most robust electron sources. There exists a filament, known as cathode, a cylindrical grid called Wehnelt electrode and an anode. In the Figure 2.4(a), the basic diagram of a thermionic emission gun is presented. A high current is passed through the filament, and due to Joule heating the temperature of the filament becomes very high, and electrons cross the potential barrier and are emitted from the filament. The current density of the emitted electron beam is given by the Richards equation [391]

$$J = A_G T^2 e^{-\frac{W}{kT}} \quad (2.6)$$

where  $A_G$  is the Richardson constant,  $k$  is the Boltzmann constant,  $W$  is the work function of the filament's material and  $T$  is the temperature of the filament. A small negative bias is being applied to the Wehnelt electrode so that the electron beam is confined and it helps the electron beam to pass through the anode into the column. The most common thermionic gun contains filament made of lanthanum hexaboride ( $\text{LaB}_6$ ) or tungsten (W). The work function of lanthanum hexaboride ( $\text{LaB}_6$ ) is 2.7 eV, thus for thermionic emission the temperature of the filament should be higher than 1800 K. For thermionic emission from tungsten (W) filament with work function 4.52 eV, the temperature of the filament should be higher than 2100 K. The main limitations of the thermionic emission guns are that it is relatively bigger in size compared to the field emission gun and the emitted electron beam has a wide spread of energy, which is not suitable for scanning probe microscopy and EELS microanalysis.

On the other hand, in the field emission gun the filament is biased at a huge negative potential difference relative to the other electrodes. The filament is made

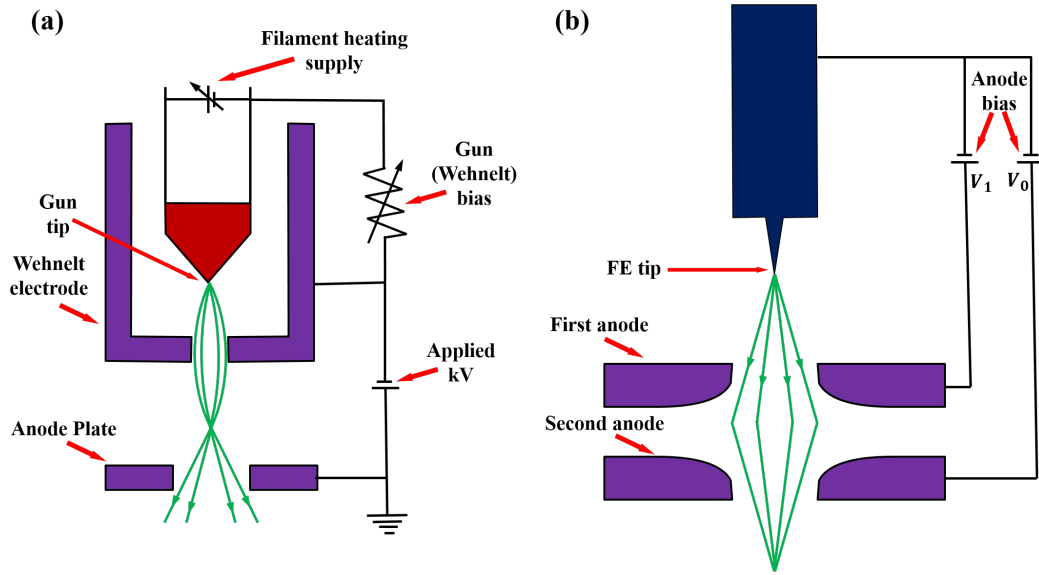


Figure 2.4: Schematic of (a) Thermionic emission gun, (b) field emission gun (FEG).

very sharply pointed so that at this huge potential difference, sufficient potential gradient is created at the surface of the filament and thus the electrons are emitted. There exist two anode plates in the field emission gun. The first one extracts the electrons from the filament and the second one accelerates the electrons. The basic diagram of a field emission gun is presented in the Figure 2.4(b). For a field emission gun, the current density of the emitted electron beam is given by the Fowler-Nordheim equation [392]

$$J = \frac{K_1 E^2}{W} e^{-\frac{K_2 W^{\frac{3}{2}}}{E}} \quad (2.7)$$

where  $W$  is the work function of the filament material,  $E$  is the external applied electric field and  $K_1$ ,  $K_2$  are constants. The required electric field to jump an electron over a potential barrier of  $W$  is given by  $E = \frac{W}{e\lambda}$ , where  $\lambda$  is the De Broglie wavelength of the electron. For tungsten (W) filament of work function  $W = 4.52$  eV, the value of the required electric field is  $E \sim 10^9$  V/m. If  $r$  be the radius of curvature at the tip of the filament, then the electric field generated at the tip due

to the applied potential  $V$  is given by  $E = \frac{V}{r}$ . For a typical filament of field emission gun,  $r = 100$  nm. So, the electric field at the tip due to an applied potential  $V = 1$  KV is  $E \sim 10^{10}$  V/m which is much higher than the required electric field to cross the potential barrier. Hence, the electrons tunnel out from the filament without any heating. These type of field emission guns are also called cold-cathode type guns. In field emission guns, the electron beam is more coherent and have better spatial and energy resolution. As the current density for field emission is very much higher (almost 3 orders of magnitude) than thermionic emission, so brightness is better for the field emission guns. But the beam diameter is relatively small for field emission guns.

There is another type of field emission gun, called Schottky type emission gun, where a high electric field is applied for lowering the potential barrier, and by thermionic emission electrons are emitted. Here, both the applied electric field and temperature of the filament is relatively less than the other cases discussed above. Again, the tip of the filament needs not to be very sharp. After the emission of the electrons from the filament, the electrons gain kinetic energy due to the potential difference between cathode and anode. The electrons start accelerating as they move towards the anode from the cathode. The wavelength of the electron beam after passing through an accelerating voltage  $V$  is given by the equation 2.4.

**Condenser lens:** The condenser lenses in the TEM have the same function as the condenser in an optical microscope. The condenser lenses accumulate the electrons from the first crossover image and focus them on the specimen surface. A TEM contains usually two condenser lenses. The first condenser lens (C1) is a very strong lens with a focal length of a few mm. Whereas the second condenser lens (C2) is weaker compared to the first condenser lens (C1) with a focal length of a few cm. The C1 lens forms an image of the gun crossover and the C2 lens produces an under-focused image of the C1 crossover by spreading the electron beam. A condenser

aperture is used between C1 and C2 to reduce the spherical aberration. There also exists a condenser mini lens in between the condenser lens and the objective lens. It does not have any pole piece to change the magnetic field. It only helps to produce an appropriate convergence angle of the electron beam. In the Figure 2.3, we have presented the different condenser lenses used in a TEM.

**Stage and specimen holder:** For observing a specimen in TEM, we attach it in a sample holder and insert it to the column of the TEM without disturbing the vacuum system. To maintain the vacuum, there exists an airlock system, and we had to first insert it to the airlock chamber. The airlock chamber is being vacuumed first by a turbomolecular pump before inserting it to the column. The specimen stage is situated below the condenser lens in the column and it can move in all three directions (x, y and z) and it can also be tilted. There are two kinds of stage systems; top entry stage and side entry stage. In the top entry stage system, the specimen is inserted from above the pole piece of the objective lens and the specimen is being held at a rotationally symmetric position with respect to the optical axis. In this case, there has no external connection with the specimen holder. So, the stage is stable from any kind of vibrations and heating. In the side entry stage system, the specimen is inserted from the side of the pole piece of the objective lens. Though the side entry stage is not free from vibration and heating, due to the presence of

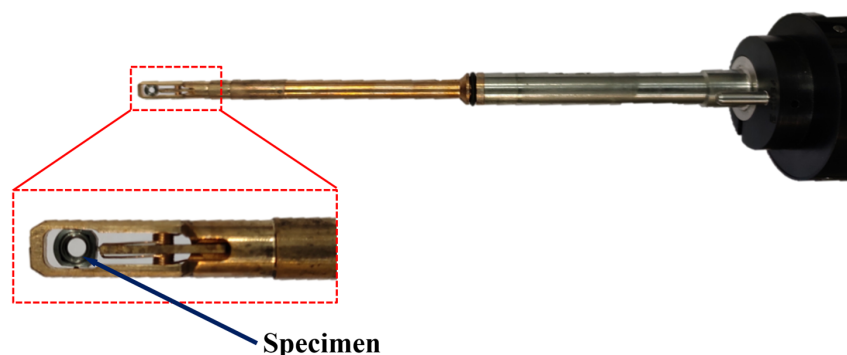


Figure 2.5: *Picture of a side entry holder.*

the additional space above the stage, it can be tilted to a high angle. Also this space can be used for the addition of other analytical attachments like EDX, etc. In our study, we have used a side entry stage system. In the Figure 2.5, we have presented the picture of the side entry holder we have used.

**Objective lens and imaging system:** The objective lens is situated just below the specimen stage. The electron beam comes from the condenser lens to the objective lens through the specimen, and the objective lens focuses the electron beam and forms a magnified real image of the specimen. It is the most important lens in the imaging lens system because it determines the resolution and contrast of the image. It can produce a wide range of magnification from  $0.5X$  to  $10^5X$  by changing the focusing position of either the diffraction pattern or the TEM image by adjusting its excitation. Below the objective lens, there exist an intermediate lens and projector lens, respectively. The intermediate lens is a combination of three types of lenses. The first lens selects the focusing position, the second lens magnifies the image and the third lens helps to achieve rotation-free image. The projector lens is the final lens system. It further magnifies the image formed by the intermediate lens system and project it to the fluorescent screen. The magnification of the projector lens is fixed at a value of  $\sim 150X$ . The total magnification obtained in the TEM is equal to the algebraic product of the magnification of each lens. Below the fluorescent screen, there exists CCD camera and other detectors. The electron beam falls on the detector and the image could be observed directly at the desktop screen.

### 2.3.1.5 Different modes of operations of TEM

By adjusting the focal length of different lenses and using different kinds of attachments, various types of information of the specimen can be obtained using the TEM. Below, we have discussed some common modes of operations in TEM to acquire specific information about the specimen.

**Imaging and diffraction:** Parallel electron beam falls on the specimen and gets diffracted. The diffracted electron beam is focused at the back focal plane by the objective lens and from that it produces a real image of the specimen at the image plane. By adjusting the intermediate lenses, we can project either the image plane or back focal plane on the viewing screen. If the image plane is projected on the screen due to the adjustment of the intermediate lenses, then we can observe the magnified real image of the specimen. In this way, we can observe the magnified real images in imaging mode (Figure 2.6(a)). Again, if the intermediate lenses are adjusted such that the back focal plane is projected on the screen, then we can observe the diffraction pattern formed by the lattice points of the specimen. Thus, we can

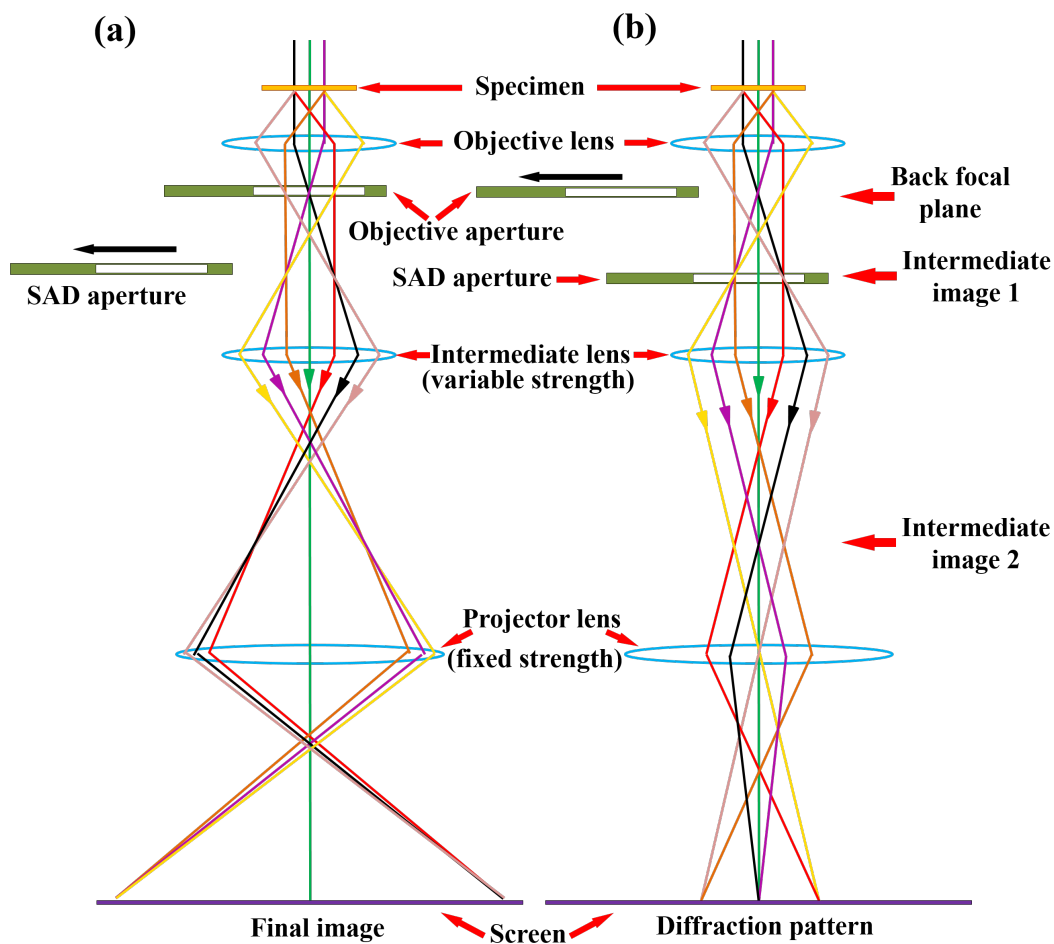


Figure 2.6: *The two basic operating modes of the TEM (a) imaging and (b) diffraction.*

get information about the lattice parameters of the specimen from the diffraction pattern in diffraction mode (Figure 2.6(b)).

**Selected area electron diffraction (SAED):** Crystallographic information like lattice parameters, lattice types and crystallographic orientations of a specimen can be obtained from the electron diffraction pattern in TEM. In the Figure 2.6(b), we have presented a schematic of how diffraction pattern is obtained in TEM. But the main disadvantage of obtaining the diffraction pattern in this way is that the whole area of the specimen is illuminated with the beam and the specimen might be buckled. Again, as the whole beam interacts with the specimen, the transmitted direct beam becomes so intense that it can damage the CCD camera. We can overcome these limitations either by making the incoming beam smaller or by allowing a selected part of electron beam using an aperture to interact with the specimen. If we make the incoming beam smaller, then the beam no longer stays parallel, it becomes converging into the specimen. The technique for obtaining a diffraction pattern with the converging beam is known as convergent beam electron diffraction (CBED). And the technique for obtaining a diffraction pattern by selecting a part of the incoming electron beam using an aperture is known as selected area electron diffraction (SAED). In the Figure 2.7(a), we have presented a schematic of SAED with the selected area diffraction (SAD) aperture and ray diagram. The SAD aperture is inserted at the image plane of the objective lens. Thus, a virtual aperture is formed in the plane of the specimen and only the electrons which pass through the virtual aperture, contribute to the formation of the diffraction pattern. The electrons which pass through the out-side region of the virtual aperture, eventually hit the SAD diaphragm (shown with the dotted lines in the Figure 2.7(a)).

When the electron beam is diffracted from a specimen, we get different kinds of diffraction patterns. For diffraction from a single crystal, the diffraction pattern contains several sharp spots. For diffraction from a poly-crystalline specimen,

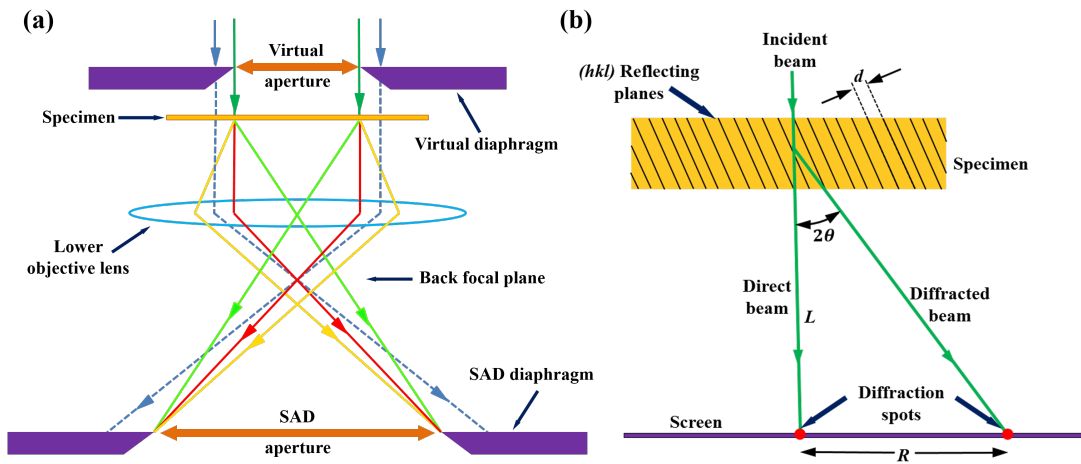


Figure 2.7: (a) Ray diagram for SAED pattern formation, (b) relation between SAED spot spacing and camera length.

the diffraction pattern contains several concentric rings. We can consider the polycrystalline material as a combination of multiple numbers of small single crystal domains oriented in different directions. As these small single crystal domains produce several diffraction spots in various directions, they construct the ring pattern by superposition of the spots. For diffraction from an amorphous material, the diffraction pattern contains much wider rings without any speckle compared to the diffraction pattern obtained from polycrystalline material. The lattice constants of the different crystallographic planes can be obtained by measuring the distances of the spots from the direct beam or from the radii of the diffraction rings. In the Figure 2.7(b), we have presented a schematic of a diffraction spot formed due to diffraction. If  $d$  be the crystal plane spacing of the specimen, then according to Bragg's law,

$$2d \sin \theta = n\lambda \quad (2.8)$$

where,  $\theta$  is the angle of diffraction and  $\lambda$  is the wavelength of the incident electron beam. From the Figure 2.7(b), if  $R$  be the distance of the spot from the direct beam,

then we can write

$$\frac{R}{L} = \tan 2\theta \quad (2.9)$$

where,  $L$  is the distance between the specimen and the screen or camera, known as camera length. As the angle of diffraction ( $\theta$ ) is very small, then we can write,

$$\frac{R}{L} = \tan 2\theta \cong 2\theta \cong \sin 2\theta = \frac{\lambda}{d} \quad (2.10)$$

Therefore,

$$d = \frac{L\lambda}{R} \quad (2.11)$$

From the equation 2.11 we can find out the crystal plane spacing ( $d$ ) by measuring the distance of the diffracted spot from the direct beam ( $R$ ).

Apart from CBED and SAED, another kind of diffraction takes place, known as Kikuchi diffraction. If the specimen is thick, then a large number of electrons are diffracted incoherently and create a pattern when they satisfy the Bragg's condition. Along with the SAED pattern, in some cases we can observe the Kikuchi diffraction pattern as lines, known as Kikuchi lines.

**Bright-field and dark-field imaging:** The incoming electron beam gets diffracted when it transmits through the specimen and forms a diffraction pattern at the back focal plane of the TEM. The diffraction pattern contains a central bright spot which is called direct beam as it does not contain any diffracted electrons. Around the central bright spot, there exist many bright spots with comparatively lower brightness than the central bright spot. They are originated due to the diffracted electrons. We can select any spot, either the central bright spot or any diffracted spot with an aperture for imaging the specimen. If we allow only the central bright

spot for imaging by masking all other diffracted spots, then it is called bright-field (BF) imaging (Figure 2.8(a)). If we allow to form the image with any diffracted beam by masking all other spots, then it is called dark-field (DF) imaging (Figure 2.8(b)). From the Figure 2.8(a) and 2.8(b) we can observe that the selected electron beam passes along the optical axis for BF imaging, but not for DF imaging. This leads to arise different kinds of aberrations in the DF image. To remove this drawback, there is a modified DF imaging technique, called central dark-field (CDF) imaging. In this mode, the diffracted beam is being directed to fall on the sample at an angle equal and opposite to the scattering angle of the selected beam (Figure 2.8(c)). The main advantage of using these techniques is that we can determine from which parts the electrons are diffracted or not, and from these information lattice defects and specimen thickness are analyzed.

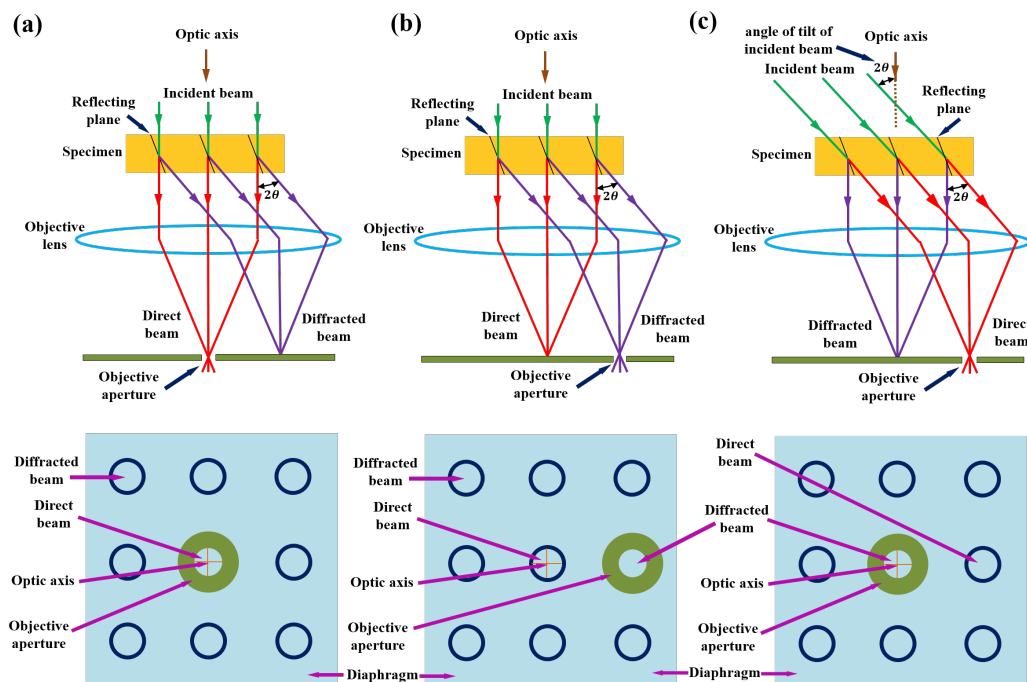


Figure 2.8: Schematic for (a) bright-field (BF), (b) dark-field (DF) and (c) central dark-field (CDF) imaging.

**Scanning transmission electron microscopy (STEM):** In scanning transmission electron microscopy (STEM), the image is formed by scanning the electrons

transmitting through an area of the specimen. In this mode, a convergent beam of electrons falls on the specimen, and the electrons passing through it are scanned using a double deflection coil in both x and y directions. In this case, the electron beam does not pass through the objective lens. The double deflection coil is kept at the focal plane of the upper objective lens. The electron beam is brought parallel to the optic axis by the upper objective lens. As a result, the diffraction pattern remains unchanged during the scanning process. The main advantage of using STEM mode is that the image formed in this mode is free from chromatic aberration as the electron beam does not pass through the objective lens. But, it takes a longer time to acquire an image due to the scanning process. The magnification in STEM mode depends on the area selected in the specimen.

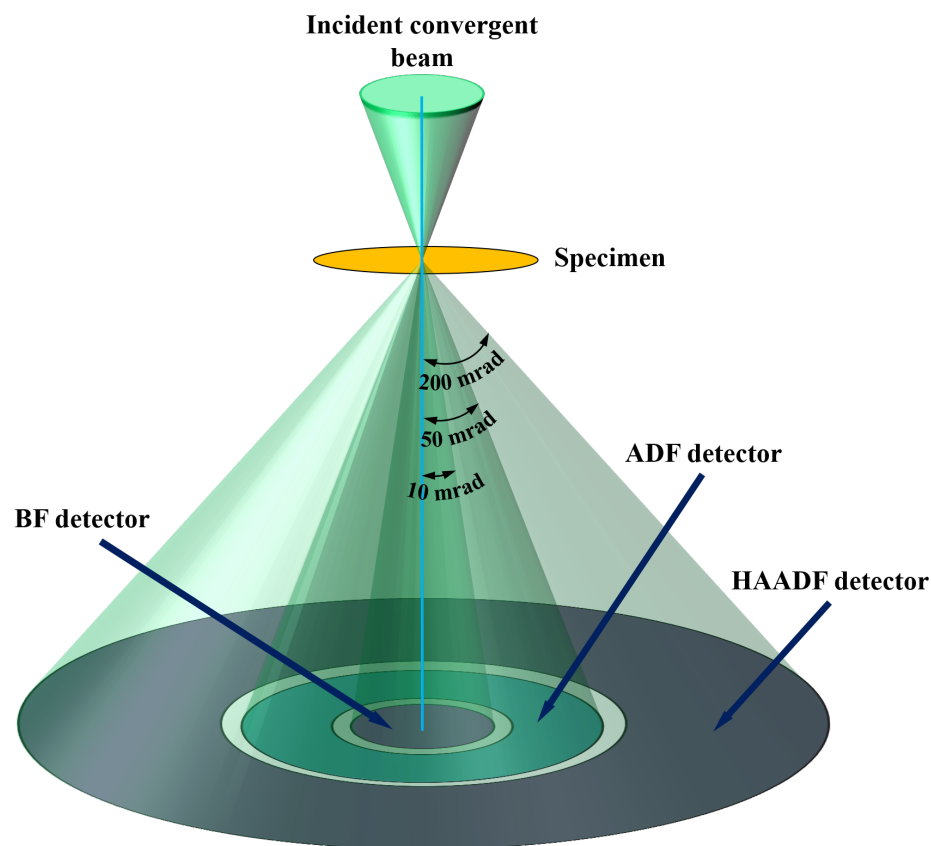


Figure 2.9: *Position of different detectors in STEM mode.*

BF and DF imaging in STEM mode can also be performed. Unlike BF and

DF mode in TEM imaging, in STEM mode, the detectors are placed at different position for BF and DF imaging. Whereas in TEM imaging mode an aperture is used to select different diffracted spots. The BF detector is placed along the optical axis of the electron beam where it collects the electrons from the direct beam which are scattered at an angle below 10 mrad. For DF imaging, an annular dark-field (ADF) detector is placed around the BF detector to collect the electrons which are diffracted at an angle between 10 mrad to 50 mrad.

When the electron beam passes through the specimen, some electrons are scattered at high angles either due to inelastic scattering or thermal diffuse scattering (TDS) or both. These electrons are collected by another annular dark-field which is kept at a large angle, called high angle annular dark-field (HAADF) detector. The HAADF detector usually collects the electrons which are scattered at an angle in between  $\beta_1 \sim 50$  mrad to  $\beta_2 \sim 200$  mrad. The resolution of a HAADF image is determined by the incident probe diameter on the specimen. The HAADF image can be easily understood as there is no interference effect between the scattered electrons as multiple scattering at high angle is absent due to a very small scattering cross-section. The intensity of the HAADF image is proportional to the square of the atomic number of the specimen material. So, the heavy atoms look brighter compared to the lighter atoms. For this reason, the HAADF image is very useful to understand the core-shell NPs. In the Figure 2.9, we have presented the schematic of the position of different detectors in STEM mode.

**Energy dispersive X-ray spectroscopy (EDX):** We know that when a high energetic electron beam interacts with a material, characteristic X-rays are produced. An X-ray energy dispersive spectrometer is attached to the TEM to collect this characteristic X-rays, and analyzing the spectrum, it provides the elemental information of the specimen. An EDX spectrometer consists of three parts; detector, analyzer unit and multi channel analyzer (MCA), respectively. When the charac-

teristic X-rays fall on the detector, an electric signal is generated and it passes to the analyzer unit. Here an electric pulse is generated which is proportional to the energy of the X-ray and this current is measured in the multi channel analyzer (MCA) unit. Normally, a semiconductor detector like Si(Li) detector is used in the EDX spectrometer. When the X-rays fall on the detector, electron-hole pairs are generated which are separated by applying a reverse bias across the detector. In this way the electric pulses are generated. In the Figure 2.10, we have presented the block diagram of different components present in an EDX detector used in TEM.

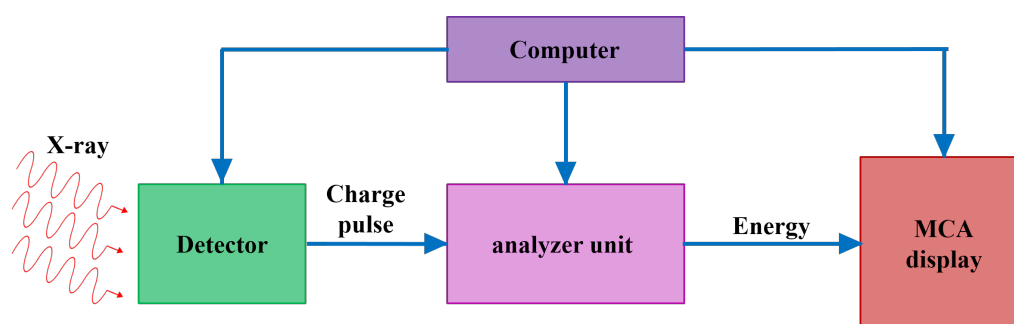


Figure 2.10: *Block diagram of different components present in an EDX detector.*

The EDX detector not only tells us the composition of the specimen, but it can also provide us a pictorial representation of the distribution of different elements present in the specimen. By acquiring the STEM-HAADF image, we can draw a line over the image, and EDX spectra are acquired over that line. This is called line profile EDX imaging. It shows how the concentrations of different elements vary along the line. By EDX elemental imaging, we can select a region of the specimen and by acquiring the EDX spectra over the whole region, it shows us the concentration of different elements at different regions of the selected area in the specimen.

**Energy filtered TEM (EFTEM) and electron energy loss spectrometry (EELS):** When the electrons are transmitted through the specimen, some of them are inelastically scattered and lose some of their kinetic energy as well as momentum.

The inelastically scattered electrons are then passed through a magnetic prism. Hence, the paths of the electrons vary according to their energy. An energy slit with adjustable energy is mounted in between the magnetic prism and detector to select electrons with specific energy and image is formed with those selected electrons only. This is known as energy filtered TEM (EFTEM). In the Figure 2.11, we have presented the schematic of the EFTEM set-up with magnetic prism. If we allow only the electrons which have not lost any energy then the image is formed only with the elastically scattered electrons. Therefore, the image is formed with enhanced contrast. If we allow to pass the electrons which have lost the energy equal to the ionization energy of any material present in the specimen, then the formed image will be sensitive to that material only. In this way we can get an idea about the distribution of different elements present in the specimen same as EDX imaging. The main advantage of EFTEM imaging over EDX imaging is that both energy and spatial resolution is much higher for EFTEM imaging.

Electron energy loss spectrometry (EELS) is a spectroscopic method, where all of the inelastically scattered electrons fall on the detector without passing through the energy slit and provide us an energy spectrum. Both qualitative and quantitative information can be obtained from the EEL spectra. The inelastically scattered electrons can be classified into three categories from the EEL spectra. The first one is plasmonic electrons, which are the electrons excited by the collective oscillations of free electrons. The plasmon peaks are situated in between 10 to 50 eV in the EEL spectra. The second one is the valence-electrons originated due to the inter- and intra-band transitions. These electrons are situated in between 0 to 10 eV in the EEL spectra. And the third one is the electrons originated due to the inner-shell electron excitations or core excitations. These electrons are situated in the range 50 to 2000 eV in the EEL spectra. From the inner-shell electron excitations we could know the oxidation states of any material.

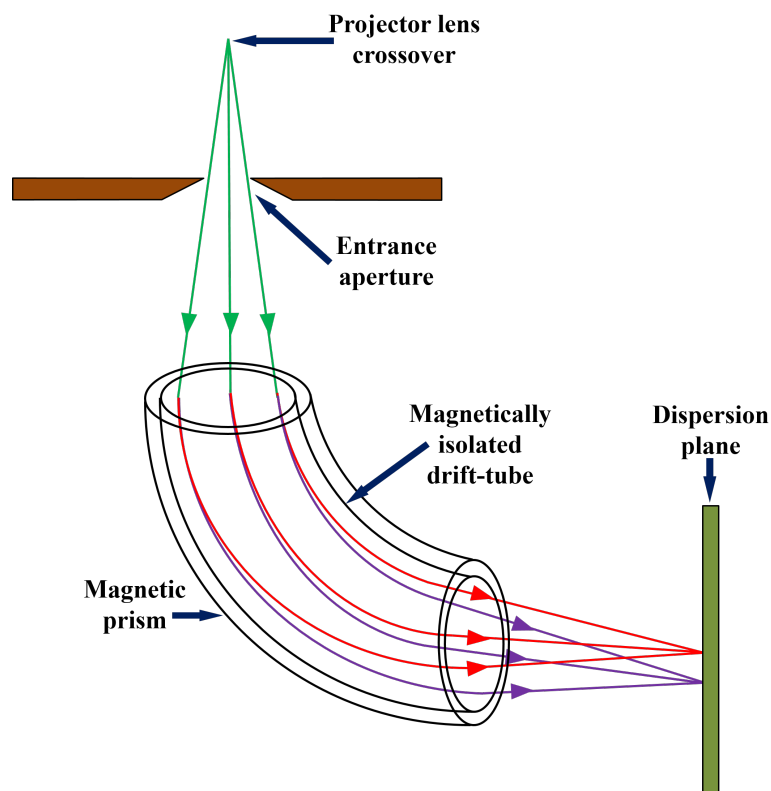


Figure 2.11: *Schematic of the EFTEM and EELS set-up with energy prism.*

### 2.3.1.6 Sample preparation for TEM

To investigate a specimen using TEM, the specimen has to be electron transparent, as the magnified image is formed with the transmitted electrons. Thus to observe a bulk specimen, we need special attention for the specimen preparation where the specimen is thinned using special techniques so that it becomes electron transparent. This procedure is known as *cross-sectional sample preparation*. In our work, we have synthesized different kinds of NPs. As the NPs are transparent to electron, so we do not need any kind of special treatment for observing them in TEM. The synthesized NPs are kept in colloidal form in water. We have used carbon coated copper grids with 300 meshes for TEM observation. The NP solutions are dropcasted on the grids. As the water evaporates from the grids, the NPs got attached to the carbon film of the grid due to adhesive force. Then the grids were

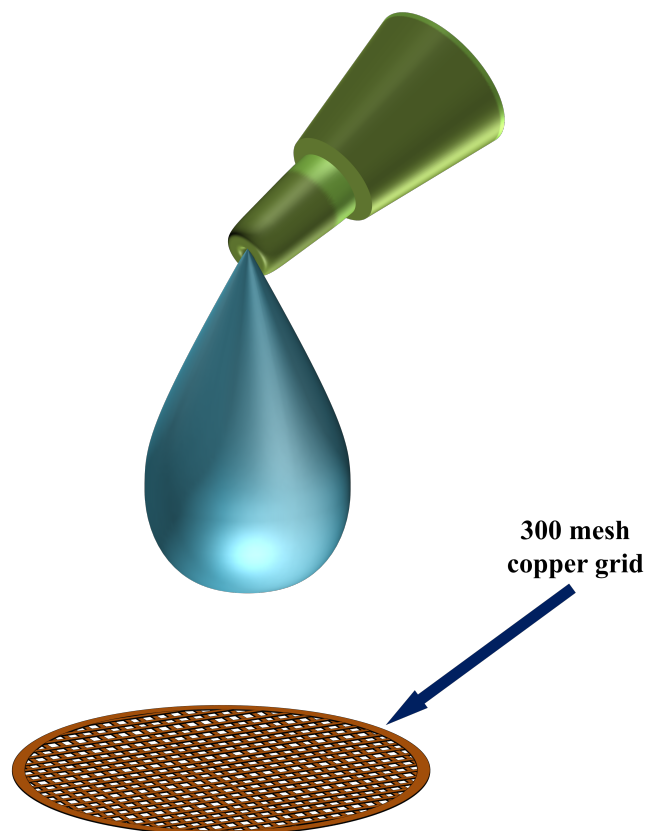


Figure 2.12: *Drop casting on a carbon coated copper grid.*

kept in a vacuum desiccator for 30 min so that they got dried completely before inserting them into TEM. In the Figure 2.12, we have present a schematic of a carbon coated copper grid we have used for TEM observation.

In our whole work, the TEM studies were performed in an FEI Tecnai G<sup>2</sup> F30-ST instrument operating at 300 kV. It is equipped with an Orius SC1000B CCD camera from Gatan Inc., a high-angle annular dark-field (HAADF) detector from Fischione (model 3000), an energy-dispersive X-ray (EDX) spectroscopy attachment from EDAX Inc. for chemical compositional analysis, a post-column Imaging Filter (Quantum SE, Model 963) from Gatan Inc. and a Gatan Quantum SE (model 963) EELS spectrometer. The picture of the TEM is shown in the Figure 2.13.

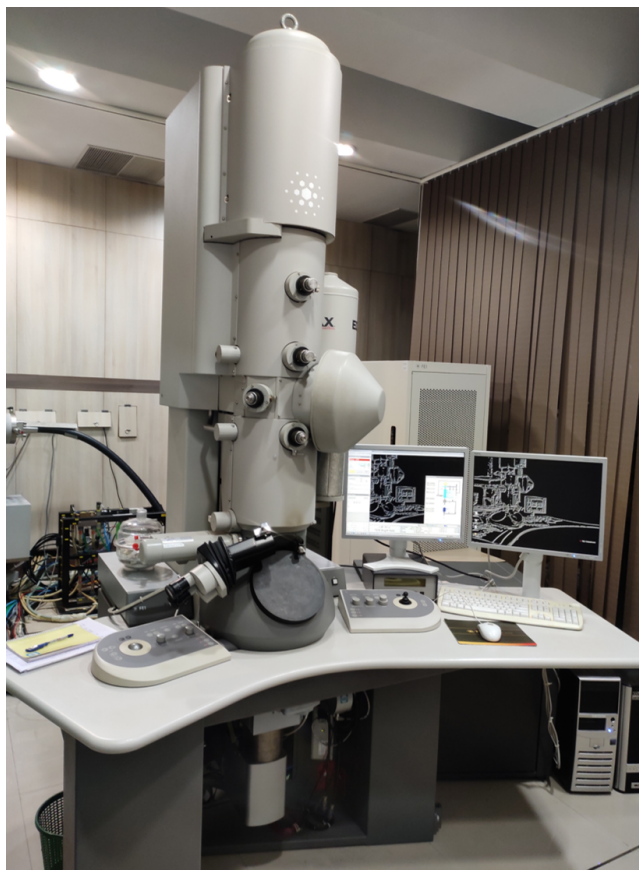


Figure 2.13: 300 kV TEM (FEI Tecnai G<sup>2</sup> F30-ST).

### 2.3.2 SERS

SERS is an ultrasensitive vibrational spectroscopic technique involving the inelastic scattering of incident photons by a molecule. SERS is widely used to detect molecules on or near the surfaces of plasmonic nanostructures. When a material interacts with a monochromatic ray of light of frequency  $\nu_0$ , most of the photons are scattered at the same frequency ( $\nu_0$ ), which is known as Rayleigh scattering. But, a very small number of photons are scattered with a frequency either higher or lower than the initial frequency ( $\nu$ ). These photons interact with the vibrational energy levels of the molecules in the material. This phenomenon is known as Raman effect. The frequency difference between the incident photons and scattered photons

is equal to the molecular vibrational frequency of the molecules ( $\Delta\nu$ ).

$$\Delta\nu = \nu_0 \pm \nu \quad (2.12)$$

Raman scattering is a very weak scattering process corresponding to other scattering events. Generally, to generate one Raman scattered photon, approximately  $10^6$ – $10^8$  scattering events should happen [393]. The number of Raman peaks in a Raman spectrum depends on the number of vibrational modes of the molecule. The peaks originated due to the photons with lower frequencies ( $\nu_0 - \nu$ ) is known as Stokes lines and the peaks originated due to the photons with higher frequencies ( $\nu_0 + \nu$ ) is known as anti-Stokes lines. Generally, the Stokes lines have more intensity than anti-Stokes lines. In Raman spectroscopy, the vibrational frequency of a molecule ( $\nu$ ) is measured as a shift from the frequency of the incident photons ( $\nu_0$ ).

The SERS measurements were carried out in a homemade Raman setup, where a continuous-wavelength diode-pumped solid-state laser from Laser Glow Technology, Canada, LRS-0532-PFM-00300-03, was used as the excitation light source. The laser has a wavelength of 532 nm. The output excitation energy was fixed at 3 mW using a neutral density filter. For focusing and filtering, InPhotonics made 532 nm Raman fiber-optics probe with a spectral range of 200–3900  $\text{cm}^{-1}$  (Stokes) was used for sample excitation as well as data collection. The probe consisted of two fibers, a 105  $\mu\text{m}$  excitation fiber and a 200  $\mu\text{m}$  collection fiber with a numerical aperture (N.A.) of 0.22. The spectra were collected in a scientific-grade spectrometer equipped with a TE-cooled 2048-pixel charge-coupled detector from Ocean Optics (QE65000) with a response range of 220–3600  $\text{cm}^{-1}$ .

To acquire the SERS spectra of different analytes, we have mixed a small amount (10–50  $\mu\text{L}$ ) of the concentrated NP solutions with the analyte solutions (190–150  $\mu\text{L}$ ). To obtain the SERS spectra, we have used  $2 \times 10^{-4}$  and  $10^{-5}$  M 4-MBA,  $10^{-5}$  M CrV, and  $10^{-3}$  M 4-MPy respectively as analytes. The resultant

solutions were kept under laser focus and Raman spectra for different NPs with different analytes were collected at room temperature.

### 2.3.3 UV-vis-NIR spectroscopy

The UV-vis-NIR absorption spectra of the NPs were obtained using a Jasco V-770 UV-vis-NIR spectrophotometer. It is equipped with a unique single monochromator which provides maximum light output with excellent absorbance linearity. A photomultiplier-tube detector was used for the detection in the UV-to-visible region and a Peltier-cooled PbS detector for the detection in the NIR region. In the Figure 2.14, we have shown the UV-vis-NIR spectrophotometer we have used to acquire the absorption spectra throughout our work.



Figure 2.14: *Photograph of the UV-vis-NIR spectrophotometer.*

To acquire the absorption spectra of any NP, the concentrate NP solution was first diluted in water medium. The diluted NP solution was then taken in a quartz cuvette of optical path length 1 cm and inserted inside the spectrophotometer. All the spectra were obtained at room temperature.

### 2.3.4 3D FDTD simulation

In order to understand the near field distributions of the electromagnetic field and SERS enhancements of the synthesized NPs, we performed 3D FDTD simulation, from Lumerical FDTD Solutions, Canada. The NPs were modeled according to their structures and materials using the material database available in the software. As in the SERS experiment, the NPs were in the aqueous solution of analytes, so the background refractive index was fixed as 1.3. We have placed a total field scattered field plane-wave source as the excitation source with the injection plane and the polarization plane along z and x direction respectively. The excitation wavelength was set to 532 nm during all of the FDTD simulations as we have used the same excitation wavelength during the SERS experiments. We had set the total simulation region as a  $1000 \times 1000 \times 1500 \text{ nm}^3$  cubical space, and used periodic boundary conditions. To decay the energy field fully during the simulation, the simulation time was set to 500 fs. We had used a  $1.5 \times 1.5 \times 1.5 \text{ nm}^3$  mesh throughout all of the simulations. To visualize the electric field intensity maps around the NPs, we have placed three separate field monitors around the NPs at y-z, x-z, and x-y planes, respectively.

### 2.3.5 Cyclic voltammetry (CV)

Due to higher sensitivity, detection ability, experimental simplicity and low cost, electrochemical sensors are very useful compared to other sensors like optical, mass and thermal sensors. Electrochemical sensors are now being used in various fields such as clinical, industrial, environmental and agricultural fields. Both cyclic voltammetric and amperometric studies were performed using a CHI 660C electrochemical workstation from CH Instruments, USA. The electrochemical workstation has three electrodes; a reference electrode, a counter electrode and a working elec-

trode. The electrodes are immersed in an electrolyte solution, where the analytes to be detected are added. We have discussed about the various properties of the electrodes and supporting electrolyte below.

**Electrolyte solution:** Other than the analytes, the electrolyte solution contains a solvent and the supporting electrolyte for example inert salts. In our work, we have used water as solvent and  $\text{Na}_2\text{SO}_4$  as the supporting electrolyte. Hence, the electrolyte solution is a 0.1 M  $\text{Na}_2\text{SO}_4$  aqueous solution. The supporting electrolyte helps in charge transportation through the electrolyte solution and completes the circuit of the cell. The solvent and the supporting electrolyte are chosen such that they should not react between themselves. The properties of a good electrolyte solution are:

- It is highly pure and has a wide liquid range.
- The analyte must be dissolved in it.
- It must not react with the analyte, the electrodes and the products of the redox reaction.
- It must be stable on acid base treatment.
- It has a sufficient potential window for the redox reaction.

The supporting electrolyte increases the conductivity of the solution as well as minimizes the uncompensated internal resistance drop between the working electrode and the reference electrode.

**Reference electrode:** A reference electrode is maintained at a stable and well defined electrochemical potential. The potentials in an electrochemical cell are measured with respect to the potential of the reference electrode. It acts as a reference in controlling and measuring the potential of the working electrode in voltammetric experiments. Here are the few properties of the reference electrode:

- The reference electrode is an ideally non-polarizable electrode. If the current flow changes, it should maintain a constant potential. But, such an ideal reference electrode is not available in reality. In reality, the electrode is chosen such that, for a small amount of current it maintains a constant potential.
- The potential developed at the reference electrode due to the electrochemical reaction should be reversible. The potential is calculated using the Nernst equation [394].
- The potential of the reference electrode should be constant at constant temperature with time.

Here we have used a silver-silver chloride electrode (Ag/AgCl) as the reference electrode with standard potential  $E^0 = 0.230 \pm 0.01$  V against the standard hydrogen electrode (SHE).

**Counter electrode:** The counter electrode acts as the current collector in the electrochemical workstation. The current flows between the counter electrode and the working electrode, where the counter electrode acts as anode. The reaction occurs at the counter electrode is opposite to the reaction occurs in the working electrode. The main properties of the counter electrode are:

- It must not react with the experimental solution.
- The reaction products due to the reaction at the counter electrode must not react with the working electrode.
- The area of the counter electrode should be much larger than the area of the working electrode. Otherwise, the counter electrode could not able to control the limiting current.

Here we have used a platinum (Pt) wire as the counter electrode. The wire is kept inside a glass tube which isolates the counter electrode from the test solution.

**Working electrode:** A potential is applied to the working electrode with respect to the reference electrode, to carry out the electrochemical reactions of the analyte. The working electrode has a definite potential window in a particular supporting electrolyte solution. Within this potential window, only the faradaic current can flow which is generated due to the charge transfer occurring from the redox reaction of the analyte. No other charge transfer occurs across the electrode-solution interface in that particular potential window. The properties of a working electrode are:

- Long term stability.
- Highly pure and reproducible surface.
- Easy renewability of the surface.

There are various kinds of working electrodes. They can be categorized as:

- Metal solid electrodes, (Examples: Pt, Au, Ag, lead electrodes.)
- Carbon based solid electrodes, (Examples: Glassy carbon/ vitreous carbon electrode, carbon paste electrode, diamond electrode.)
- Liquid electrodes and (Examples: mercury drop electrode)
- Conducting film electrodes.

In our work, we have used a conducting film electrode as the working electrode. It is an ITO (indium tin oxide) coated ( $1 \times 1$ ) cm<sup>2</sup> glass slide on which the NPs are deposited. The ITO coated glass slides were first cleaned by ultrasonication in ethanol for 10 min and dried in air. Then, 50  $\mu$ L of the 10-fold diluted (in water) NP solutions were dropcasted on the slides to get a homogeneous film of the NPs on ITO film. After that, they were dried overnight under vacuum.

## STATEMENT BY AUTHOR

This dissertation has been submitted in partial fulfillment of requirements for an advanced degree at Homi Bhabha National Institute (HBNI) and is deposited in the Library to be made available to borrowers under rules of the HBNI.

Brief quotations from this dissertation are allowable without special permission, provided that accurate acknowledgement of source is made. Requests for permission for extended quotation from or reproduction of this manuscript in whole or in part may be granted by the Competent Authority of HBNI when in his or her judgment the proposed use of the material is in the interests of scholarship. In all other instances, however, permission must be obtained from the author.



---

Gourab Bhattacharjee

## DECLARATION

I, hereby declare that the investigation presented in the thesis has been carried out by me. The work is original and has not been submitted earlier as a whole or in part for a degree / diploma at this or any other Institution / University.

*Gourab Bhattacharjee*

---

Gourab Bhattacharjee

## List of Publications arising from the thesis

### Peer reviewed journals:

1. CoreShell Gold@Silver Nanorods of Varying Length for High Surface-Enhanced Raman Scattering Enhancement.

**Gourab Bhattacharjee**, Maireyee Bhattacharya, Abhijit Roy, Dulal Senapati and Biswarup Satpati, *ACS Appl. Nano Mater.*, **2018**, 1(10), 5589–5600.

2. Core-Shell Gold @Silver Hollow Nanocubes for Higher SERS Enhancement and Non-Enzymatic Biosensor.

**Gourab Bhattacharjee**, Sumit Majumder, Dulal Senapati, Sangam Banerjee and Biswarup Satpati, *Mater. Chem. Phys.*, **2020**, 239, 122113.

### Conference proceedings:

1. Synthesis of Parallel and Antiparallel Core-Shell Triangular Nanoparticles.

**Gourab Bhattacharjee** and Biswarup Satpati, *AIP Conference Proceedings*, **2018**, 1942(1), 050112.

2. Synthesis of Core-Shell Nanocubes for Higher SERS Enhancement.

**Gourab Bhattacharjee** and Biswarup Satpati, *AIP Conference Proceedings*, **2019**, 2115(1), 030086.



---

Gourab Bhattacharjee

*To my “Family”*

## ACKNOWLEDGMENTS

Some feats cannot be accomplished alone. Similarly, this thesis would not have been accomplished without the assistance and inspiration of many people including my guide, colleagues and friends supported in many ways to the successful completion of this thesis.

First and Foremost, I would like to express my earnest gratitude to my research advisor Dr. Biswarup Satpati for his continuous encouragement, patience, inspiration and passion. His immense knowledge and experience helped me a lot during my Ph.D. course.

I am also grateful to my doctoral committee members, Prof. Satyaranjan Bhattacharyya, Prof. Tapas Kumar Chini, Prof. Dulal Senapati and Dr. Prasanta Karmakar for their useful suggestions and continuous encouragement.

Special thanks to my collaborators Dr. Maireyee Bhattacharya, Prof. Sangam Banerjee and Dr. Sumit Majumder for their helpful advices and support. I would also like to acknowledge my lab members Tanmay da, Tapas da, Abhijit, Bipasha, Suchanda, Smrutimedha, Tukai and Suman for their help and support.

A considerable amount of time of my PhD life have spent with seniors, friends and juniors. I wish to thank Achyut da, Arpan da, Sudeshna Di, Suman, Anway, Arghya, Ratnadwip, Bankim, Avik, Subha, Montu, Udit, Sandip, Astik, Sabyasachi, Abhishek, Tanmay, Moushri, Sayak, Apurba, Snehal, Bibhuti for being with me and being supportive.

I express my heartfelt gratitude and indebtedness to my parents Shri Gopal Bhattacharjee and Smt. Dipali Bhattacharjee, my sister Dipti for endless love and support. Last but not the least, I want to thank Moumita, my best friend and enemy, for being supportive and compassionate during this journey.

SINP, Kolkata

May, 2020

Gourab Bhattacharjee

## Chapter 4

# Localized surface plasmon and near electric field studies using SERS

---

---

*In this chapter we have discussed about the LSPR properties of different core-shell nanoparticles, calculated the SERS enhancement factor and compared the results with theoretical simulation.*

---

---

## 4.1 Introduction

When electromagnetic rays interact with metallic NPs, the electron clouds of the NPs start oscillating due to the interaction between the electric field of the incoming electromagnetic rays with the electron clouds of the NPs. These collective oscillations of the electron clouds do not propagate, rather it remains confined only into the particle dimension. This phenomenon is known as LSPR since the plasmons are localized. When the electron clouds collectively oscillate due to the incident electric field at a certain resonant frequency, the light is absorbed and later released by the NPs in all directions. This is known as scattering. Whereas some part of the absorbed light is converted into phonons, which cause vibrations in the lattices. This is referred to as absorption [411, 412]. This implies the absorption spectra can manifest the LSPR properties of the NPs. From the absorption spectra we can also get the information about different properties of the NPs like composition and color of the compound, band gap, purity, etc. [413].

Raman effect was discovered in 1928 by Sir C. V. Raman. It refers to the inelastic scattering of photons by any matter, which implies the exchange of energy between the matter and the interacting photons, resulting in a change in the direction of photons. Hence, the molecular vibration energy levels take part in this process. If the vibration energy band gains energy from the photons, then the process is called Stokes Raman effect and if it loses its energy, then the process is called anti-Stokes Raman effect [414]. The intensity of the Raman scattering collected by a detector is given by

$$I_S = \frac{8\pi^4\alpha^2}{\lambda^4r^2}(1 + \cos^2\theta)I_0 \quad (4.1)$$

where  $I_0$  and  $\lambda$  are the intensity and wavelength of the incident photons,  $\alpha$  is the polarizability of the molecule,  $r$  is the distance between the center of scattering and

detector and  $\theta$  is the angle between the incident and scattered photons.

SERS was originally discovered much later in the 1970s, when it was observed that the Raman intensities have been enhanced from the pyridine absorbed on Ag NPs [415]. These enhancements in Raman intensities arise due to the increase of the local electric field around the metallic NPs. Again, the enhancement of this local electric field depends on many factors like the wavelength, direction of polarization and incidence of the interacting electromagnetic rays, collection angle of the detector, Raman cross-section of the molecules, the optical properties of the SERS substrate and on the dielectric constant of the surrounding medium of the NPs [358]. When a far-field electromagnetic ray falls upon a metallic nanomaterial, the LSPR band is excited and starts oscillating. The oscillating LSPR band then re-radiates into far-field electromagnetic rays [313]. In general, the electric field around the NPs is distributed non-uniformly, and highly localized at the sharp edges, tips, corners and nano-gaps of the nanomaterials [388, 416–418]. These regions with highly localized electric fields are called “hot spots”.

The SERS enhancement has contributions from both electromagnetic enhancement and chemical enhancement. But generally the chemical enhancement is much smaller than electromagnetic counterpart and can be neglected. Again, the electromagnetic enhancement has two parts: local field enhancement and radiation enhancement [313, 358]. It could be shown that the power enhancement factor due to the interacting electromagnetic ray of frequency  $\omega_0$  at a point  $r$  could be given by

$$M_{loc}(\omega_0, r) = \left| \frac{E_{loc}(\omega_0, r)}{E_0(\omega_0, r)} \right|^2 \quad (4.2)$$

Here,  $E_{loc}(\omega_0, r)$  and  $E_0(\omega_0, r)$  are the local and incident electric field strengths, respectively.

If  $\omega_R$  be the resonance frequency of the LSPR band, then the radiation en-

hancement at  $r$  due to the incident electric field with frequency  $\omega_0$  could be given by

$$M_{rad}(\omega, r) \approx \left| \frac{E_{loc}(\omega_R, r)}{E_0(\omega_R, r)} \right|^2 \approx \left| \frac{E_{loc}(\omega_0, r)}{E_0(\omega_0, r)} \right|^2 \quad (4.3)$$

Here,  $E_{loc}(\omega_R, r)$  is the local electric field produced by the interacting electric field  $E_0(\omega_R, r)$  at the resonant frequency of  $\omega_R$ . Therefore, the SERS EF at resonant frequency  $\omega_R$  due to the incoming electromagnetic rays with frequency  $\omega_0$  is given by

$$EF(\omega_0, \omega_R, r) = M_{loc}(\omega_0, r)M_{rad}(\omega, r) \approx \left| \frac{E_{loc}(\omega_0, r)}{E_0(\omega_0, r)} \right|^4 \quad (4.4)$$

So, from the equation 4.4, it is found that the SERS EF is proportional to the 4<sup>th</sup> power of local field enhancement. In FDTD simulation, we formed models of metallic NPs and excite them with a plane wave source. Then the local electric field around the NPs was mapped using the simulation. From the information of this local electric field, the EF was calculated from the simulation.

## 4.2 UV-Vis-NIR spectroscopy of different NPs

The absorption spectra of NPs are very useful as they reflect many properties of the NPs, like the shape and size of the NPs as well as the band gap and LSPR band. From the information about the LSPR band, we can find out which types of NPs are more suitable as SERS substrate, as the SERS EF depends on the wavelength of both LSPR and incident electromagnetic rays. In our studies, the absorption spectra of the NPs were acquired over a wide range from ultra violet (UV) (200 nm) to near infra-red (NIR) (1400 nm) region. As the synthesized NPs were dispersed into water medium in colloidal form, we had to acquire the spectra

in the water medium. Hence, in order to acquire the absorption spectra, we had to restrict ourselves between 200 – 1400 nm range, because the absorption of water is much higher ( $>1$ ) below 250 nm and above 1400 nm [419] and the contribution from the water would dominate over the contribution of the NPs in the region outside 200 – 1400 nm. That is the only reason behind acquiring the absorption spectra in the said range mentioned above. There might exist SPR modes beyond this range, but we could not observe them in water medium.

### 4.2.1 Au@Ag NRs

To find out how the changes in lengths or aspect ratios of these Au@Ag core-shell NRs affect the SPR, we have acquired absorption spectra of the Au@Ag NRs and Ag NRs over a wide range of 250–1400 nm. The obtained absorption spectra for Au NBPs, Au@Ag NRs of different lengths along with the monometallic Ag NRs are presented in the Figure 4.1. The absorption spectrum of Au NBPs shows two higher absorption peaks at 527 nm and 667 nm, respectively. Besides there exists a small peak around 363 nm. The plasmon peak at 667 nm has originated due to the pure dipolar longitudinal mode. The plasmon band appeared at 527 nm has originated due to the first dipolar transverse mode ( $DT_1$ ) arising from the pentagonal bases of the Au NBPs. The plasmon band at 363 nm has originated due to the second dipolar transverse mode ( $DT_2$ ) arising from the tips of the Au NBPs. Now, the length ( $42 \pm 5$  nm) and width of the pentagonal bases ( $17 \pm 3$  nm) are much larger than the diameter of the tips of the Au NBPs, so the absorption cross-section is highest for the pure dipolar longitudinal mode as it arises along the length of the Au NBPs and lowest for the second dipolar transverse mode ( $DT_2$ ) as it arises from the tips. The absorption cross-section for the first dipolar transverse mode ( $DT_1$ ) falls in between them.

From the UV-vis-NIR spectra (Figure 4.1) one can notice that there exist more

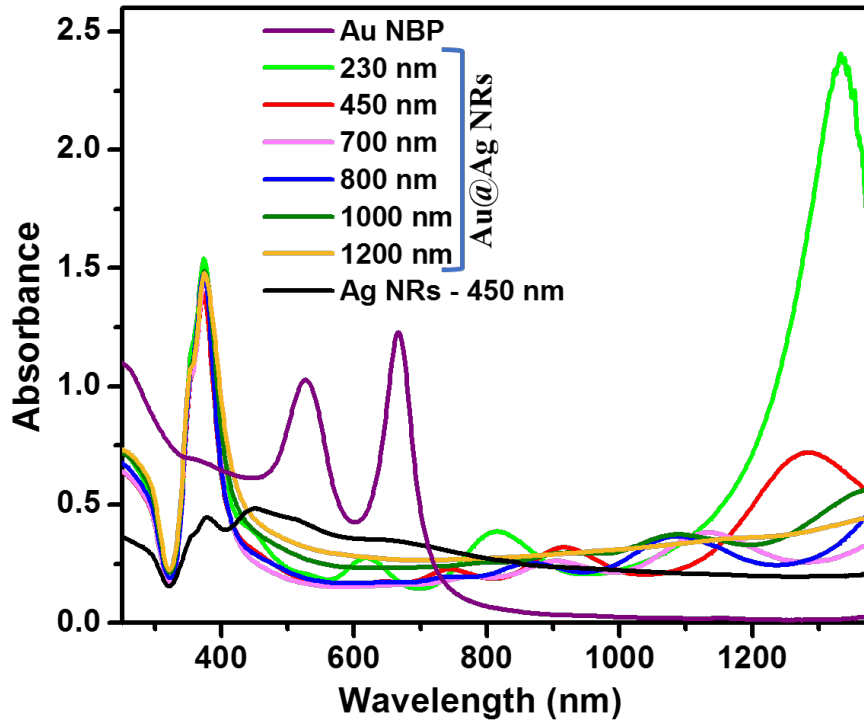


Figure 4.1: Absorption spectra of Au NBPs, Au@Ag core-shell NRs of different lengths and Ag NRs.

number of peaks in the absorption spectra of Au@Ag NRs compared to Ag NRs, which implies that the Au@Ag core-shell NRs show highly structured multiple plasmon bands compared to the Ag NRs throughout the absorption spectra. There exist two common peaks at the wavelengths of 355 nm and 374 nm for both types of NRs. The peak around 355 nm has originated from the SPR of bulk Ag [420]. The peak at 374 nm has originated due to the quadrupolar transverse SPR for Ag NRs and Au@Ag NRs [420]. It is well known that if the dimension of any NP is of the order or higher than one tenth of the wavelength ( $\geq \lambda/10$ ) of the electromagnetic wave falling on the NP, then other higher order modes like quadrupolar, octapolar, etc. become active beside the dipolar modes of the NP. For this reason, we could observe multiple absorption peaks at the higher wavelength region of the spectra. In the absorption spectrum of Ag NRs, there exist three absorption peaks at 448 nm, 514 nm

and 645 nm, respectively. The peaks could be assigned as dipolar transverse (DT), quadrupolar longitudinal (QL), and dipolar longitudinal (DL) modes for Ag, respectively. In the case of Au@Ag NRs of length 230 nm, we could observe more peaks in the absorption spectra from UV to NIR region compared to the monometallic Ag NRs. Whereas, there exists no absorption band in the NIR region for Ag NRs. The probable reasons could be:

- the absorption band exists outside the region we are observing, i.e., the band gap for the longitudinal plasmon band of monometallic Ag NR is present at much higher or lower energy,
- the enhanced metal to metal charge transfer due to the lattice mismatch for bimetallic NPs is absent in the case of a monometallic Ag NR.

For any plasmonic NP, the SPR wavelength depends on many factors like, the radius of the NP, composition of the material and refractive index of the medium. As the size of the NP increases, we could observe a red shift in the SPR band. According to Mie-Gans theory [421], the polarizability of any NP highly depends on both of its shape and size. So, the SPR wavelength can be varied by varying its shape or size, either independently or simultaneously. But, when the symmetry of any NP is broken, the NP gains additional SPR modes. For the case of NRs, we could observe two absorption bands, and they are due to the transverse and longitudinal SPR, respectively [422]. In the Figure 4.2, we have demonstrated the visualization of two SPR modes for an NR.

Comparing the two models presented in the Figure 4.2, one can conclude that the NR is more easily polarized longitudinally with a higher absorption cross section than transversely. So, the longitudinal SPR occurs at lower energy or higher wavelength with greater optical density. When the length of an NR is increased for a fixed diameter, both the longitudinal and transverse SPR are affected. But as

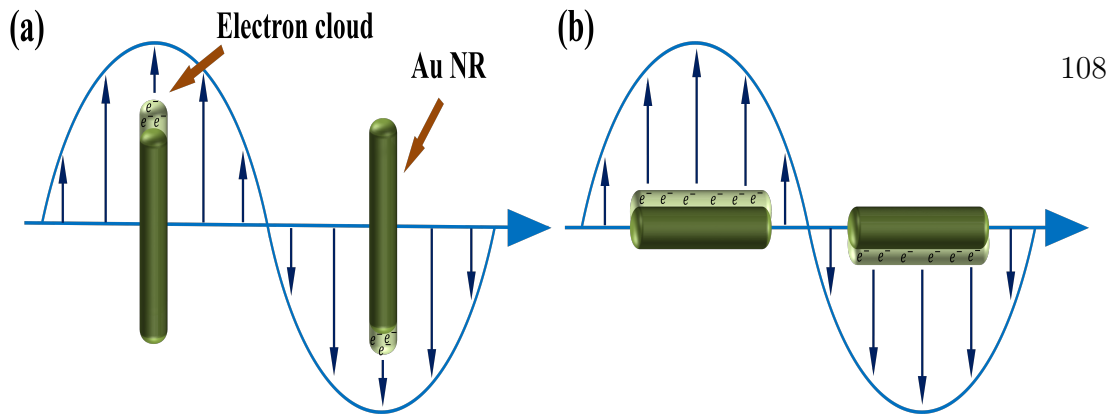


Figure 4.2: (a) Longitudinal SPR (LSPR) and (b) transverse SPR (TSPR).

the longitudinal SPR is easily polarizable, it shifts more compared to the transverse SPR. In conclusion, as the length of the NR is varied over a wide region, the longitudinal SPR varies over a wide range; from visible to NIR region. Whereas, we could observe a little shift for the case of transverse SPR.

For core-shell NRs of length 230 nm, besides the peaks at 355 and 374 nm common to monometallic Ag NRs, there exist additional absorption peaks at 445, 528, 621, 815, and 1340 nm respectively. As there is no plasmon band observed in the NIR region for both Au NBPs and Ag NRs, the plasmon band at the NIR region, for example the SPR at 1340 nm for Au@Ag NRs of length 230 nm might be originated from the coupling between Au and Ag. So, we could assign the peak at 1340 nm as the coupled dipolar longitudinal (CDL) mode which has been originated due to the effective spatial coupling between the Au DL and Ag DL modes. For Au@Ag NRs of different lengths, the coupling is maximum for a shorter length of Ag shells. As a result, we have got maximum CDL absorption strength for Au@Ag NRs of length 230 nm, and as the length increased, the absorption cross section decreased. Hence, we can observe a significant reduction in the CDL absorption strength with the increasing length of the NRs. Though the lengths of the Au@Ag NRs have been varied over a wide range, we could hardly observe any change in their diameter as it varied from 27 nm to 35 nm. Hence, the contributions from the higher order transverse modes are almost negligible.



For Au@Ag NRs of length 230 nm, the 7 absorption peaks at 355, 374, 445, 528, 621, 815, and 1340 nm can be assigned as bulk Ag, quadrupolar transverse of Ag (QT), dipolar transverse of Ag (DT), dipolar transverse of Au (DT) + quadrupolar longitudinal of Ag (QL), dipolar longitudinal of Ag (DL), dipolar longitudinal of Au (DL) and coupled dipolar longitudinal between Au and Ag (CDL) respectively. The coupled dipolar transverse (CDT) mode could also be generated due to the coupling between the dipolar transverse mode of core Au NBP and shell Ag NR similar to the coupled dipolar longitudinal mode, and they are highly accessible. Again, as the lengths of the NRs have increased, higher order coupled dipolar transverse (CDT) modes have started appearing in the range between 800 to 1100 nm. As the diameters of the Au@Ag NRs have increased with increasing lengths, the contribution from the transverse mode has increased, and also the coupled dipolar transverse (CDT) modes have red shifted which is clearly observable from the absorption spectra. So, we could conclude that the absorption peaks above 820 nm (i.e., in the NIR region) have not originated from the longitudinal plasmon band of the Ag nano-shell of the Au@Ag NRs, rather due to the different extents of plasmon coupling between the longitudinal and transverse modes of the core Au NBPs and shell Ag NRs in the Au@Ag NRs. As the lengths of the Au@Ag NR have increased, we have clearly observed that all of the multipolar transverse and longitudinal peaks have red-shifted as well as a reduction in the peak intensities. This is the main reason behind the absence of any peak in the absorption spectra for Au@Ag NR of length 1200 nm, because all the multipolar transverse and longitudinal peaks have red-shifted beyond our observable limit of 1400 nm as well as the intensities of the peaks have decreased so much that they are hard to identify. We have provided a list of the peaks in the UV-vis-NIR absorption spectra of Ag NRs and Au@Ag NRs of different lengths with their peak positions (nm), their origin and strength of the peaks in the Table 4.1, where DT, DL, QT, QL, CDT, and CDL stand for the dipolar transverse, dipolar longitudinal, quadrupolar transverse, quadrupolar

longitudinal, coupled dipolar transverse, and coupled dipolar longitudinal modes, respectively. The strengths of the peaks are identified as S, W, and VW, where they stand for strong, weak and very weak, respectively.

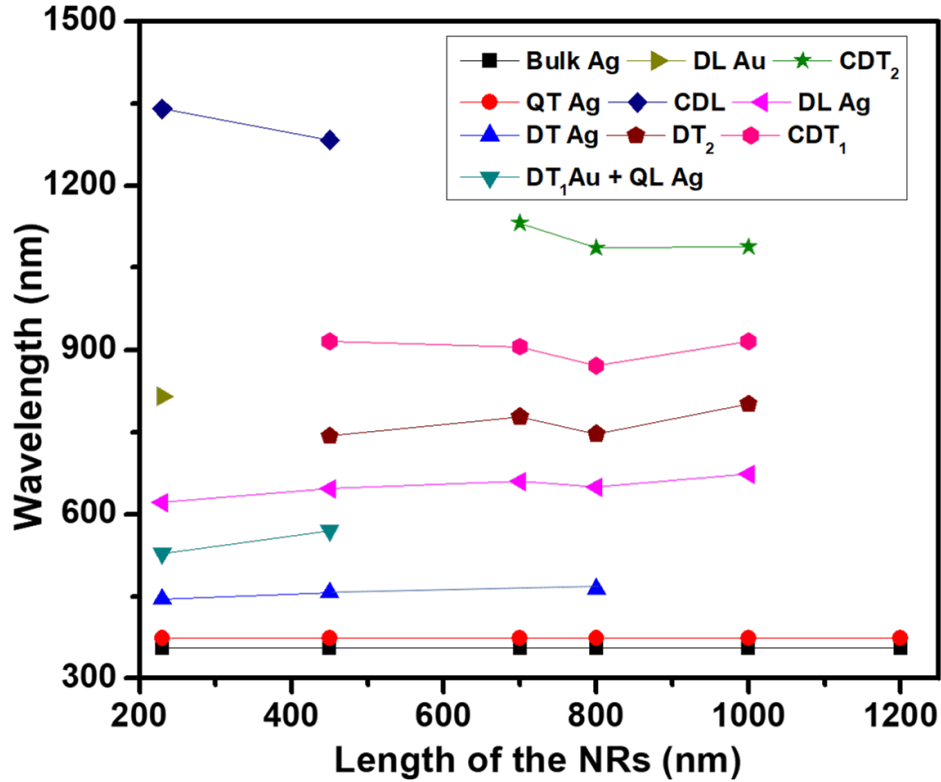


Figure 4.3: *Dependence of the plasmon modes on the lengths of the Au@Ag NRs.*

For Au@Ag core-shell NR, as the core Au NBPs were completely covered by the Ag NR shells, the incoming electromagnetic radiation could not be able to penetrate the Ag shells to reach the Au NBPs. As a result, the optical properties due to the pure Au cores have diminished, and due to the very small lattice mismatch between the core Au NBPs and shell Ag NRs, the coupled modes have intensified which supports easy plasmon coupling. Therefore, we can vary the LSPR band of the Au@Ag NRs over a wide range from the UV to NIR region by only changing their length or the aspect ratio. From the absorption spectra in the Figure 4.1 or the Table 4.1, one can observe that as the length of the Au@Ag NRs has been increased, the absorption peaks have also red shifted. But in the case of Au@Ag NRs of length 800

nm, we could observe that some of the absorption peaks have blue-shifted compared to the Au@Ag NRs of length 700 nm. Although Au@Ag NRs of length 800 nm have greater surface area and plasmon band closer to the excitation wavelength compared to Au@Ag NRs of length 700 nm. These discrepancies may arise due to the fact that there is a larger distribution of length for Au@Ag NRs of length 800 nm compared to Au@Ag NRs of any other length. Again these Au@Ag NRs of length 800 nm are not also in regular shape compared to the remaining NRs. In the Figure 4.3, we have presented how the different plasmon modes depend on the length of the Au@Ag NRs. One can clearly observe that with the increasing length of the Au@Ag NRs, the plasmon bands have been also red shifted.

#### 4.2.2 Core-shell NSs, NCs, HNSs and HNCs

UV-vis-NIR absorption spectra were acquired to investigate how the SPR of these Au@Ag core-shell NPs change with morphology. In the Figure 4.4, we have presented the UV-vis-NIR spectra of the Au TOH NPs and other four types of Au@Ag core-shell NPs, i.e., NSs, NCs, HNSs and HNCs respectively. From the absorption spectrum of Au TOH NPs, we can observe there exists a very high absorption peak around 595 nm. It can be assigned as the dipolar LSPR for the Au TOH NPs [416]. We know that if the size of any NP is large enough ( $\approx 100$  nm), then besides the contribution from the dipolar LSPR, the contribution from the higher order LSPR also comes into the picture due to the phase retardation effects [423]. Therefore, the absorption peak observed at 396 nm in the spectra can be originated due to the contribution from the quadrupolar LSPR. The small absorption peak at 292 nm can be assigned as the SPR of the bulk Au [424].

From the absorption spectra of all the four types of core-shell NPs, we can observe that there exist two common plasmon peaks at 243 nm and 290 nm respectively. Again, if the size of any NP is comparable to the wavelength of the

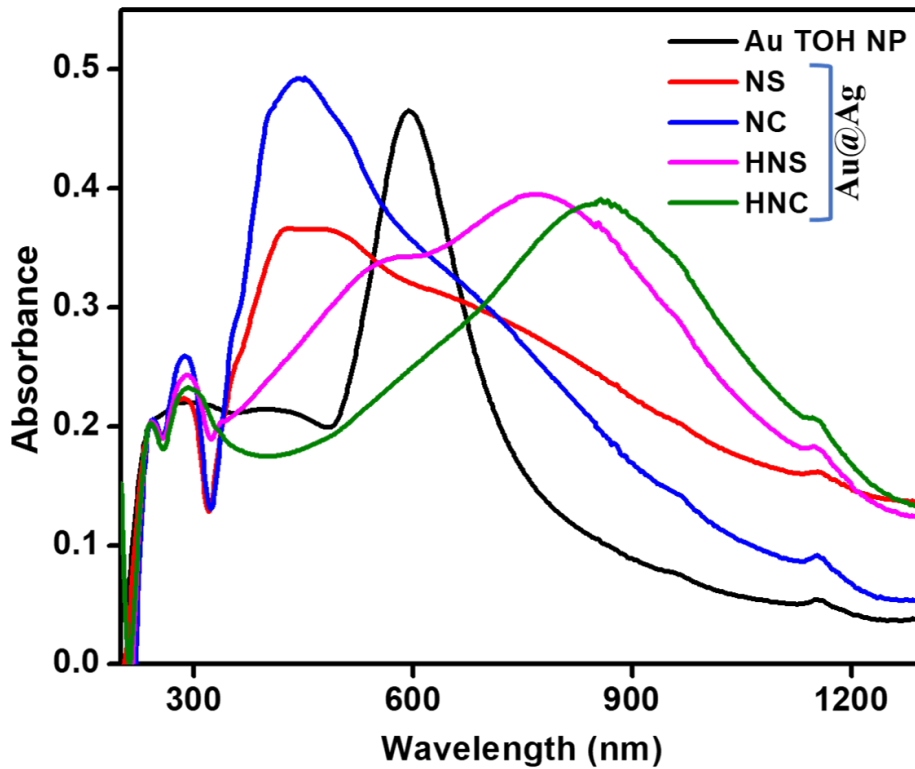


Figure 4.4: Absorption spectra of Au TOH NPs and Au@Ag core-shell NSs, NCs, HNSs and HNCs.

electromagnetic wave interaction with the NP ( $\geq \lambda/10$ ), then the other higher order modes like quadrupolar, octapolar, etc. also become active besides the other dipolar modes. So, the absorption peaks at 243 nm and 290 nm can be assigned as the higher order transverse SPRs for Ag counterpart of the Au@Ag NPs and it is clear that these higher order LSPRs are very less sensitive on the shape and size of the NPs [420]. On contrary, the dipolar LSPRs are more sensitive to the shape and size of the NPs [388]. Apart from those peaks at low wavelength region, there also exists a small hump at around 354 nm common to the absorption spectra for all four core-shell NPs. This is originated due to the SPR of bulk Ag [420].

Comparing the absorption spectra of the Au@Ag NSs and NCs, we can observe that there exists a high absorption peak at the lower wavelength side, at 427 nm and 439 nm respectively, and a very low absorption peak at 743 nm and 698 nm,

respectively. The absorption peaks at the lower wavelength have originated due to the dipolar LSPR of the Ag counterpart of the Au@Ag NPs. And the absorption peaks at higher wavelength correspond to the coupled LSPR modes between the core Au and shell Ag part of the NPs. From these observations, we can conclude that for Au@Ag NSs and NCs, i.e., core-shell NPs with solid Ag shell, the contribution in the absorption spectra from the Ag part is more dominant than the contribution due to the coupling part. As in these cases, the core Au is completely covered by the Ag shell, the incoming electromagnetic wave could not penetrate the solid Ag shell. As a result, we have got more contributions from the shell Ag part of the NPs in the absorption spectra. Whereas, in the case of core-shell NPs with hollow shells, i.e., Au@Ag HNSs and HNCs, the fact is completely opposite. From the absorption spectra of Au@Ag HNSs and HNCs, we can observe that there exists a very low absorption peak at lower wavelength region, at 559 nm and 623 nm respectively, which is due to the dipolar LSPR of Ag part of the NPs. But there exists a very strong absorption peak at the higher wavelength region, at 765 nm and 855 nm respectively, which has originated due to the coupling of LSPR between Au and Ag part in the NPs. In these cases, the shell thickness is very small as it is hollow in nature, so the incident electromagnetic radiation could penetrate the hollow shell easily, and interact with the core Au TOH. Due to this fact, the contribution due to the Ag shell is very small compared to the coupled mode as it gets intensified due to the very small lattice mismatch in the crystalline structure of Au and Ag, which also supports easy plasmon coupling.

### 4.3 SERS activity

The strength of the LSPR in all the synthesized NPs had been studied by collecting the SERS spectra by using different analytes. As we had synthesized the core-shell NPs in long-chain surfactant medium like CTAB or CTAC, the added

analyte molecules could not be able to reach the surfaces of the NPs as closely as they could for the case of surfactants with small molecules like trisodium citrate, ascorbic acid, etc. To overcome this limitation, we had used analytes with electron-rich ligand which would effectively bond with the positively charged head-group  $N_{(\text{CH}_3)_3}^+$  of CTAC. Thus, the accessibility of the surfaces to the analyte molecules would be increased. Here we had used different analytes like 4-mercaptobenzoic acid (4-MBA), crystal violet (CrV) and 4-mercaptopyridine (4-MPy) to collect the SERS spectra. Even after 30 min of the addition of these analytes with the NPs, the solutions did not show any signature of aggregation, which ruled out efficient coupling between the nanostructures and the molecules of the analytes. Which implies that the contribution from the chemical enhancement had no role in the total Raman cross section. Hence, the observed SERS spectra could be explained entirely by an evanescent-field-induced electromagnetic enhancement mechanism [425].

### 4.3.1 Core-shell NRs

We had collected the SERS spectra for Au@Ag NRs of different lengths using 4-MBA, CrV and 4-MPy respectively as analytes and investigated the change in Raman activity with the length of the Au@Ag NRs. In the Figure 4.5, we have presented the acquired SERS spectra for Au@Ag of different length using  $2 \times 10^{-4}$  M 4-MBA as analyte. We had observed a reduction in the Raman activity as the length of the Au@Ag NRs was increased. The plasmon band close to the excitation wavelength had diminished or red shifted with the increasing length of the Au@Ag NRs. So, the reduction in Raman activity is expected. But in the case for Au@Ag NRs of length 230 nm and 450 nm, it was observed that Au@Ag NRs of length 450 nm had greater SERS activity compared to the Au@Ag NRs of length 230 nm, though Au@Ag NRs of length 230 nm have a much larger contribution from  $DT_1(\text{Au}) + QL(\text{Ag})$ , and which is also close to the excitation wavelength. If we consider the

plasmon contributions for Au@Ag NRs of length 230 nm and 450 nm separately, then obviously the Au@Ag NRs of length 230 nm should give much better Raman scattering compared to the Au@Ag NRs of length 450 nm. But if we compare the surface area of those Au@Ag NRs, then obviously the Au@Ag NRs of length 450 nm have a bigger surface area compared to the Au@Ag NRs of length 230 nm  $\left( \frac{A_{450\text{ nm}}}{A_{230\text{ nm}}} = \frac{2\pi r \times 450}{2\pi r \times 230} \approx 2 \right)$ , as a result, large number of analyte molecules got attached to the surface of the Au@Ag NRs of length 450 nm compared to the Au@Ag NRs of length 230 nm. Which resulted in a large SERS signal. For longer Au@Ag NRs, although they could absorb a much higher number of analyte molecules, but showed reasonable Raman cross sections as they did not have any plasmon band near the laser excitation wavelength. Hence, the SERS enhancement offered by an Au@Ag NR not only depends on the plasmon contribution at the excitation wavelength, but it also depends on the effective surface area for the absorption of the analyte molecules.

From the SERS spectra shown in the Figure 4.5, we could observe prominent Raman modes at 526, 805, 1076, 1180, 1385, 1478, and 1592  $cm^{-1}$ , respectively. Two sharp peaks at 1076 and 1592  $cm^{-1}$  in the SERS spectra were originated due to *C-H in-plane bending* and *C=C symmetric stretching vibration*, respectively [426]. The maximum enhancements at 1070 and 1592  $cm^{-1}$  imply the largest interaction of these modes with the plasmonic nanosurfaces. The other relatively weaker Raman modes observed at 526, 1180, 1478, 805, and 1385  $cm^{-1}$  were originated due to the *C-H out-of-plane bending*, *C-H bending*, *ring bending*, *COO<sup>-</sup> bending*, and *COO<sup>-</sup> symmetric stretching*, respectively [426]. Because of the strong affinity of sulfur (S) atoms to the Ag atoms in the shell, 4-MBA molecules most probably bound with the S atoms to the nanosurfaces by keeping the benzene  $\pi$  cloud perpendicular to the free electron cloud of the Au@Ag NRs and the COOH group at the distant end. As the Ag-S stretching mode appears in the range between 250 to 350  $cm^{-1}$  [427], it is very difficult to trace the strong contribution of this mode from the recorded SERS

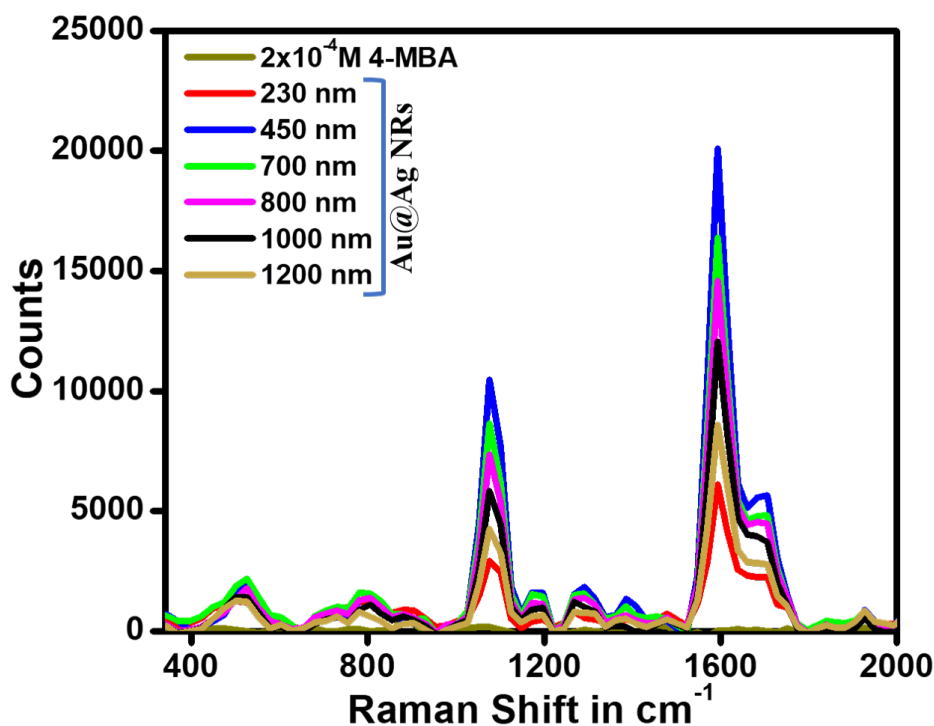


Figure 4.5: *SERS spectra of  $2 \times 10^{-4}$  M 4-MBA mixed with the core-shell Au@Ag NRs of different lengths.*

spectra, because it is masked by Rayleigh scattering. Due to the close proximity and favorable orientation (perpendicular orientation of the benzene group to the surface of the Au@Ag NRs), both *C-H in-plane bending* and *C=C symmetric stretching of the  $\pi$  cloud* brought them close to the nanosurface. As a result they have maximum overlap specifically to enhance them compared to the other modes [426].

In the Figure 4.6, we have presented the obtained SERS spectra for Au@Ag of different lengths using CrV as analyte. The prominent Raman modes had been observed at 448, 557, 805, 919, 1172, 1385, and 1615  $cm^{-1}$ , respectively. The three highest peaks had been observed at 1172, 1385, and 1615  $cm^{-1}$ , which correspond to the *benzene C-H in-plane bending vibration*, *N-phenyl bond stretching vibration* and *benzene C=C stretching vibration* modes respectively. These observations imply maximum interaction of these modes with the CrV molecules absorbed on the surfaces of the Au@Ag NRs. The other relatively weaker Raman modes observed at

448, 805, and  $919\text{ cm}^{-1}$  could be assigned as a combination of the out-of-plane ring skeletal vibration and out-of-plane  $C^+$ –phenyl bond vibration, out-of-plane bending of the  $C$ – $H$  bond and ring skeletal vibration of radial orientation, respectively. The weakest Raman mode observed at  $557\text{ cm}^{-1}$  could be assigned as the benzene ring skeletal vibration of the radial orientation mode [428].

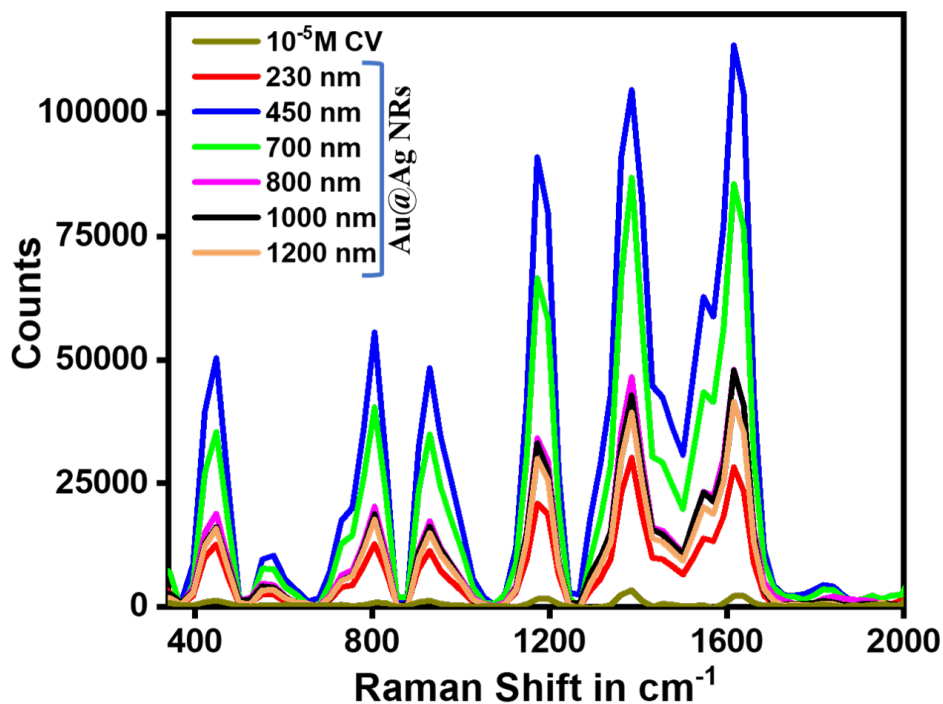


Figure 4.6: SERS spectra of  $10^{-5}\text{ M CrV}$  mixed with the core-shell Au@Ag NRs of different lengths.

Figure 4.7 shows experimentally obtained SERS spectra from 4-MPy adsorbed onto the surfaces of Au@Ag NRs of different lengths. The eminent Raman modes had been observed at 466, 722, 993, 1100, 1220, 1455 and  $1592\text{ cm}^{-1}$  respectively. The maximum SERS enhancements had been observed at 993, 1100, and  $1592\text{ cm}^{-1}$  which represent the strong interaction of those modes with the surfaces of the Au@Ag NRs. The Raman modes observed at 993, 1100, and  $1592\text{ cm}^{-1}$  could be assigned as the ring-breathing mode, ring-breathing mode coupled with the  $C$ – $S$  stretching mode and pyridine ring  $C=C$  stretching modes, respectively. The other relatively weaker modes observed at 466, 722, 1220, and  $1455\text{ cm}^{-1}$  could be assigned as the

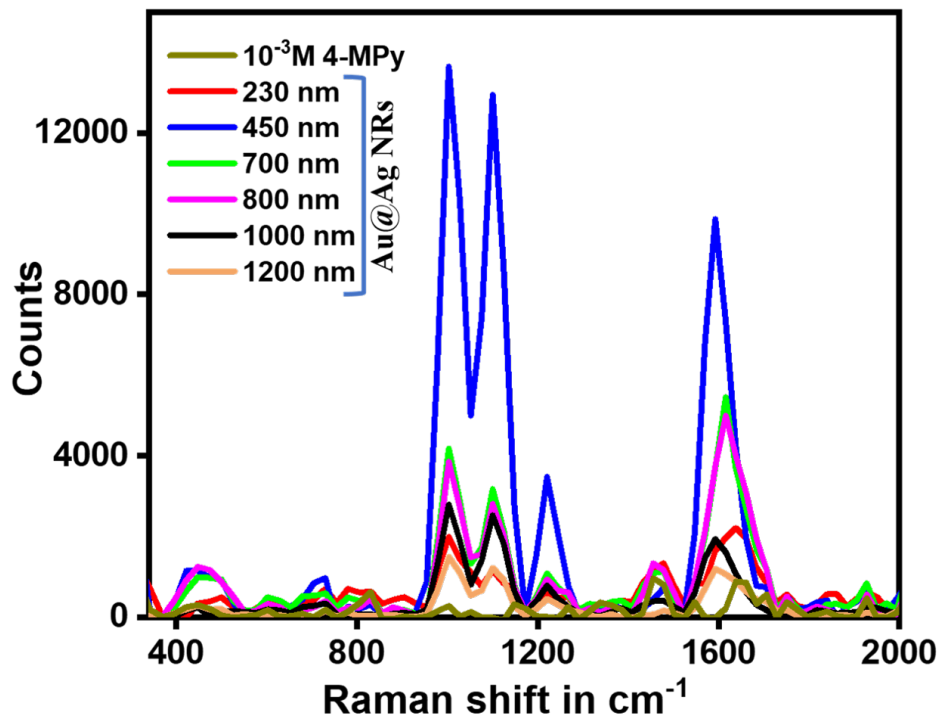


Figure 4.7: SERS spectra of  $10^{-3}$  M 4-MPy mixed with the core-shell Au@Ag NRs of different lengths.

out-of-plane CCC bending mode, a combination of the C=C in-plane bending of the pyridine ring and C-S stretching mode, a combination of the in-plane C-H bending and N-H deformation mode, and a combination of the C=C and C=N stretching mode, respectively [429]. We can clearly observe that in each case, the Raman signal for Au@Ag NRs of length 450 nm is maximum.

In the Figure 4.8, we have presented the SERS spectra of Ag NRs and Au@Ag NRs having almost the same length of about 450 nm in the analyte of  $2 \times 10^{-4}$  M 4-MBA. The spectra clearly show that the SERS enhancement for the Au@Ag NRs is much higher (almost 4 times) than that of a monometallic Ag NRs.

It is well known that the SERS enhancement depends on many factors, like the shape and size of the NPs, the excitation wavelength due to the coupling between the excitation wave and LSPR of the NPs, the presence of sharp edges and tips and also on the existence of lattice strain in the NPs [430]. For the case of Au@Ag NRs,

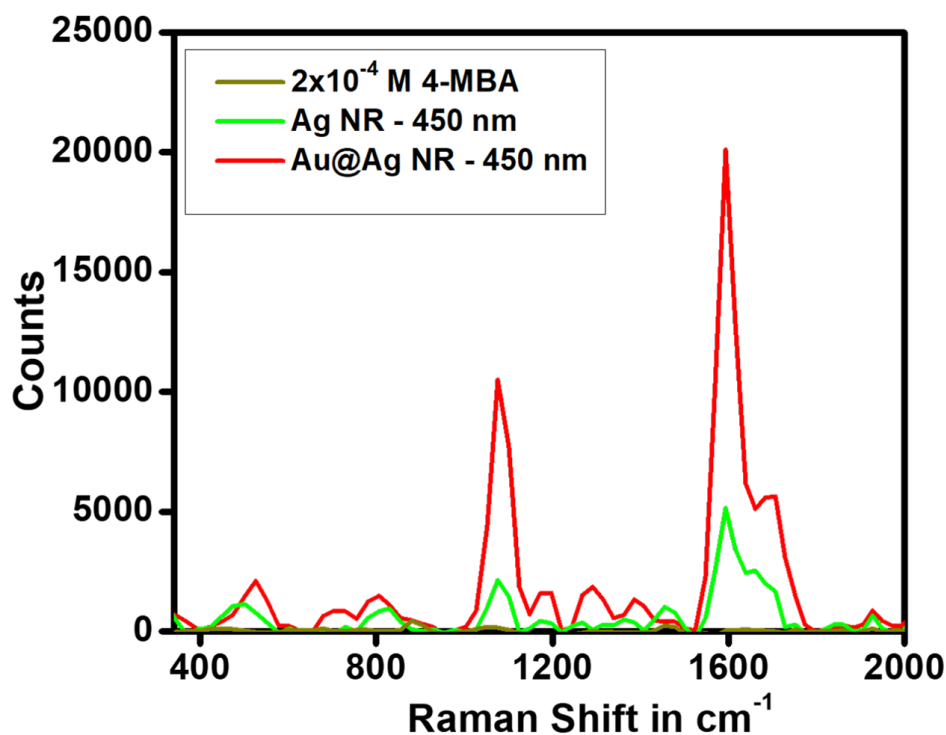


Figure 4.8: SERS spectra of  $2 \times 10^{-4}$  M 4-MBA obtained for Ag NRs and Au@Ag NRs of length 450 nm.

a small lattice mismatch was present at the interface of the core Au and shell Ag, which generated a small strain at the interfaces. Hence the local electric field was increased. Again, due to the presence of multiple sharp edges and tips in the core Au NBP the local electric field was enhanced for the Au@Ag NRs, which was absent for Ag NRs. This electric field drove the SERS enhancement higher than that for Ag NRs because the lattice mismatch was absent here.

### 4.3.2 Calculation of SERS EF

The SERS EF offered by Au@Ag NRs of different lengths and Ag NRs have been calculated for those three different analytes by comparing the SERS signal on the nanosurface and in bulk for some specific Raman modes with higher intensity .

The EF is given by the following expression [388, 416, 431–433]:

$$EF = \frac{I_{SERS}}{I_{bulk}} \times \frac{N_{bulk}}{N_{SERS}} \quad (4.5)$$

Here,  $I_{SERS}$  is the integral intensity of a definite vibration mode in the Raman peak of the analyte in the presence of the Au@Ag NRs in the solution,  $I_{bulk}$  is the integral intensity of that vibration mode in the Raman peak of the analyte alone in the solution,  $N_{bulk}$  is the number of analyte molecules used in the bulk, and  $N_{SERS}$  is the number of analyte molecules absorbed on the surfaces of the Au@Ag NRs.  $N_{bulk}$  can be given by the equation

$$N_{bulk} = \frac{V\rho}{M} N_A \quad (4.6)$$

where,  $N_A$  is the Avogadro number ( $N_A = 6.023 \times 10^{23}$ ),  $\rho$  and  $M$  is the density and the molecular weight of the analyte respectively, and  $V$  is the effective laser excitation volume, given by  $V = \pi r^2 \delta$ . Here,  $r$  is the laser spot radius given by the relation  $r = \frac{1.22\lambda}{NA}$  and  $\delta$  is the depth of focus given by the expression  $\delta = \frac{2\pi}{\lambda} r^2$ , where  $\lambda$  is the excitation wavelength and  $NA$  is the numerical aperture of the laser. For our experimental set-up,  $\lambda = 532$  nm and  $NA = 0.22$ . So,  $r = \frac{1.22\lambda}{NA} = 2.95$   $\mu\text{m}$ , and  $\delta = \frac{2\pi}{\lambda} r^2 = 102.73$   $\mu\text{m}$ . Hence, the effective laser excitation volume is given by

$$V = \pi r^2 \delta = 2.81 \times 10^3 \mu\text{m}^3 = 2.81 \times 10^{-15} \text{m}^3 \quad (4.7)$$

Considering the value of  $V$  and  $N_A$  above,  $N_{bulk}$  can be given by the relation

$$N_{bulk} = \frac{\rho}{M} \times 1.69 \times 10^9 \quad (4.8)$$

To find out the value of  $N_{SERS}$ , we had to find out the number of NRs in the laser excitation volume  $V$ . To synthesize Au@Ag NRs of length 230 nm, we have

added  $v = 3 \text{ mL} = 3 \times 10^{-3} \text{ L}$  of  $c = 10^{-2} \text{ M}$   $\text{AgNO}_3$  into the growth solution. The atomic mass of Ag is  $M_{Ag} = 107.8682 \text{ u}$ . So, the total amount of Ag in the growth solution is  $W_{Ag} = cvM_{Ag} = 3.24 \times 10^{-3} \text{ g}$ .

After the growth was completed, the resultant solution contains both Au@Ag NRs and spherical Au@Ag NPs. The spherical NPs dominate over the NRs as only 10% of the resultant NPs are NRs which is evident from the Figure 3.2. We have collected only the NRs using the purification process. Then the total amount of Ag which contributes to formation of the NRs is  $W_{NR} = 0.1 \times W_{Ag} = 3.24 \times 10^{-4} \text{ g}$ .

Now, the volume of a single NR with diameter  $d_{NR} = 2r_{NR} = 27 \text{ nm}$  and length  $l = 230 \text{ nm}$  is  $v_{NR} \cong \pi \frac{d_{NR}^2}{4} l = 1.32 \times 10^{-4} \mu\text{m}^3$ .

The density of Ag is  $\rho_{Ag} = 10.5 \text{ g.cm}^{-3} = 1.05 \times 10^{-11} \text{ g.}\mu\text{m}^{-3}$ .

As the volume of the core Au NBP is very small compared to the volume of the shell NR, so by neglecting the effect of the core Au NBP, the weight of a single NR of diameter  $d_{NR} = 27 \text{ nm}$  and length  $l = 230 \text{ nm}$  is given by  $w_{NR} = v_{NR}\rho_{Ag} \cong \pi \frac{d_{NR}^2}{4} l \rho_{Ag} = 1.39 \times 10^{-15} \text{ g}$ .

So, the total number of NRs of length  $l = 230 \text{ nm}$  after the centrifugation in the final volume of  $V_S \sim 1 \text{ mL} = 10^{12} \mu\text{m}^3$  is  $N_{NR} = \frac{W_{NR}}{w_{NR}} = 2.34 \times 10^{11}$ .

Hence, the number density of the Au@Ag NRs of length  $l = 230 \text{ nm}$  is  $n_S = \frac{N_{NR}}{V_S} = 2.34 \times 10^{-1} \mu\text{m}^{-3}$ .

To acquire the SERS spectra, we have mixed  $50 \mu\text{L}$  of the NRs solution into  $150 \mu\text{L}$  of analyte solution. Therefore, the number density in the SERS substrate is  $1/4^{\text{th}}$  of the density we have calculated above. Hence, the number density of NRs of length  $l = 230 \text{ nm}$  as SERS substrate is  $n_{NR} = \frac{n_S}{4} = 5.85 \times 10^{-2} \mu\text{m}^{-3}$ .

The effective laser excitation volume was calculated to be  $V = 2.81 \times 10^3 \mu\text{m}^3$ . So, number of Au@Ag NRs of length  $l = 230 \text{ nm}$  inside the laser excitation volume is

$$N = Vn_{NR} \approx 164.$$

Table 4.2: Number density of NRs as SERS substrate.

Samples		Volume of $10^{-2}$ M $\text{AgNO}_3$ in the growth solution ( $v$ ) in mL	Amount of Ag in the NRs ( $W_{NR}$ ) in g	Weight of a single NR ( $w_{NR}$ ) in g	Total number of NRs synthesized ( $N_{NR}$ )	Final volume of the NRs solution ( $V_S$ ) in mL	Density of NRs in SERS substrate ( $n_{NR}$ ) in $\mu\text{m}^{-3}$
Au@Ag NRs of length	230 nm	3	$3.24 \times 10^{-4}$	$1.39 \times 10^{-15}$	$2.34 \times 10^{11}$	1	$5.85 \times 10^{-2}$
	450 nm	5	$5.39 \times 10^{-4}$	$3.12 \times 10^{-15}$	$1.73 \times 10^{11}$	1.5	$2.88 \times 10^{-2}$
	700 nm	7	$7.55 \times 10^{-4}$	$5.91 \times 10^{-15}$	$1.28 \times 10^{11}$	2	$1.60 \times 10^{-2}$
	800 nm	8	$8.63 \times 10^{-4}$	$6.75 \times 10^{-15}$	$1.27 \times 10^{11}$	2.4	$1.33 \times 10^{-2}$
	1000 nm	10	$1.08 \times 10^{-3}$	$8.98 \times 10^{-15}$	$1.20 \times 10^{11}$	3	$1.00 \times 10^{-2}$
	1200 nm	12	$1.29 \times 10^{-3}$	$1.21 \times 10^{-14}$	$1.07 \times 10^{11}$	3.5	$7.63 \times 10^{-3}$
Ag NRs of 450 nm		0.8	$8.63 \times 10^{-5}$	$2.91 \times 10^{-15}$	$2.97 \times 10^{10}$	0.25	$2.97 \times 10^{-2}$

In our whole process (to study SERS spectra of Au@Ag NRs of different lengths), we have maintained the same density of the Ag atoms in each case. To achieve that, we have added the same amount (200  $\mu$  L for each case) of Au core NBPs in the growth process of Au@Ag NRs for every length, afterwards we have centrifuged to collect them. After observing the TEM images of the Au@Ag NRs, we could assume that the numbers of collected Au@Ag NRs after centrifugation

were the same in every case as there were no Au NBPs left after this process. Finally, we had redispersed them in different volumes of deionized water so that the total number of Ag atoms remains same in every case. As a result, when we have acquired the SERS spectra, the effective surface area of the NRs and the number of analyte molecules remain constant. In this way, the analyte molecules formed a monolayer on the surface of the NRs in every case. Using this method, we have made the number of Ag atoms or Ag surface area same in our SERS measurement by maintaining different concentrations of NRs according to their lengths. In the Table 4.2, we have calculated and summarized the number densities of the Au@Ag NRs of each length along with the Ag NRs. From the Table 4.2, we can clearly observe that as the lengths of the NRs have increased, the number densities of the NRs have decreased, which is quite obvious. The calculated density of NRs in the SERS substrate was used to calculate the SERS EFs offered by different analytes separately.

#### 4.3.2.1 For 4-MBA

For 4-MBA as analyte, we have calculated the EF at the maximum SERS signals observed at  $1070\text{ cm}^{-1}$  and  $1592\text{ cm}^{-1}$  respectively. The density and molecular weight of 4-MBA are  $\rho = 1.49\text{ g.cm}^{-3}$  and  $M = 154.13\text{ g.mol}^{-1}$ , respectively.

Hence, from the equation 4.8, we can find out

$$N_{bulk} = 1.64 \times 10^{13} \quad (4.9)$$

Assuming the NRs to be spherically ended rods, the surface area  $S$  of an NR of length  $l$  and radius  $r_{NR}$  is given by  $S = 4\pi r_{NR}^2 + 2\pi r_{NR}(l - 2r_{NR})$ .

The packing density of 4-MBA molecules on Ag surface is  $\sigma \sim 3.01 \times 10^5\text{ }\mu\text{m}^{-2}$  [434].

When the SERS substrate was exposed to the laser excitation, only the upper half of the NRs interacted with the laser excitation. Considering this fact, we get

$$N_{SERS} = \frac{S\sigma V n_{NR}}{2} \quad (4.10)$$

where, the effective laser excitation volume  $V = 2.81 \times 10^{-15} \text{ m}^3$  we have got from equation 4.7 and  $n_{NR}$  is the number density of NRs in the SERS substrate we have calculated in the Table 4.2.

$I_{bulk}$  and  $I_{SERS}$  can be found from the area under the certain Raman peaks of the SERS spectra. From the SERS spectra for 4-MBA as analyte in Figure 4.5, we have obtained  $I_{bulk} = 6402.6$  counts for Raman mode at  $1076 \text{ cm}^{-1}$  and  $I_{bulk} = 1865.6$  counts for Raman mode at  $1592 \text{ cm}^{-1}$ . The calculated EF for Au@Ag NRs of different lengths and Ag NRs for 4-MBA as analyte are presented in the Table 4.3.

From the Table 4.3, we can notice that the obtained EF at  $1592 \text{ cm}^{-1}$  for

Table 4.3: SERS EF for Ag NR and Au@Ag NR of different lengths for 4-MBA as analyte.

Samples		$N_{SERS}$	$I_{SERS}$ @ $1076 \text{ cm}^{-1}$	$I_{SERS}$ @ $1592 \text{ cm}^{-1}$	EF @ $1076$ $\text{cm}^{-1}$	EF @ $1592$ $\text{cm}^{-1}$
Au@Ag NRs of length	230 nm	482414.03	113325.62	330236.06	$6.01 \times 10^8$	$6.01 \times 10^9$
	450 nm	499086.09	384810.41	$1.06 \times 10^6$	$1.97 \times 10^9$	$1.86 \times 10^{10}$
	700 nm	475927.14	316610.38	870251.46	$1.70 \times 10^9$	$1.60 \times 10^{10}$
	800 nm	452130.78	271282.38	786400.63	$1.53 \times 10^9$	$1.53 \times 10^{10}$
	1000 nm	438214.16	217003.35	650976.66	$1.27 \times 10^9$	$1.30 \times 10^{10}$
	1200 nm	425545.79	159992.77	469408.50	$9.61 \times 10^8$	$9.68 \times 10^9$
Ag NRs of 450 nm		496934.86	76097.82	277993.97	$3.92 \times 10^8$	$4.91 \times 10^9$

Au@Ag NRs of length 450 nm is  $1.86 \times 10^{10}$ , which is maximum among Au@Ag NRs of all other lengths and comparable to the previously reported result in the literature [435]. We could also observe that the EF for monometallic Ag NRs of length 450 nm is  $4.91 \times 10^9$ , which is almost  $1/4^{th}$  of the EF obtained for core-shell Au@Ag NRs of same length i.e., 450 nm.

#### 4.3.2.2 For CrV

For CrV as analyte, the EFs were calculated at the maximum Raman signals observed at 1172, 1385 and 1615  $cm^{-1}$ , respectively. The density and molecular weight of CrV are  $\rho = 1.19 g.cm^{-3}$  and  $M = 407.98 g.mol^{-1}$ , respectively.

Therefore, from the equation 4.8, we have got  $N_{bulk} = 4.94 \times 10^{12}$ .

The molecular foot print size of a CrV molecule on Ag surface is  $a = 4 nm^2$  [436].

Table 4.4: SERS EF for Au@Ag NR of different lengths for CrV as analyte.

Samples	$N_{SERS}$	$I_{SERS}$ @ 1172 $cm^{-1}$	$I_{SERS}$ @ 1385 $cm^{-1}$	$I_{SERS}$ @ 1615 $cm^{-1}$	EF @ 1172 $cm^{-1}$	EF @ 1385 $cm^{-1}$	EF @ 1615 $cm^{-1}$	
Au@Ag NRs of length	230 nm	400676.11	$1.39 \times 10^6$	$2.28 \times 10^6$	$1.96 \times 10^6$	$1.60 \times 10^8$	$1.59 \times 10^8$	$1.72 \times 10^8$
	450 nm	414523.33	$6.02 \times 10^6$	$9.25 \times 10^6$	$8.48 \times 10^6$	$6.70 \times 10^8$	$6.23 \times 10^8$	$7.20 \times 10^8$
	700 nm	395288.32	$4.40 \times 10^6$	$6.75 \times 10^6$	$6.25 \times 10^6$	$5.14 \times 10^8$	$4.77 \times 10^8$	$5.57 \times 10^8$
	800 nm	375523.90	$2.20 \times 10^6$	$3.58 \times 10^6$	$3.38 \times 10^6$	$2.70 \times 10^8$	$2.66 \times 10^8$	$3.17 \times 10^8$
	1000 nm	363965.25	$2.11 \times 10^6$	$3.38 \times 10^6$	$3.27 \times 10^6$	$2.67 \times 10^8$	$2.59 \times 10^8$	$3.16 \times 10^8$
	1200 nm	353443.35	$1.93 \times 10^6$	$3.04 \times 10^6$	$2.88 \times 10^6$	$2.52 \times 10^8$	$2.40 \times 10^8$	$2.87 \times 10^8$

Therefore, the packing density could be found  $\sigma = \frac{1}{a} = 2.50 \times 10^5 \mu m^{-2}$ . From this information, we could find out the value of  $N_{SERS}$  using the equation 4.10.

From the SERS spectra of Au@Ag NRs for CrV as analyte presented in the Figure 4.6, we have found out the values of  $I_{bulk}$  to be 107078.7, 176861.1 and 140305.6 counts at 1172, 1385 and 1615  $cm^{-1}$ , respectively. The calculated EFs for the Au@Ag NRs of different lengths are summarized in the Table 4.4.

From the values obtained in the Table 4.4, the maximum SERS EF was obtained for Au@Ag NRs of length 450 nm at 1615  $cm^{-1}$  which is  $7.20 \times 10^8$ .

#### 4.3.2.3 For 4-MPy

We have also calculated the EFs for Au@Ag NRs of different lengths using 4-MPy as analyte at the maximum Raman signals observed at 993 and 1100  $cm^{-1}$ , respectively. For 4-MPy, the density and molecular weight are  $\rho = 1.20 g.cm^{-3}$  and  $M = 111.16 g.mol^{-1}$ , respectively.

So, from the equation 4.8, we have got  $N_{bulk} = 1.83 \times 10^{13}$ .

The molecular foot print size of a 4-MPy molecule on Ag surface  $a = 0.18 nm^2$  [437].

Table 4.5: SERS EF for Au@Ag NR of different lengths for 4-MPy as analyte.

Samples		$N_{SERS}$	$I_{SERS}$ @ 993 $cm^{-1}$	$I_{SERS}$ @ 1100 $cm^{-1}$	EF @ 993 $cm^{-1}$	EF @ 1100 $cm^{-1}$
Au@Ag NRs of length	230 nm	8911036.66	128935.3	89917.03	$2.02 \times 10^7$	$3.51 \times 10^7$
	450 nm	9218998.90	813974.2	796227.2	$1.23 \times 10^8$	$3.01 \times 10^8$
	700 nm	8791212.24	234140.3	196930.6	$3.72 \times 10^7$	$7.80 \times 10^7$
	800 nm	8351651.62	218020.1	182285.0	$3.64 \times 10^7$	$7.60 \times 10^7$
	1000 nm	8094587.16	160157.5	157905.4	$2.76 \times 10^7$	$6.79 \times 10^7$
	1200 nm	7860580.00	87545.0	78070.2	$1.55 \times 10^7$	$3.46 \times 10^7$

Therefore, the packing density could be found  $\sigma = \frac{1}{a} = 5.56 \times 10^6 \mu\text{m}^{-2}$ . From this information, we could find out the value of  $N_{SERS}$  using the equation 4.10.

From the SERS spectra of Au@Ag NRs using 4-MPy as analyte presented in the Figure 4.7, we have found out the values of  $I_{bulk}$  to be 13110.2 and 5257.0 counts at 993 and 1100  $\text{cm}^{-1}$ , respectively. The calculated EFs for the Au@Ag NRs of different lengths are summarized in the Table 4.5.

From the values obtained in the Table 4.5, the maximum SERS EF was obtained for Au@Ag NRs of length 450 nm at 1100  $\text{cm}^{-1}$  which is  $3.01 \times 10^8$ .

### 4.3.3 Core-shell NSs, NCs, HNSs and HNCs

The strengths of the LSPRs in SERS activity for all the synthesized core-shell NPs with Au TOH NPs as core were studied by collecting the SERS spectra using 4-MBA as analyte. To prepare the SERS substrates, 10  $\mu\text{L}$  of the concentrated Au TOH NPs and all types of Au@Ag NPs were mixed with the 190  $\mu\text{L}$  of  $10^{-5}$  M 4-MBA solution separately. As the NPs contain a large number of sharp edges and tips, electromagnetic rays got focused at those places and hot spots were formed at those places. These hot spots contributed to high SERS enhancement. It is discussed before that if the LSPR bands of the NPs are close to the excitation wavelength of the laser, then high SERS signals are generated. Though the higher-order multipolar plasmon modes far away from laser excitation wavelength became nonradiative, they could also participate in the enhancement of the SERS activity by absorbing light and decaying through evanescent near-field [417].

The SERS spectra of Au TOH NPs and Au@Ag NS, NCs, HNSs and HNCs using 4-MBA as analyte are presented in the Figure 4.9. Comparing the spectra for different NPs, we can observe that all of them have very high and sharp peaks at 1076 and 1592  $\text{cm}^{-1}$  respectively. In our SERS experiment we had used 532 nm as

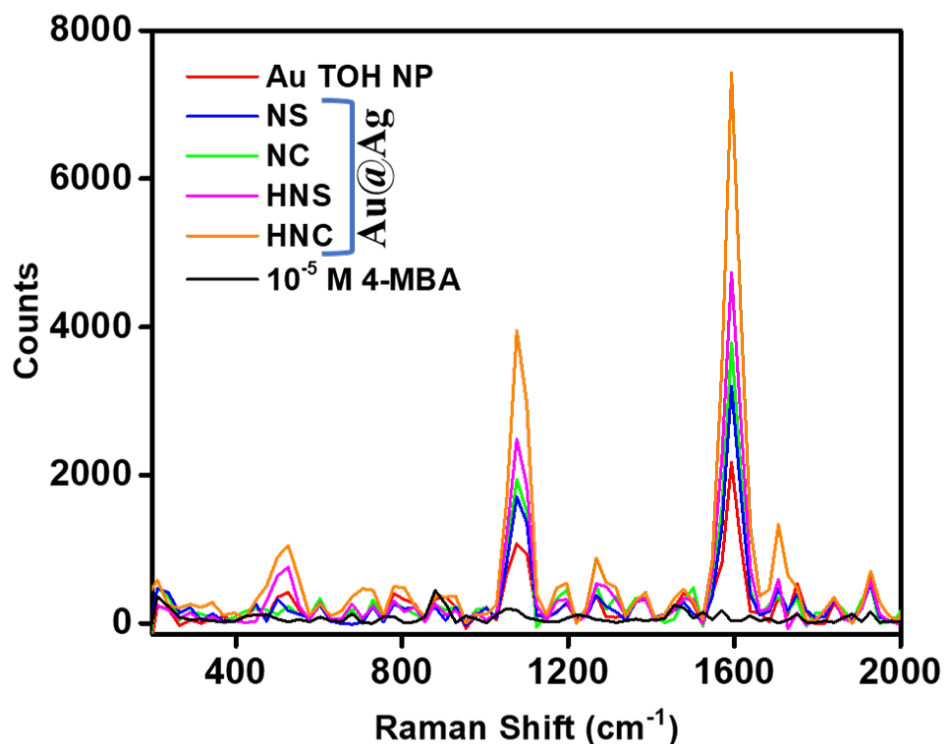


Figure 4.9: *SERS spectra of  $10^{-5}$  M 4-MBA mixed with the NPs of different morphology.*

our SERS excitation wavelength. From the absorption spectra of the Au TOH NPs presented in the Figure 4.4, we could observe that the dipolar LSPR band of Au TOH NPs is at 595 nm, which is very close to the excitation wavelength. Again, the TOH NPs contain large numbers of sharp edges and tips, which intensified the local electric field at those places. For that reason the SERS enhancement is very high for Au TOH NPs. Now, comparing the absorption spectra between Au TOH NPs and Au@Ag NSs and NCs, the dipolar LSPR bands for Ag of the Au@Ag NSs and NCs (427 nm and 439 nm respectively) were relatively far from the excitation wavelength of SERS. But, as the SERS enhancement offered by the Au@Ag core-shell NPs is much higher than Au NPs, hence Au@Ag NSs and NCs offered higher enhancement than Au TOH NPs though their dipolar LSPR bands were far away from the laser excitation wavelength. Comparing the morphology of Au@Ag NSs and NCs, the Au@Ag NCs contain several sharp edges and corners than NSs and the

local field got intensified at those places. For that reason the Au@Ag NCs offered better enhancement compared to the Au@Ag NSs. For the cases of Au@Ag HNSs and HNCs, their dipolar LSPR bands for Ag (559 nm and 623 nm respectively) were relatively closer to the SERS excitation wavelength and they contributed to high SERS enhancement. Again, as the Au@Ag HNSs and HNCs contain hollow Ag shells, the effective surface area is very high compared to the Au@Ag NSs and NCs as the shells are solid. Therefore, the analyte molecules only attached to the outer Ag surfaces for Au@Ag NSs and NCs. Whereas, for Au@Ag HNSs and HNCs, the analyte molecules could attach to both inner and outer Ag walls as well as on the core Au TOH NPs. Again, a higher number of hot spots would generate at the nanogaps between the Au TOH cores and hollow Ag shells. All these facts would increase the SERS signal. Hence, the SERS signals for the HNPs were higher compared to other NPs. Between the Au@Ag HNSs and HNCs, the SERS enhancement is maximum for Au@Ag HNCs, as they contain more number of sharp edge and corners compared to the Au@Ag HNSs.

The highest SERS signals are observed at 1076 and 1592  $cm^{-1}$  which could be assigned as *C-H in-plane bending* and *C=C symmetric stretching vibration* mode, respectively [426]. Hence, these two modes had maximum interaction with the plasmonic nanosurfaces. Besides these two strong peaks, some other Raman modes of lower intensity were observed at 526 and 1385  $cm^{-1}$  which could arise due to *C-H out-plane bending* and *COO<sup>-</sup> symmetric stretching*, respectively [426].

#### 4.3.4 Calculation of SERS EF for 4-MBA

The SERS EF has been calculated for the Au TOH NPs and the Au@Ag NPs of different morphologies using 4-MBA as analyte by the equation 4.5. Now, for 4-MBA as analyte, the value of  $N_{bulk}$  from the previously calculated result in the equation 4.9 is given by  $N_{bulk} = 1.64 \times 10^{13}$ .

To synthesize the Au TOH NPs,  $v = 2 \text{ mL} = 2 \times 10^{-3} \text{ L}$  of  $c = 10^{-2} \text{ M HAuCl}_4$  has been added to the growth solution. The atomic mass of Au is  $M_{Au} = 196.9666 \text{ u}$ . By assuming all the Au atoms have participated in the synthesis of the TOH NPs, we can find the total weight of the synthesized TOH NPs as  $W_{Au} = M_{Au}cv = 3.94 \times 10^{-3} \text{ g}$ .

Considering the size of the synthesized Au TOH NP is same, the volume of a single Au TOH NP with edge length  $l = 35 \text{ nm}$  would be  $v_{TOH} \cong \left( \frac{\sqrt{39+2\sqrt{2}}}{6} l^3 \right) = 6.48 \times 10^{-5} \mu\text{m}^3$ .

The density of solid Au is  $\rho_{Au} = 19.32 \text{ g.cm}^{-3} = 1.932 \times 10^{-11} \text{ g.}\mu\text{m}^{-3}$ . So, the weight of a single Au TOH NP is  $w_{TOH} = v_{TOH}\rho_{Au} = 1.25 \times 10^{-15} \text{ g}$ .

Therefore, the total number of TOH NPs after centrifugation in a final volume of  $V_S \cong 1 \text{ mL} = 10^{12} \mu\text{m}^3$  is given by  $N_{TOH} = \frac{W_{Au}}{w_{TOH}} = 3.15 \times 10^{12}$ .

Hence, the number density of the Au TOH NPs is  $n = \frac{N_{TOH}}{V_S} = 3.15 \mu\text{m}^{-3}$ .

For the synthesis of the Au@Ag NSs and NCs,  $250 \mu\text{L}$  of Au TOH NPs as seed solutions had been mixed to the growth solutions. As we could not observe any Au TOH NP during the TEM observation of the Au@Ag NSs and NCs, we could consider that all of the Au TOH NPs had been transformed into core-shell NPs. Hence, the number density of the Au@Ag NSs and NCs after centrifugation to the final volume of  $V_S \cong 1 \text{ mL}$  is  $1/4^{th}$  of the number density for Au TOH NPs.

Again,  $100 \mu\text{L}$  of the Au@Ag NSs and NCs had been mixed to the growth solutions for synthesizing Au@Ag HNSs and HNCs. As we could not observe any Au@Ag NPs with solid Ag core, we could consider that all of the Au@Ag NSs and NCs had been transformed to Au@Ag HNSs and HNCs, respectively. Therefore, the number density of the Au@Ag HNSs and HNCs after centrifugation to a final volume  $V_S \cong 1 \text{ mL}$  is  $1/10^{th}$  of the number density for Au@Ag NSs or NCs, i.e.,  $1/40^{th}$  of number density for Au TOH NPs.

To prepare the SERS substrates, 10  $\mu\text{L}$  of the synthesized NP solutions have been mixed with 190  $\mu\text{L}$  of  $10^{-5}$  M 4-MBA solutions. So, the number density of the NPs in SERS substrates is  $1/20^{\text{th}}$  of the number density in each case we have calculated above. For example, the number density of Au TOH NPs in SERS substrate is  $n_{TOH} = \frac{n}{20} = 1.575 \times 10^{-1} \mu\text{m}^{-3}$ .

After calculating the number density of each type of Au@Ag NPs, we have calculated the values of  $N_{SERS}$  from equation 4.10 for each of them. The values of  $I_{bulk}$  and  $I_{SERS}$  could be obtained from the area under the peaks from the SERS spectra presented in the Figure 4.9. The obtained values of  $I_{bulk}$  at 1076 and 1592  $\text{cm}^{-1}$  are 8876.5 counts and 4520.7 counts, respectively. The calculated values of the EFs for Au TOH NPs and Au@Ag NSs, NCs, HNSs and HNCs have been summarized in the Table 4.6. The maximum value of the EF has been obtained for Au@Ag HNCs at the Raman mode 1592  $\text{cm}^{-1}$  and the value is  $7.52 \times 10^9$ .

Table 4.6: SERS EF for Au TOH NPs and Au@Ag NPs of different morphologies for 4-MBA as analyte.

Samples	Surface area ( $S$ ) in $\text{nm}^2$	$N_{SERS}$	$I_{SERS}$ @ 1076 $\text{cm}^{-1}$	$I_{SERS}$ @ 1592 $\text{cm}^{-1}$	EF @ 1076 $\text{cm}^{-1}$	EF @ 1592 $\text{cm}^{-1}$	
Au TOH NP	12730.6	$8.48 \times 10^5$	53012.8	81197.8	$1.16 \times 10^7$	$3.47 \times 10^7$	
Au@Ag	NS	80424.8	$1.34 \times 10^6$	77665.7	124151.0	$1.07 \times 10^8$	$3.36 \times 10^8$
	NC	86400.0	$1.44 \times 10^6$	87992.1	146861.9	$1.13 \times 10^8$	$3.70 \times 10^8$
	HNS	80424.8	$1.34 \times 10^5$	111214.6	191907.6	$1.54 \times 10^9$	$5.20 \times 10^9$
	HNC	86400.0	$1.44 \times 10^5$	173731.1	298884.8	$2.23 \times 10^9$	$7.52 \times 10^9$

## 4.4 FDTD simulation

Using FDTD simulation, one can solve many electromagnetic problems like scattering from any metallic or dielectric substance, antenna, micro-strip circuit, absorption of electromagnetic rays in the human body when exposed to radiation, etc. For anisotropic and arbitrarily shaped NPs like the various core-shell NPs we had synthesized here, it is very hard to find the analytical solution of Maxwell's equations because the electromagnetic field is very complex around the NPs. So the electromagnetic field near the arbitrarily shaped NPs can be easily found by FDTD simulation. The electric field is enhanced at the sharp edges and tips of the NPs, which can be clearly observed from the FDTD simulation. From the values of the electric fields at various places, we could find the SERS EF by the equation

$$EF = \left( \frac{E}{E_0} \right)^4 \quad (4.11)$$

where  $E_0$  is the amplitude of the electric field of the source and  $E$  is the local maximum electric field [438]. We have used 532 nm as the excitation wavelength in the FDTD simulation, same as for the SERS experiment.

### 4.4.1 Core-shell NRs

To visualize the local electric field and substantiate the experimentally calculated high SERS enhancement for Au@Ag NRs of different lengths, FDTD simulation were performed for both Au@Ag NRs and Ag NRs. The shell Ag NR was assumed as a spherically ended rod and in the middle of the rod we had placed a truncated bipyramidal structure on a pentagonal base of Au. For Au and Ag NR, they were similarly modeled as a spherically ended rod of Au and Ag respectively, without any core. In the Figure 4.10(a-c), we have presented the y-z views of the

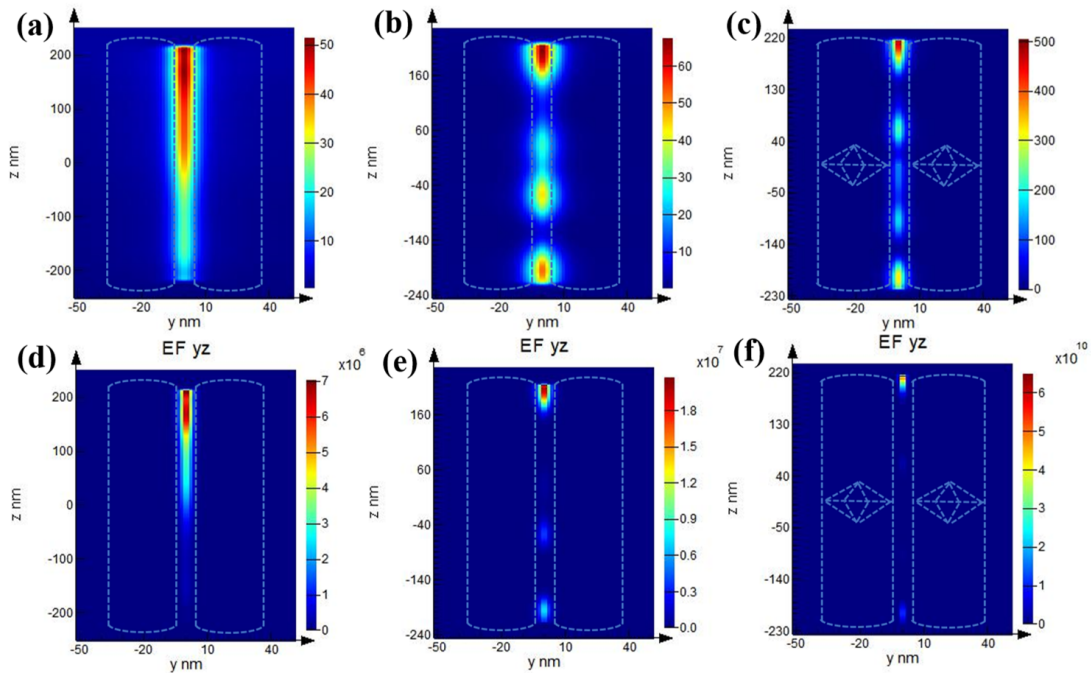


Figure 4.10:  $y$ - $z$  views of the electric-field distribution of (a) Au NRs, (b) Ag NRs, (c) Au@Ag NRs of length 450 nm and the corresponding EF maps for (d) Au NRs, (e) Ag NRs, (f) Au@Ag NRs of length 450 nm.

local electric field distribution for Au NRs, Ag NRs and Au@Ag NRs of length 450 nm, respectively. In the Figure 4.10(d-e), we have presented the corresponding EF maps of them. The local electric field distributions for Au NRs and Ag NRs show that for Ag NRs, the electric field and the corresponding EF is high compared to the Au NRs, which is very obvious. But, it is highest for Au@Ag NRs. From the Figure 4.10(a) and (b), we can clearly observe that the enhancement of the local electric field takes place only at the corners of the monometallic NRs. Whereas from the Figure 4.10(c), it is clear that besides the corners, large electric-field enhancement occurs in the middle of the Au@Ag NRs i.e., around the core Au NBPs. Due to the presence of sharp edges and tips in the core Au NBPs and coupling of the LSPR band of Au and Ag, the electric field is enhanced at the middle of the NRs.

In the Figure 4.11(a-e), we have presented the  $y$ - $z$  views of the local electric field distribution for Au@Ag NRs of lengths 230, 700, 800, 1000 and 1200 nm respectively.

The corresponding EF maps of them have been presented in the Figure 4.11(f-j). The results clearly demonstrate that as the length of the Au@Ag NRs increases, the value of EF decreases. And the maximum value of EF has been obtained for Au@Ag NRs of length 450 nm. All these observations justify the observation we have got from the SERS experiment.

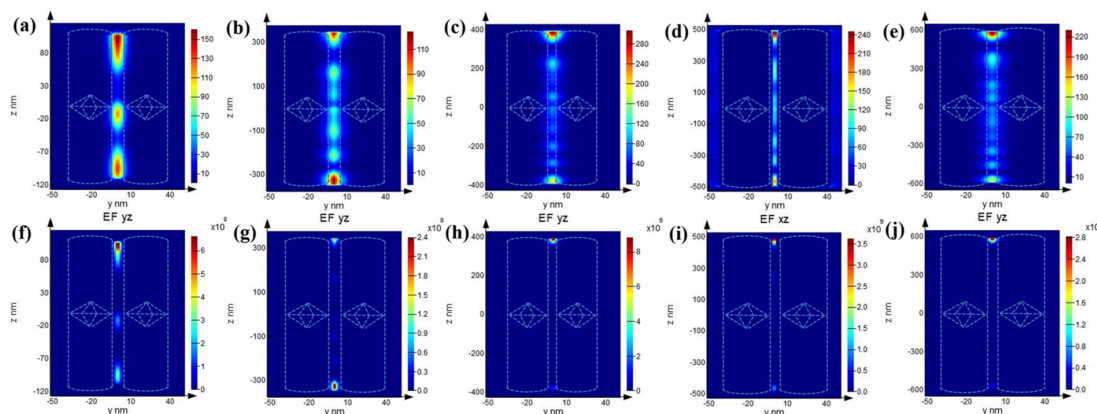


Figure 4.11: *y-z* views of the electric-field distribution of Au@Ag NRs of length (a) 230 nm, (b) 700 nm, (c) 800 nm, (d) 1000 nm, (e) 1200 nm and the corresponding EF maps for Au@Ag NRs of length (f) 230 nm, (g) 700 nm, (h) 800 nm, (i) 1000 nm, (j) 1200 nm, respectively.

The EF we have obtained from the SERS experiment is very high compared to some previously reported Au@Ag NRs with Au NRs as core [439, 440]. To justify this observation, we have performed the FDTD simulation of those previously reported structures. In the Figure 4.12(a) and (b), we have presented the *y-z* view of the local electric field distribution and in the Figure 4.12(c) and (d) the corresponding EF for Au@Ag NRs of lengths 80 and 230 nm respectively, with a 75 nm long Au NR core in both cases. Comparing the EF of these two types of NRs with our synthesized Au@Ag NRs, we can clearly observe that the SERS EF is very high for Au@Ag NRs with Au NBP as core because the Au NR core inside the Au@Ag NR does not have any sharp edges or tips. Whereas the Au NBP core inside the Au@Ag NR we have synthesized, contains several sharp edges and tips, where the electromagnetic rays got focused, which resulted in high SERS enhancement.

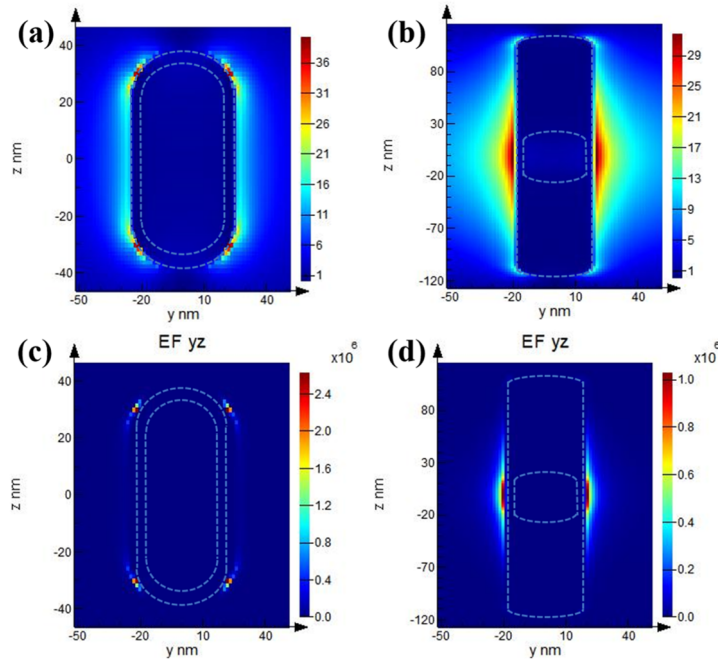


Figure 4.12: *y-z* views of the electric-field distribution of Au@Ag NR of length (a) 80 nm, (b) 230 nm and the corresponding EF maps for Au@Ag NR of length (c) 80 nm, (d) 230 nm with core Au NR of length 75 nm.

#### 4.4.2 Core-shell NSs, NCs, HNSs and HNCs

FDTD simulations were performed to study the local electric field near the NPs and to verify the experimentally observed SERS enhancement for Au TOH NPs, Au@Ag NSs, NCs, HNSs and HNCs. The electric field was intensified at the sharp edges and corners of the NPs as well as at the nanogaps between two NPs. In Figure 4.13(a), we have presented the distribution of the local electric field for two Au TOH NPs of edge length 35 nm and separated by a distance of 5 nm. The map clearly shows that the electric field has amplified at the tips of the Au TOH NPs and at the nanogaps between the TOH NPs. In the Figure 4.13(b), we have presented the EF map for the Au TOH NPs. The EF was found to be ( $\sim 10^7$ ), which is very close to the value we had found from the SERS measurement and subsequent EF calculation.

The *y-z* views of electric field distribution for core-shell Au@Ag NSs, NCs,

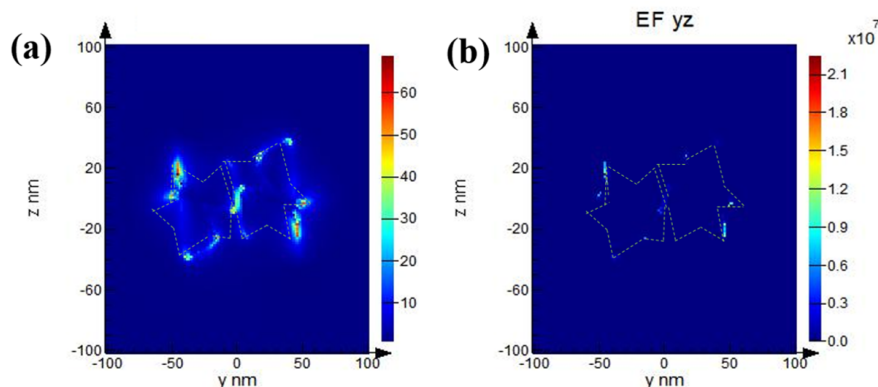


Figure 4.13: *y-z* view of (a) the electric field distribution and (b) corresponding EF map for Au TOH NPs.

HNSs and HNCs placed 5 nm apart are presented in the Figure 4.14(a)-(d) respectively. The corresponding EF maps are shown in the Figure 4.14(e)-(h) respectively. From the Figure 4.14(e), we could observe that for Au@Ag NSs, the maximum contribution in SERS is coming from the nanogap between the two NSs. But for Au@Ag NCs, the maximum contribution is coming from the corners of the Ag shell and it is much larger than the case for Au@Ag NSs. Similar results have been observed for Au@Ag HNSs and HNCs, but the values of the electric field and correspond EF are much larger than Au@Ag NSs and NCs. For Au@Ag HNSs and HNCs, as the shells were hollow, the electromagnetic rays could penetrate the hollow shells and interact with the Au TOH cores, which was not for the cases of Au@Ag NSs and NCs as the incoming electromagnetic wave could not penetrate the solid Ag shell. So, for Au@Ag HNSs and HNCs, both core and shell participated in the enhancement of the electric field, resulting in high enhancement. From the FDTD simulation results, the maximum SERS EF was obtained for Au@Ag HNCs which is ( $\sim 5 \times 10^9$ ), which is close to the value we had obtained from the SERS experiment.

From the observations, it was noticed that the experimentally obtained values of the SERS EF did not match completely with the values obtained from the FDTD simulation. The possible reasons behind this might be:

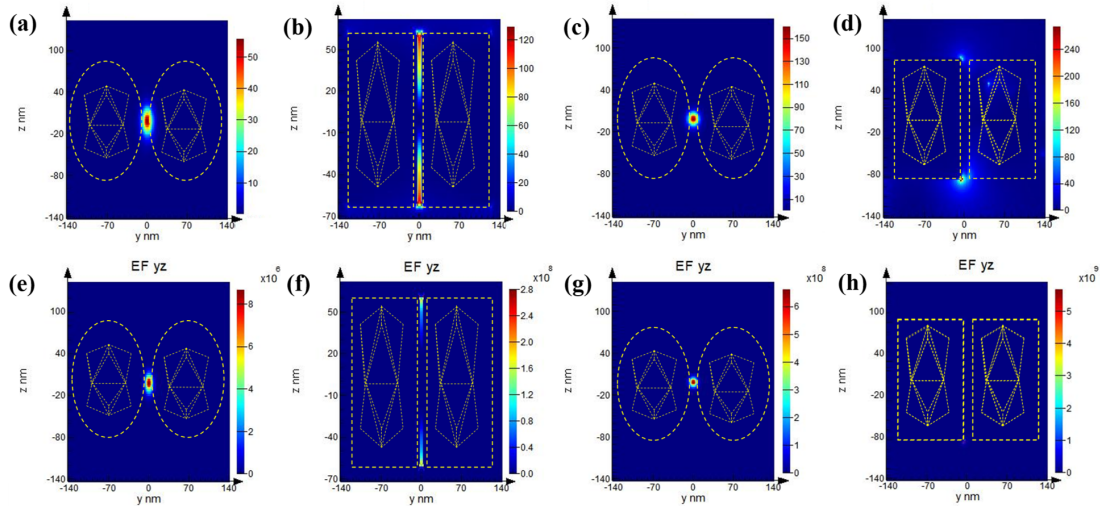


Figure 4.14:  $y$ - $z$  views of the electric field distribution for Au@Ag (a) NSs, (b) NCs, (c) HNSs, (d) HNCs and corresponding EF maps for Au@Ag (e) NSs, (f) NCs, (g) HNSs, (h) HNCs, respectively.

- In FDTD simulation, we had modeled the NPs with a specific dimension only. But in reality, there exists a size distribution for all the NPs which was neglected during FDTD simulation.
- Similarly, from TEM observation we have fixed a 5 nm of separation between two NPs during the FDTD simulation, but the separation also was not fixed in the SERS substrate.
- Moreover SERS is a combined effect of electromagnetic enhancement and chemical enhancement. But for FDTD simulation, the contribution from the chemical part was neglected.

#### 4.4.3 Pd NCs and Au@Pd NCs

Pd NPs are very important in the field of nanotechnology for their highly catalytic properties. They are being widely used in various industrial fields such as hydrogen storage [441], electrode material in electro-catalysis [442], reduction of pollutant gases [443], etc. But, of Pd NPs remained largely unexplored compared to

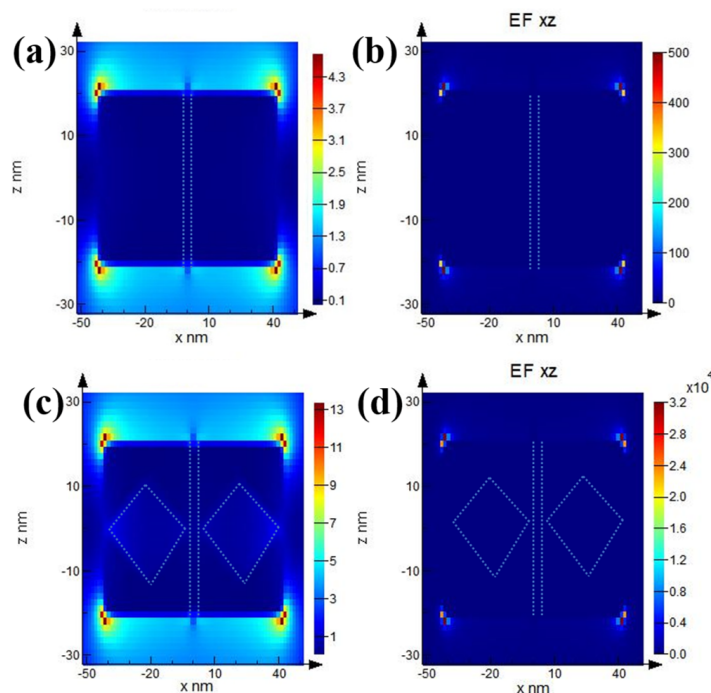


Figure 4.15: (a) *x-z* view of electric field distribution and (b) EF map of Pd NCs, (c) *x-z* view of electric field distribution and (d) EF map of Au@Pd NCs.

Au and Ag NPs because Pd NPs do not have any SPR band in the visible spectral region [444]. Besides, the SERS activity of Pd NPs is also very low compared to Au and Ag NPs. The incorporation of Au cores inside the Pd NPs could enhance the SERS activity of the NPs. In the Figure 4.15(a) and (b), the *x-z* view of the local electric field distribution of the Pd NCs situated at a distance of 5 nm and the corresponding EF distribution are presented. The local electric field distribution map (Figure 4.15(a)) shows the electric field got focused at the sharp corners of the Pd NCs. The EF distribution map shows the highest EF of almost  $5 \times 10^2$  which matches with the reported experimental SERS EF values ( $10\text{--}10^3$ ) [445]. The *x-z* view of the local electric field distribution of the Au@Pd NPs situated at a distance of 5 nm and the corresponding EF distributions are presented in the Figure 4.15(c) and (d). The result confirms that due to the insertion of the Au octahedral core, the local electric fields and the corresponding EF have increased several times (highest EF  $\sim 3 \times 10^4$ ). Due to the insertion of the Au octahedral core, the numbers of sharp

edges and tips have increased in the NPs, which increased the EF. Again, due to the lattice mismatch between Au and Pd ( $\sim 4.69\%$ ), a lattice strain has developed in the Au@Pd NCs, which has also contributed to increasing the EF. Hence, the SERS EF can be easily increased for Pd NPs by incorporation of Au cores inside them.

## 4.5 Conclusion

In this chapter we have discussed about the absorption spectra acquired from Au@Ag NPs of different morphologies and high SERS enhancement. The Au@Ag NRs of different lengths showed multipolar plasmon peaks throughout the region of the absorption spectra. Besides the plasmon peaks of Au and Ag, the coupled modes between Au and Ag also appeared in the absorption spectra. Due to the presence of dipolar plasmon peaks near the excitation wavelengths of the laser, the Au@Ag NRs provided huge SERS enhancement for different analytes like 4-MBA, CrV and 4-MPy. The SERS enhancement was compared with the monometallic Ag NRs. Due to the absence of plasmon peaks near the excitation wavelength as well as Au NBP cores, Ag NRs showed comparatively lower SERS enhancement. The local electric field near the Au@Ag NRs was studied using FDTD simulation, and it was found that the electric field is maximum near the core Au NBPs as they contain more number of sharp edges and tips compared to other regions. The SERS EF was verified using the FDTD analysis, and it is remarkable that the values have matched quite well with the experimental values. All these observations make the Au@Ag NRs a very good SERS substrate with high EF.

From the absorption spectra of Au@Ag NSs, NCs, HNSs and HNCs, we have clearly observed that for Au@Ag NPs with solid shells (e.g. NSs and NCs), the plasmon peaks for Ag dominated over other modes. Whereas, for Au@Ag NPs with hollow shells (e.g. HNSs and HNCs), the coupled modes between Au and

Ag dominated over other plasmon modes, because in these cases, the incoming electromagnetic waves could penetrate the thin Ag walls very easily and interact with the Au TOH cores. The SERS spectra showed maximum EF for Au@Ag HNCs, as the analyte molecules could be absorbed on both sides of the Ag shells as well as on core Au TOHs. Again, as the Au@Ag HNCs contain a large number of sharp edges and tips on both core Au TOHs and shell Ag NCs, the electromagnetic rays focused at those places, resulting in high SERS enhancement. These facts were verified by the FDTD simulation, and it was observed that the electric field was very high at the corners of the Ag shells and also inside the Ag shells, around the tips of the core Au TOH NPs.

## Chapter 5

# Cyclic voltammetry study and application of the nanoparticles as bio-sensors

---

---

*This chapter is an overview of the interfacial charge transfer of the nanoparticles as electrodes using cyclic voltammetric and amperometric studies and the application of the nanoparticles as bio-sensors for sensing uric acid and ascorbic acid.*

---

---

## 5.1 Introduction

Electrochemistry is the study about the transfer of electrons between the electrodes and reactant molecules. Voltammetry is a kind of electrochemical study, where we measure the current through the electrodes with respect to a time dependent potential applied across the electrodes. From voltammetry, we could get a lot of qualitative information about the system, like the redox potential of the analyte, diffusion coefficient of the analyte molecules in a particular medium, the total number of electrons transferred during the reaction, etc. [446]. There exist different kinds of voltammetry studies depending upon the kinds of wave forms applied across the electrodes. Cyclic voltammetry is one such kind of voltammetry where the applied potential across the working electrode is ramped linearly with time. After a time, the potential reached to a set value and then it is ramped in the opposite direction. Therefore, after some time, the potential reaches to its initial value completing a full cycle, which implies the applied waveform is triangular in nature. In the Figure 5.1(a), we have presented the waveform of the ramped potential applied across the electrodes in cyclic voltammetry, where  $E_{initial}$  is the initial potential of the electrode. After the 'forward scan' is complete, it reaches to the switching potential  $E_{switching}$  and the ramped is then applied in opposite direction. After the 'reverse scan' is complete, it reaches to its initial potential  $E_{initial}$ .

A cyclic voltammogram would be called reversible if the heterogeneous electron transfer occurs much faster than other processes like scan rate of ramp potential, diffusion, etc. In the Figure 5.1(b), we have shown a typical reversible cyclic voltammogram for an electrochemical system. From the plot in Figure 5.1(b), we could know both kinetic and thermodynamic information of the electrochemical system. If  $E_{pc}$  and  $E_{pa}$  be the potentials of the cathode peak and anode peak respectively,

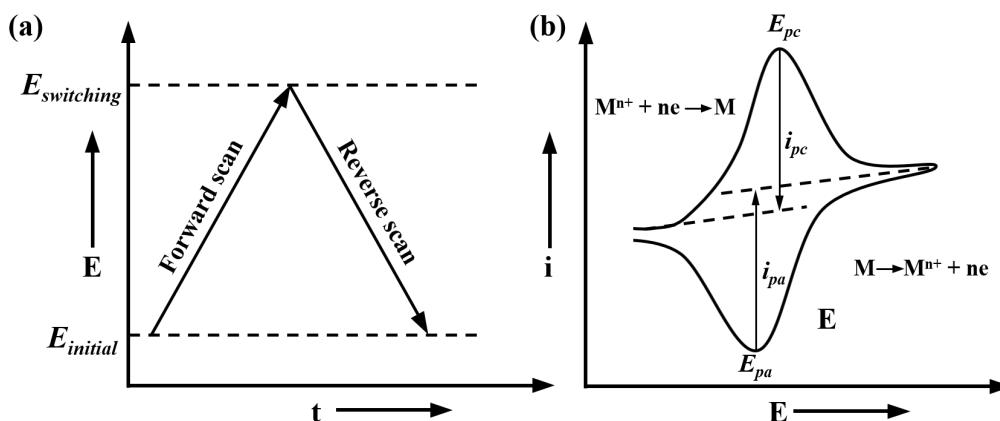


Figure 5.1: (a) Waveform of the ramped potential applied across the electrodes in cyclic voltammetry, (b) a typical cyclic voltammogram for a reversible electrochemical system.

then the separation between these two peaks  $\Delta E_p$  would be given by

$$\Delta E_p = |E_{pc} - E_{pa}| = 2.303 \frac{RT}{nF} \quad (5.1)$$

Here, the Faraday constant  $F = 96485.33212 \text{ C.mol}^{-1}$ , and  $n$  is the number of electrons getting transferred per molecule during reduction or oxidation. At  $25^\circ\text{C}$ , we get

$$\Delta E_p = \frac{0.059}{n} \text{ V} \quad (5.2)$$

The formal reduction potential  $E_{red}$  of a reversible couple is given by the equation

$$E_{red} = \frac{E_{pc} + E_{pa}}{2} \quad (5.3)$$

The peak current  $i_p$  in the voltammogram could be given by the Randles-Sevcik equation as [447]

$$i_p = 0.4463 n A F C \left( \frac{n v F D}{RT} \right)^{1/2} \quad (5.4)$$

where,  $n$  is the number of electrons getting transferred per molecule during reduction or oxidation,  $A$  is the area of the electrode,  $F$  is the Faraday Constant,  $C$  is the concentration of the redox solution,  $v$  is the potential sweep rate and  $D$  is the diffusion coefficient at temperature  $T$ . At  $25^\circ\text{C}$ , the equation 5.4 is reduced to

$$i_p = (2.69 \times 10^5) n^{3/2} AD^{3/2} Cv^{3/2} \quad (5.5)$$

From the equation 5.5, we could determine various quantities like the number of electrons getting transferred in a redox reaction, the diffusion coefficient, active surface area of an electrode, etc.

So, a cyclic voltammetric biosensor operates in cyclic modes with a ramped potential applied across the electrodes. Whereas, in amperometric biosensors, a fixed potential is applied across the electrodes, which is either reduction or oxidation potential of the redox molecules, and a corresponding current is obtained. Hence, a current is obtained only when the applied potential across the electrodes is equal to the reduction or oxidation potential of the redox molecules. In an amperometric biosensor, the current  $i$  will be given by the Cottrell equation as [448]

$$i = \frac{nFAc_0\sqrt{D}}{\sqrt{\pi t}} \quad (5.6)$$

where,  $n$  is the number of electrons getting transferred per molecule during reduction or oxidation,  $F$  is the Faraday Constant,  $A$  is the area of the electrode,  $D$  is the diffusion coefficient,  $c_0$  is the initial concentration of the redox solution and  $t$  is the time elapsed from when the potential was applied. Using the equation 5.6, we could find out the diffusion coefficient  $D$  of the redox molecules.

Uric acid (UA) is the last product of purine metabolism in the human body. Purine converts into UA. The human body maintains a specific level of UA. The excess UA is removed through urine. For a normal and healthy human being, the

usual concentration of UA in urine is 2 mM [449]. Any abnormal levels of UA can result in some type of diseases, such as hyperuricemia, gout and Lesch-Nyhan [450, 451]. Besides UA, AA also exists in human blood and urine in the form of vitamin C. AA or vitamin C acts as a very good antioxidant, as well as it helps the human body to synthesize collagen. Collagen is one of the main constituents of bones, cartilages, teeth and blood vessels in the human body [452]. It also protects from retina muscular degeneration and cancer [453, 454]. But we have to intake vitamin C by consumption of vegetables and citrus fruits as the human body is unable to produce vitamin C [455]. The concentration level of vitamin C in a normal human body varies between 120 – 450  $\mu\text{M}$  [456]. Any irregular levels of vitamin C in blood can cause various diseases like diarrhea, nausea, etc. [454]. For all of these reasons, accurate, susceptible and selective detection of both UA and AA or vitamin C is very significant for clinical diagnosis or industrial purposes [450, 451, 453, 454, 457]. But the simultaneous detection of both UA and AA is very hard using carbon or as-deposited diamond electrodes as both UA and AA oxidize them at nearly same potential. Whereas, using the cyclic voltammetric or amperometric technique, one can easily and selectively detect both UA and AA at the same time with great sensitivity. Besides, it is a very cost-effective method for sensing any biomolecule.

We had designed the electrodes by spin coating the Au@Ag NSs, NCs, HNSs, HNCs on ITO coated glass substrates. We had performed the cyclic voltammetric studies using these electrodes. We had also performed amperometric sensing studies of UA and AA with the electrodes. The observations are reported in this chapter.

## 5.2 Electrochemical cyclic voltammetry study

Five electrodes had been prepared by spin coating of Au TOH NPs and Au@Ag NSs, NCs, HNSs and HNCs respectively on ITO (indium tin oxide) coated glass

substrate. Cyclic voltammetry measurements had been performed to study the interfacial charge transfer and electron accumulation in between those electrodes and electrolyte interfaces. The cyclic voltammetry plots at a scan rate of 0.05 V/s for those electrodes are presented in the Figure 5.2. As the Au@Ag core-shell NPs contain Au-Ag interfaces, so a large amount of electron accumulation had taken place at those interfaces, which was not in the case for monometallic Au TOH NPs. Hence, the current densities for the core-shell nanostructures were much higher compared to the monometallic NPs, which is clearly visible from the Figure 5.2. It is evident that the effective surface area and interface area are much higher for the NPs with hollow Ag shells (HNSs and HNCs) compared to the NPs with solid Ag shells (NSs and NCs). As a result, the current density is higher for Au@Ag HNSs and HNCs. Again, between the NPs with cubical Ag shells (NCs or HNCs) and spherical Ag shells (NSs or HNSs), the NPs with cubical Ag shells have higher surface area compared to the NPs with spherical Ag shells of the same size. The

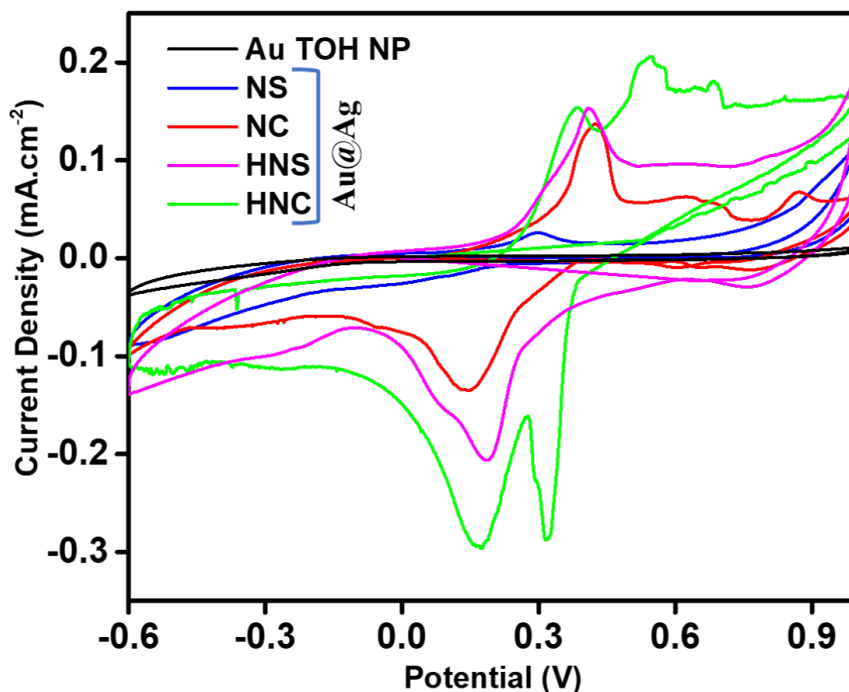


Figure 5.2: Cyclic voltammetry plots for Au TOH NPs and core-shell Au@Ag NSs, NCs, HNSs and HNCs, respectively at a scan rate of 0.05 V/s.

NPs with cubical Ag shells also contain multiple sharp edges and corners. As the charge density of any charged surface varies inversely to the radius of curvature, the charge density is higher for NCs and HNCs, because the sharp objects have a very small radius of curvature [458]. All of these facts support that the Au@Ag HNCs provide the maximum current density which was also observed in our cyclic voltammetry measurements.

### 5.3 Electrochemical sensing study

As the core-shell NPs provide very high current densities compared to the Au TOH NPs, so we had performed the non-enzymatic electrochemical sensing studies with the core-shell NPs only. In the sensing studies of both UA and AA, 0.1 M  $\text{Na}_2\text{SO}_4$  solution was used as the electrolyte. In the Figure 5.3(a-d), we have presented the cyclic voltammetry plots for different concentrations of UA added to the electrolyte medium, where we had used Au@Ag NSs, NCs, HNSs and HNCs as electrodes, respectively. From the plots, we can clearly observe that the current densities have increased significantly as the concentrations of UA have been increased at the potential of  $-0.36$  V, which is the reduction potential for UA. As UA was added into the medium, it got reduced at the reduction potential of  $-0.36$  V, which increased the effective number of ions into the electrolyte medium. The increased number of ions helped to increase the current density of the system and with higher molar concentrations of UA added to the medium, more number of ions were produced in the electrolyte solution, resulting in the increase in current densities. So, from the Figure 5.3(a-d), it is clear that these Au@Ag core-shell NPs could be used as UA sensors at an electrode potential of  $-0.36$  V. The plots also suggest that the change in current densities is maximum for Au@Ag HNCs, which indicates that it has the highest sensitivity for sensing UA over the other three core-shell NPs.

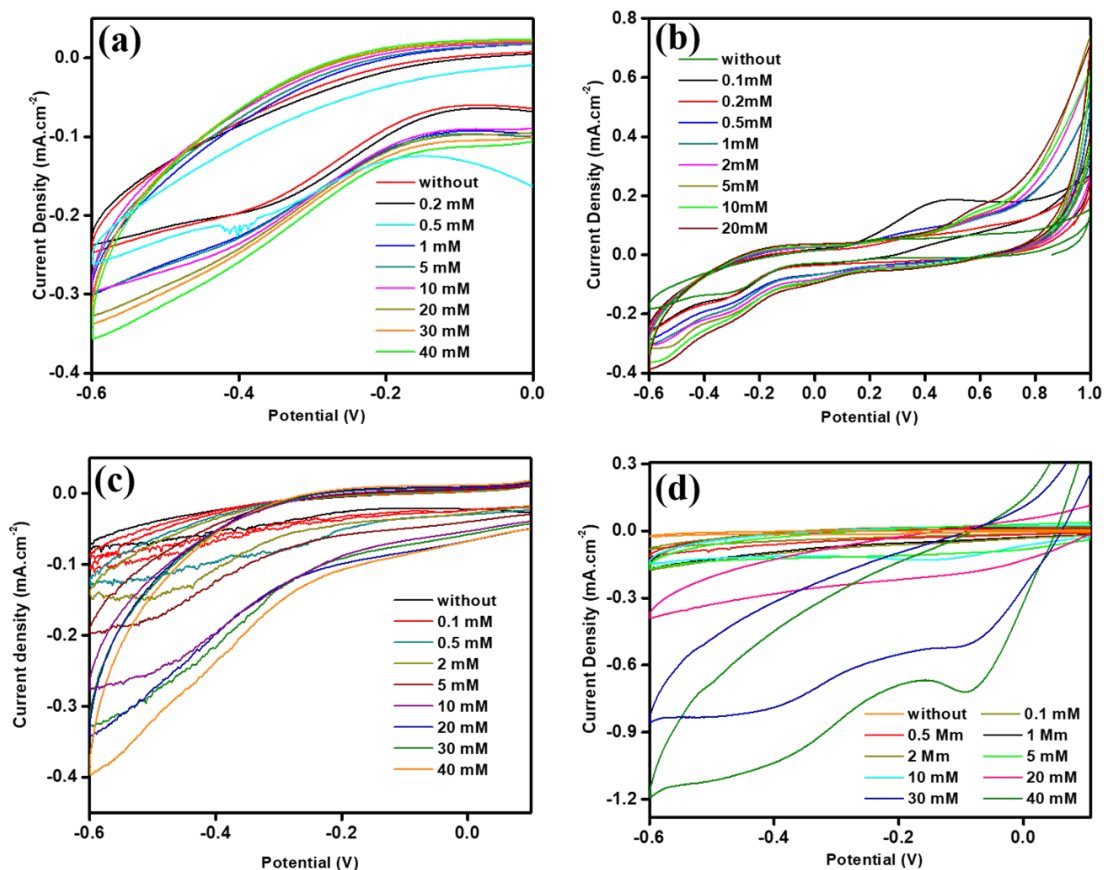


Figure 5.3: Cyclic voltammetry plots for different concentrations of UA added into the medium for Au@Ag (a) NSs, (b) NCs, (c) HNSs and (d) HNCs as electrode at a scan rate of 0.05 V/s.

Similarly, the AA sensing had been performed using these four types of core-shell NPs as electrode. The cyclic voltammetry plots for different concentrations of AA added into the electrolyte medium have been presented in the Figure 5.4(a-d), with Au@Ag NSs, NCs, HNSs and HNCs as electrodes respectively. Here we can observe that the current densities have been increased with increasing concentration of AA added in the electrolyte medium at the potential of 0.55 V, which is the oxidation potential for AA. As AA was added into the electrolyte medium, it got oxidized at the potential of 0.55 V, which increased the effective number of ions into the medium, resulting in the increase in current densities. So, we can conclude that these core-shell NPs as the electrode, can be used as AA sensor, with maximum sensing sensitivity for Au@Ag HNCs, as the change in current density is maximum

for it compared to the other three type of NPs.

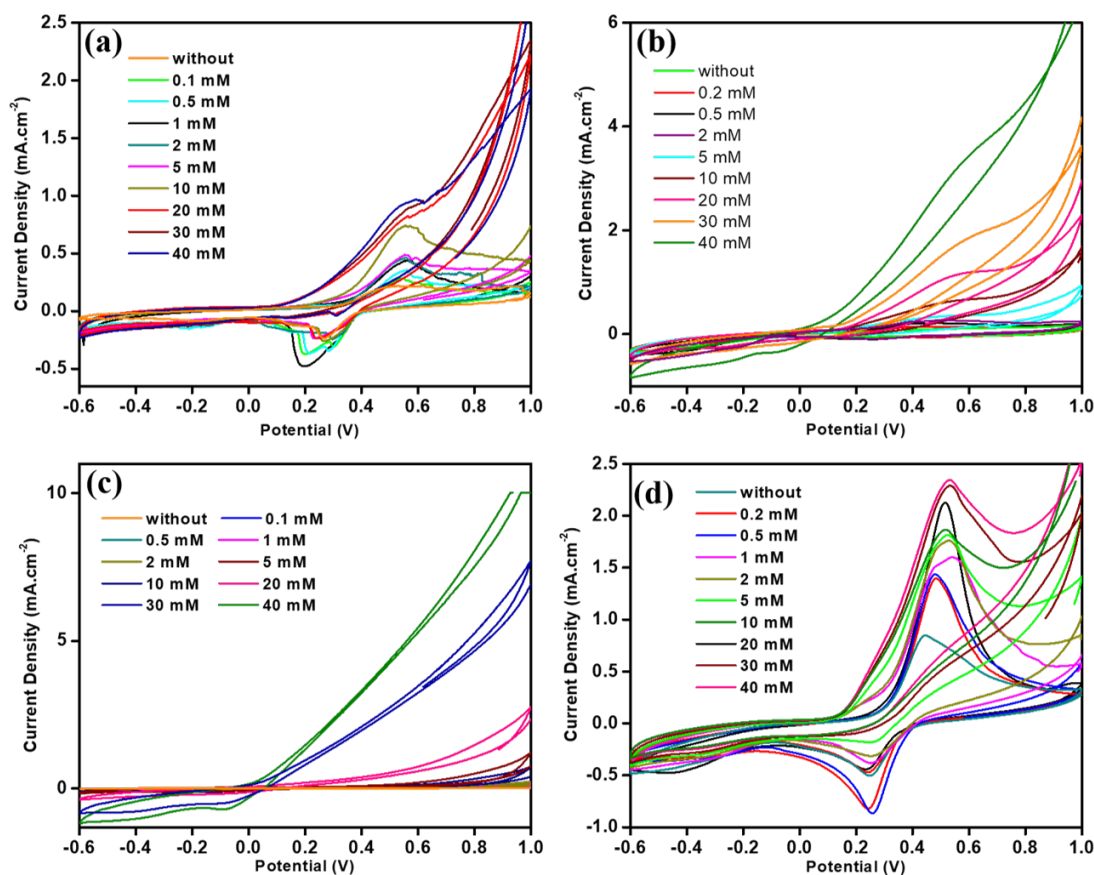


Figure 5.4: Cyclic voltammetry plots for different concentrations of AA added into the medium for Au@Ag (a) NSs, (b) NCs, (c) HNSs and (d) HNCs as electrode at a scan rate of 0.05 V/s.

The cyclic voltammetry plots in the Figure 5.3(a-d) and 5.4(a-b) for different concentrations of UA and AA added into the electrolyte medium recommend that Au@Ag NPs-coated ITO electrode could be used as an efficient sensor for detection of both UA and AA. It is clear that the change in current densities with increasing concentrations of UA or AA i.e., the sensitivity of sensing them, is maximum for Au@Ag HNCs for both the cases. As the Au@Ag HNCs have maximum surface area compared to the other three types of NPs, they have a larger area to interact with the electrolyte containing UA or AA. Again, Au@Ag HNCs contain multiple sharp edges and corners, where charge density is very high. All these facts make the sensitivity better for Au@Ag HNCs for sensing both UA and AA. We have performed the

amperometric sensing studies of UA and AA using only Au@Ag HNCs as electrode, because they have maximum sensitivity.

### 5.3.1 Amperometric sensing of UA

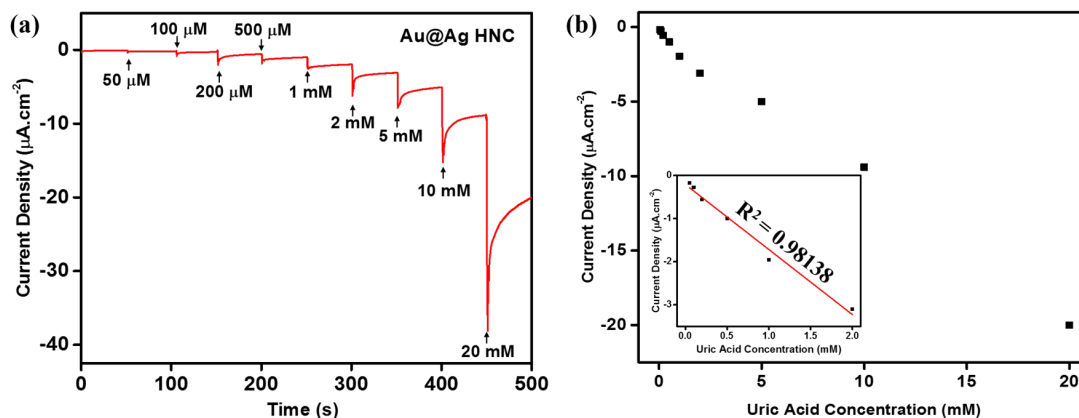


Figure 5.5: (a) Amperometric  $J-t$  curve and (b) corresponding response of current density for sensing UA with the linear fitted graph in the inset.

For amperometric sensing of UA with Au@Ag HNCs coated ITO as electrode, the electrode potential was kept fixed at  $-0.36$  V, which is the reduction potential of UA. Here, different concentrations of UA had been added into the electrolyte medium in increasing order after a regular time interval and changes in the current densities had been observed. In the Figure 5.5(a) we have presented the amperometric sensing study for UA. We could observe that with increasing concentrations of UA, the current density has been increased. In the Figure 5.5(b) we have presented the change in current density with the concentrations of UA which indicates that the current density has increased with increasing concentration of UA in almost linear order and become nonlinear at higher concentration region. At the linear region, i.e., at low concentrations of UA added into the medium which is from  $50 \mu\text{M}$  to  $2 \text{ mM}$ , the response curve has been linear fitted by the equation

$$J = -1.509 (\mu\text{A}\cdot\text{mM}^{-1}\text{cm}^{-2}) C_{\text{UA}} - 0.2090 \quad (5.7)$$

with a correlation factor of  $R^2 = 0.98138$  (presented at the inset of the Figure 5.5(b)). Hence, the sensitivity for sensing UA, which is implied by the slope of the graph, is  $1.509 \mu A.mM^{-1}cm^{-2}$  with the minimum detection limit of  $0.36 \mu M$  ( $S/N = 3$ ).

### 5.3.2 Amperometric sensing of AA

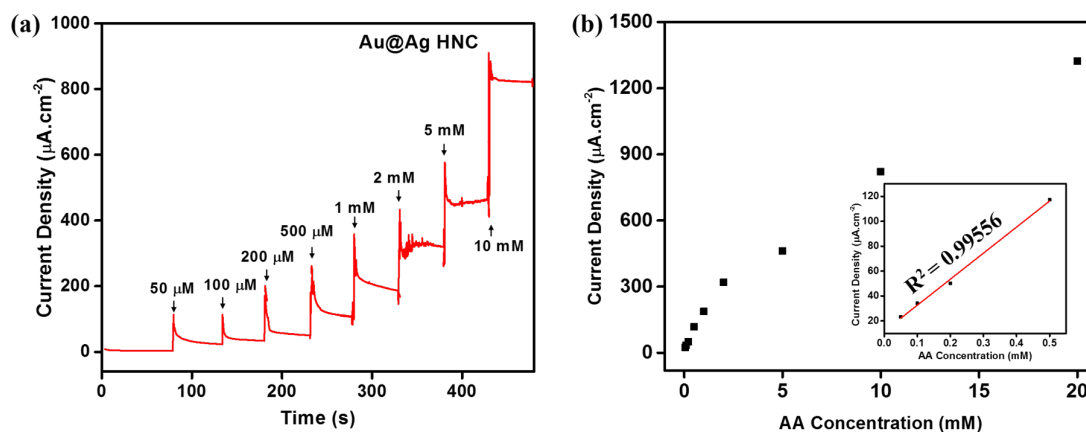


Figure 5.6: (a) Amperometric  $J-t$  curve and (b) corresponding response of current density for sensing AA with the linear fitted graph in the inset.

The amperometric sensing study of AA using Au@Ag HNCs coated ITO electrode was performed at the electrode potential 0.55 V, i.e., at the oxidation potential of AA. Figure 5.6(a) represents the amperometric sensing response curve, which shows that the current density has increased with increasing concentrations of AA added into the electrolyte medium after a successive time interval. In the Figure 5.6(b), we have plotted the current density for different concentrations of AA, which shows that the current density has been increased with increasing concentrations of AA almost linearly at the lower concentration region of AA, which is from 50  $\mu M$  to 500  $\mu M$ . And the current density becomes nonlinear at higher concentrations of AA. The linear part of the response curve in the Figure 5.6(b) has been linear fitted by the equation

$$J = 209.02718 (\mu A.mM^{-1}cm^{-2}) C_{AA} + 11.74097 \quad (5.8)$$

with a correlation factor of  $R^2 = 0.99556$  (presented at the inset of the Figure 5.6(b)). Therefore, the sensitivity for sensing AA, which is implied by the slope of the graph, is  $209.02718 \mu A.mM^{-1}cm^{-2}$  with the minimum detection limit of  $0.019 \mu M$  ( $S/N = 3$ ).

### 5.3.3 Long-term stability and selectivity

To investigate how the sensitivity of the Au@Ag HNCs as an electrochemical sensor got affected over time, we had performed the long-term stability study. We had conducted the cyclic voltammetry sensing studies of both UA (2 mM) and AA (0.5 mM) after every 1 week over a total period of 4 weeks, using the Au@Ag HNCs coated ITO sheet as electrode. We had found that the current densities had been reduced, and as the time increased, the current densities had reduced more. In Figure 5.7(a) and (b), we have presented the long-term stability studies of UA and AA, respectively. We have found that for sensing UA, the current density had been reduced to 75% of its initial value after 4 weeks. For sensing AA, the current density had been reduced to 69% of its initial value after 4 weeks. So, we can conclude that the long-term stability of the Au@Ag HNCs coated ITO sheet as an electrode for sensing UA and AA is very good, i.e., it is quite stable over time.

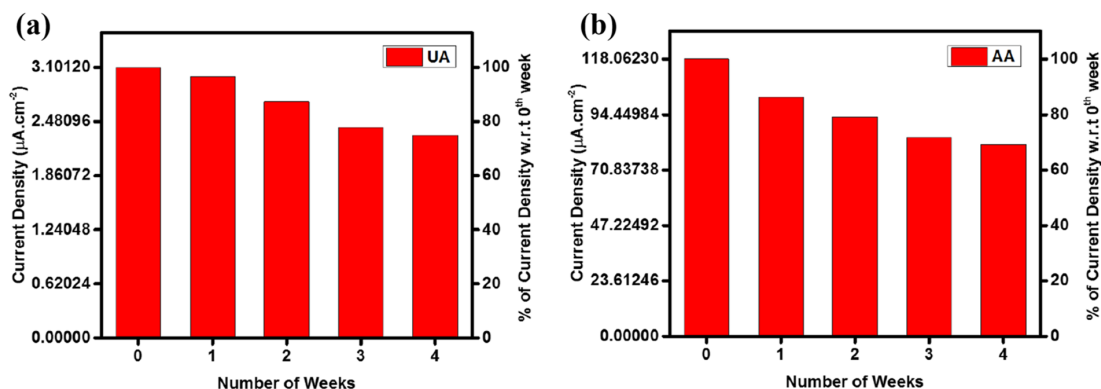


Figure 5.7: Long-term stability performances of the Au@Ag HNCs coated ITO electrode towards electrochemical sensing of (a) UA (2 mM) and (b) AA (0.5 mM).

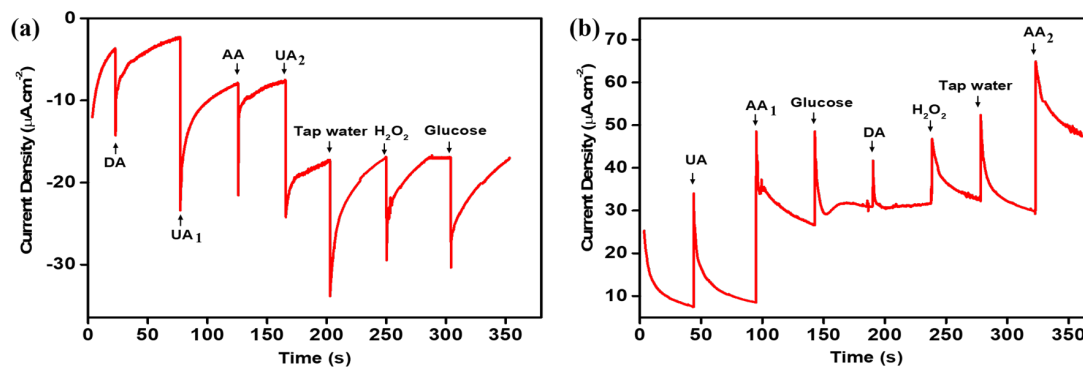


Figure 5.8: *Selectivity study for (a) UA and (b) AA sensing for the Au@Ag HNCs coated ITO electrode.*

An ideal sensor should detect only the desired material anyone wants to detect, not any other material. For that reason, selectivity study is very important for sensing studies. In the Figure 5.8(a), we have presented the selectivity study for Au@Ag HNCs as a sensor for sensing UA only. In this case, the electrode potential was kept fixed at  $-0.36$  V, and different chemicals were added into the electrolyte medium, such as tap water, dopamine (DA),  $H_2O_2$ , glucose, UA and AA. But we could observe that the current density had changed only when UA was added into the medium. As the electrode potential was kept fixed at  $-0.36$  V, which is the reduction potential for UA, only UA was reduced at the electrode. As a result, a change in current density was observed. The other added chemicals remained in the electrolyte medium as they were and did not take part in the current flow. Therefore, if the electrode potential is kept fixed at  $-0.36$  V, the current density changes only when UA solution is being added into the medium, otherwise it remains unchanged. Similarly, when the electrode potential was kept fixed at  $0.55$  V, which is the oxidation potential for AA, the current density changed only when AA solution was added into the medium, otherwise it remained unchanged. This phenomenon was clearly observed during the selectivity study for Au@Ag HNCs as a sensor for sensing AA only, which is presented in the Figure 5.8(b). In this case, we also added different chemical in the electrolyte medium like tap water, DA,  $H_2O_2$ , glucose,

UA and AA, but the current density changed only when AA was added. So, our proposed Au@Ag HNCs could act as both UA and AA sensor independently, at an electrode potential of  $-0.36$  V and  $0.55$  V, respectively.

In each case, we could observe that as soon as UA, AA or any other chemicals were added into the electrolyte medium, the current density increased abruptly and then stabilized to some value. When something was added to the electrolyte medium, it created some disturbances and due to that the current density has changed at the immediate moment it was added and after some time it has stabilized to some value. In every case, we have considered these stabilized values as the current densities at those particular concentrations of UA, AA or any other chemical added into the medium.

With Au@Ag HNCs as electrode, we have measured the concentration of both UA and AA of known concentration. When we added  $1$  mM of UA in the electrolyte solution, we found current density of  $-1.65 \mu A.mM^{-1}$ , which corresponds to UA of concentration  $0.95$  mM. And for  $100 \mu M$  of AA added in the electrolyte solution, we have found a current density of  $30 \mu A.mM^{-1}$ , which corresponds to AA of concentration  $101.7 \mu M$ . The accuracy of sensing both UA and AA is given by %Bias as [459]

$$\%Bias = \frac{measuredvalue - truevalue}{truevalue} \times 100 \quad (5.9)$$

Therefore, the accuracy of sensing UA  $5.00\%$  is and AA is  $1.70\%$ .

## 5.4 Comparison with reported results

The detection performances, i.e, various properties of a sensor like sensitivity, lowest detection limit and range of linear response of various previously proposed electrochemical sensors for sensing UA and AA respectively, have been compared with the Au@Ag HNCs coated ITO sensor we have proposed. In the Table 5.1, we have summarized a comparative study of these various properties of different UA sensors with our propose sensor for sensing UA.

Similarly, in the Table 5.2, we have summarized a comparative study of those various properties of different AA sensors with our propose sensor for sensing AA.

Comparing the values of linear range, sensitivity and detection limit for our proposed sensors for sensing both UA and AA with other previously reported sensors, we can conclude that the proposed Au@Ag HNCs coated ITO sensors have a better linear range, with great sensitivity and very small detection limit for sensing both UA and AA.

Table 5.1: Comparison of the analytical performances between the proposed UA sensor with some other previously reported UA electrochemical sensors.

Electrodes	Linear range ( $\mu M$ )	Sensitivity ( $\mu M.mM^{-1} cm^{-2}$ )	Detection limit ( $\mu M$ )	Reference/Remarks
g-C <sub>3</sub> N <sub>4</sub> NS	100 – 1000	202.5	4.45	[460]
PDA-rGO/Au/SPCE	2.5 – 1000	4.4	0.74	[461]
Nafion/Urlicase/ZnO NSs/Ag/Si	50 – 2000	129.81	0.019	[462]
Urlicase/Au NPs/MWCNT/Au	10 – 800	440	10	[463]
Nafion/Urlicase/ZnO micro/NWs/Au	100 – 590	89.74	25.6	[464]
Urlicase/ZnO: N/ITO /glass	50 – 1000	1100	40	[465]
Nafion/Urlicase-ZnO NRs/Ag/glass	10 – 4560	239.67	0.005	[466]
GCE/MWCNT-PEI	5 – 50	750	0.1	[467]
GCE/MWCNT@PDOP@PtNPu	0.3 – 13	1.03	0.12	[468]
CPE/MWCNT/a-CD	5 – 40	0.325	5	[469]
GCE/fMWCNT/Q	1 – 125	0.078	0.575	[470]
Au-TOH@Ag-HNCs/ITO	50 – 2000	1.509	0.36	Our work

Table 5.2: Comparison of the analytical performances between the proposed AA sensor with some other previously reported AA electrochemical sensors.

Electrodes	Linear range ( $\mu M$ )	Sensitivity ( $\mu M.mM^{-1} cm^{-2}$ )	Detection limit ( $\mu M$ )	Reference/Remarks
Graphene doped CPE	0.1 – 106	3.31571	0.07	[471]
CoTNPPc-MWNTs/GCE	10 – 1600	–	5	[472]
CoPc-MWNTs/GCE	10 – 2600	55.79076	1	[473]
BPEI/EGDE/[Fe(CN) <sub>6</sub> ] <sup>4-</sup> /GCE	1 – 5000	28.2	1	[474]
Gr/CuPc/PANI/SPE	0.5 – 120	24.46	0.063	[475]
PANI micro-tube/ITO	5 – 4700	178.2	0.28	[476]
MSA-PANI/MWCNTs/GCE	20 – 29600	363	0.6	[477]
DBSA-PANI/SPE	500 – 8000	10.75	8.3	[478]
PANI/SPCE	30 – 270	17.7	33	[479]
PANI/Au/GCE	10 – 12000	25.69	8.2	[480]
Au/SiO <sub>2</sub> /PANI/CPE	150 – 8000	21.88	3.375	[481]
PANI-Ni/SPCE	2 – 1210	479	0.4	[482]
PANI/HNTs/ITO	5 – 5500	826.53	0.21	[483]
RGO-Au/ITO	25 – 300	314.07	6.80	[484]
Au-TOH@Ag-HNCs/ITO	50 – 500	209.03	0.019	Our work

## 5.5 Conclusion

We have investigated the cyclic voltammetry and amperometric studies using the synthesized Au@Ag NSs, NCs, HNSs and HNCs coated ITO glass substrate as electrodes. The cyclic voltammetry plots of these electrodes show how the interfacial area of the NPs affects the current. As the Au@Ag HNCs have maximum surface area compared to remaining NPs, they give the maximum current. The cyclic voltammetry has been performed for all the electrodes by adding UA and AA into the electrolyte solution, and it has been observed that the current has increased with increasing concentrations of UA and AA.

These observations lead us to perform the amperometric studies for sensing UA and AA with the Au@Ag HNCs coated ITO glass electrode, as it produces the maximum current. From the amperometric sensing studies, the sensitivity, lowest detection limit and range of detection have been found out. The results show very improved sensitivity along with other properties by comparing with some previously reported results. Hence, we can conclude that the Au@Ag HNCs coated electrode can be applicable in sensing both UA and AA with very high sensitivity and small lowest detection limit.

# Chapter 6

## Conclusion

---

---

*In this chapter a quick recap has been presented on the works discussed in this thesis and the overall conclusions are briefly summarized. Some future predictions of our study have also been discussed.*

---

---

## 6.1 Summary

In recent years, research on nanoparticles has become a hot topic in material sciences and chemistry for their unusual properties and a wide range of applications. SERS is an ultra sensitive vibrational spectroscopic method which provides us an idea about the near field behavior of the electromagnetic field around the NPs. Besides it has a wide application in sensing molecules with very high sensitivity. The main goal of this thesis work was to synthesize core-shell NPs of different morphologies with high energy facets and explore their surface plasmon related optical properties using TEM, UV-vs-NIR spectroscopy and SERS. The SERS spectra of the NPs show enhanced electric field around them. Finally, the NPs were used as nonenzymatic electrochemical biosensors for sensing UA and AA with very high sensitivity and very small lowest detection limit.

- In **chapter 1**, a brief overview of the core-shell NPs has been discussed. The properties of the NPs are highly dependent on their shape and size. This was the main motivation for synthesizing NPs of different shapes and sizes. We have observed that core-shell NPs have superior properties over their monometallic counterpart. Various noble metal NPs of sizes and shapes, enclosed by high energy facets have been obtained using different synthesis methods. The properties of any metallic NP are governed by its surface plasmon, which is the collective oscillations of electrons in the conduction bands. The theoretical background of SERS and its relation with the surface plasmon has been discussed in this chapter. Finally, the importance of biosensors and their advantages over other sensors have been discussed.
- In **chapter 2**, a brief description of the synthesis methods of different types of core-shell NPs such as Au@Ag NRs with Au NBPs as core, Au@Ag NSs and NCs with Au TOH as core, Au@Ag nanotriangles with Au triangles as core

and Au@Pd NCs with Au octahedron as core, has been presented. All of the NPs were synthesized following the seed mediated chemical growth method. Later, the Au@Ag NSs and NCs with Au TOH as core, have been transformed into core-shell HNPs using galvanic replacement reaction. Since the TEM is the major characterization tool in this thesis for observing the shape and size of the synthesized NPs, it has been discussed in detail with various modes of operations. The working principle of UV-vs-NIR spectrometer, SERS and nonenzymatic electrochemical biosensors have been discussed in brief.

- In **chapter 3**, the TEM observations of the synthesized NPs have been presented. From the bright-field TEM images, we have measured the sizes of the different NPs. The HRTEM images of the NPs were also acquired. From the HRTEM images, it was observed that the synthesized NPs are single crystalline in nature. The growth directions and indices of the bounding facets of the NPs have been found out from the HRTEM images. It was observed that the Au TOH NPs are bounded by  $\{221\}$  and  $\{331\}$  planes. The growth of the NPs into different shapes from the seed NPs have been examined. The bright-field TEM images do not show the details of the core-shell NPs. The clear pictures of the core-shell NPs were observed from the STEM-HAADF images due to Z contrast. The mapped images using EDX were also presented in this chapter, which clearly shows the elements present in the core and shell separately.
- In **chapter 4**, the plasmonic properties of the NPs were discussed. The acquired absorption spectra of the synthesized NPs were presented. The absorption spectra of the Au@Ag NRs with Au NBPs as core shows multiple plasmon peaks throughout the absorption spectra. As the lengths of the NRs have increased, all the peaks were red shifted. Besides the longitudinal and transvers dipolar modes, different multipolar modes along with the coupling

modes have been observed. Comparing the absorption spectra of Au@Ag NSs or NCs with their hollow configuration, it was observed that the contribution from the shell Ag part is very high compared to the core Au part for Au@Ag NSs or NCs. Whereas, for the HNPs, the contribution from the core Au part has been intensified. To investigate the near field behavior of the electromagnetic field, SERS spectra of the NPs were acquired using different analytes. For Au@Ag NRs of different lengths, maximum enhancement was observed for Au@Ag NRs of length 450 nm, as the plasmonic wavelength matches with the laser excitation wavelength. Comparing the SERS enhancement of Au@Ag NRs and Ag NRs, Au@Ag NRs shows higher enhancement due to the presence of multiple sharp edges and tips in the core Au NPs and the lattice strain at the core and shell interfaces. For Au@Ag NSs and NCs, higher enhancement was observed for Au@Ag NCs, for the presence of multiple edges, corners and tips in the NCs. Au@Ag HNSs and HNCs show much higher enhancement compared to Au@Ag NSs and NCs respectively. For the HNPs, the incoming electromagnetic rays also interact with the Au cores and multiple hot spots are generated at the edges and tips of the Au TOH NPs as well as at the narrow hollow spaces between the cores and shells. The FDTD simulations were performed which verified the experimental SERS observations.

- In **chapter 5**, the electrochemical properties of the Au TOH NPs along with Au@Ag NSs, NCs, HNSs and HNCs are presented. The interfacial charge transfer for the Au@Ag HNCs was found maximum for their higher surface area along with the presence of the sharp edges and tips which have the maximum charge density. The cyclic voltammetry studies were performed by adding different amounts of UA and AA in the electrolyte medium and it was observed that as the concentrations of the UA and AA have increased, the current densities also increased, which implies that using these NPs as electrode could work as sensors. As the change in current densities is maxi-

mum for Au@Ag HNCs for both UA and AA, hence the amperometric studies were performed using Au@Ag HNCs-coated electrode only. It was observed that the Au@Ag HNCs as biosensor has greater sensitivity and very small lowest detection limit for both AA and UA, which are comparable to recently reported works.

## 6.2 Outlook

This thesis work deals with the synthesis of core-shell NPs where the core NPs are enclosed by the high energy facets. The core-shell NPs show enhanced optical properties as well as stability and tunability. The developments of core-shell NPs of different morphologies and constituting materials have opened up a wide range of applications in different fields. Recently, core-shell NPs with metallic shell and polymer core are being used for biomedical applications, solar cells and organic LED (OLED) [485–487]. Core-shell NPs made of materials like Au, Ag, Pd, Pt have gained very special attention in nanotechnology because their properties distinctly differ from their respective bulk counterpart and have a wide range of applications in various fields like solar cells [100–102], catalysis [237–241], biomedicine [229, 235, 236], bioimaging [250, 251] etc. The core-shell NPs have a huge importance in the field of medicine and biotechnology. They are used for plastic surgery and tissue engineering [217, 226], drug targeting or drug delivery [211, 217, 218, 222, 225], biosensors [182, 191, 233], and cancer therapy [488–492].

SERS is an excellent technique for understanding the near field behavior of the electromagnetic field around the NPs. On the other hand, it is applied for biosensing purposes as well as a precise imaging tool for both *ex vivo* and *in vivo* samples [493–496]. Immuno-SERS (ISERS) microscopy is a recently developed technique which is used for imaging antibodies for selective protein recognition [497]. SERE is also

being widely used for environmental purposes such as monitoring and quantification of toxins and chemicals present in the environment [498–501], bacteria signaling metabolites [502], heavy metals [503–505], etc. It is also being used for the analysis of the quality of water or food for its excellent sensitivity [506, 507].

Nonenzymatic electrochemical biosensor is a very useful sensor for sensing biomolecules. For greater sensitivity, the HNPs coated modified electrode was used as biosensors for their higher interfacial areas. As the outputs of the sensors are electrical signals, so they are very easy to analyze. Besides, it provides very fast responses and does not need any special arrangements for the set up. The development of various types of NPs modified electrodes has enabled us for the detection of different biomolecules with huge sensitivity and selectivity.

In summery, this thesis work deals with the development of various core-shell NPs. It was observed that the properties of the core-shell NPs are highly dependent on their shape and size. They have been used as efficient SERS substrates which provide huge EF for their unusual structures. The dependence of SERS enhancement on the structure and size of the NPs was investigated. In short, we have designed some NPs which provide huge SERS enhancement. The NPs were transformed into HNPs so that they can be used as biosensors with excellent sensitivity. All these core-shell NPs may be very useful for future perspectives as SERS substrates or biosensors or in any other field. Though any kind of prediction for future perspectives is inherently risky. But, one can definitely conclude that the core-shell NPs must be very useful in the upcoming years for their wide range of applications in various fields.

# Bibliography

- [1] P. Sciau, *Nanoparticles in ancient materials: the metallic lustre decorations of medieval ceramics*, Vol. 115, INTECH Open Access Publisher, **2012**.
- [2] M. Faraday, *Philos Trans R Soc London* **1857**, 147, 145.
- [3] R. A. Zsigmondy, *Nobel lecture* **1926**, 11.
- [4] R. P. Feynman, *California Institute of Technology Engineering and Science magazine* **1960**.
- [5] A. Thompson, B. N. Taylor, Guide for the Use of the International System of Units (SI), tech. rep., **2008**.
- [6] R. Siegel in *Physics of new materials*, Springer, **1994**, pp. 65–105.
- [7] M. Kiskinova, *Chemical reviews* **1996**, 96, 1431–1448.
- [8] G. A. Somorjai, *Chemical reviews* **1996**, 96, 1223–1236.
- [9] F. Seker, K. Meeker, T. F. Kuech, A. B. Ellis, *Chemical reviews* **2000**, 100, 2505–2536.
- [10] G. C. Pimentel, J. A. Coonrod, Opportunities in Chemistry. Tech. rep., NATIONAL ACADEMY OF SCIENCES WASHINGTON DC, **1985**, pp. 240–243.
- [11] Z. Wang, Transmission electron microscopy of shape-controlled nanocrystals and their assemblies, **2000**.

- [12] Z.-Y. Jiang, Q. Kuang, Z.-X. Xie, L.-S. Zheng, *Advanced Functional Materials* **2010**, *20*, 3634–3645.
- [13] A. Kuzume, E. Herrero, J. M. Feliu, R. J. Nichols, D. J. Schiffrin, *Physical Chemistry Chemical Physics* **2004**, *6*, 619–625.
- [14] Z.-Y. Zhou, N. Tian, J.-T. Li, I. Broadwell, S.-G. Sun, *Chemical Society Reviews* **2011**, *40*, 4167–4185.
- [15] Q.-S. Chen, Z.-Y. Zhou, F. J. Vidal-Iglesias, J. Solla-Gullón, J. M. Feliu, S.-G. Sun, *Journal of the American Chemical Society* **2011**, *133*, 12930–12933.
- [16] C.-W. Yang, K. Chanda, P.-H. Lin, Y.-N. Wang, C.-W. Liao, M. H. Huang, *Journal of the American Chemical Society* **2011**, *133*, 19993–20000.
- [17] D.-S. Yang, D. Bhattacharjya, S. Inamdar, J. Park, J.-S. Yu, *Journal of the American Chemical Society* **2012**, *134*, 16127–16130.
- [18] A. R. Tao, S. Habas, P. Yang, *small* **2008**, *4*, 310–325.
- [19] Z. Quan, Y. Wang, J. Fang, *Accounts of chemical research* **2013**, *46*, 191–202.
- [20] H. Zhang, M. Jin, Y. Xia, *Angewandte Chemie International Edition* **2012**, *51*, 7656–7673.
- [21] D. Wang, Y. Liu, T. You, *CrystEngComm* **2010**, *12*, 4028–4030.
- [22] P.-J. Chung, L.-M. Lyu, M. H. Huang, *Chemistry—A European Journal* **2011**, *17*, 9746–9752.
- [23] M. L. Personick, M. R. Langille, J. Zhang, N. Harris, G. C. Schatz, C. A. Mirkin, *Journal of the American Chemical Society* **2011**, *133*, 6170–6173.
- [24] F. Lu, Y. Zhang, L. Zhang, Y. Zhang, J. X. Wang, R. R. Adzic, E. A. Stach, O. Gang, *Journal of the American Chemical Society* **2011**, *133*, 18074–18077.
- [25] M. Jin, H. Zhang, Z. Xie, Y. Xia, *Angewandte Chemie International Edition* **2011**, *50*, 7850–7854.

- [26] N. Tian, Z.-Y. Zhou, N.-F. Yu, L.-Y. Wang, S.-G. Sun, *Journal of the American Chemical Society* **2010**, *132*, 7580–7581.
- [27] N. Tian, Z.-Y. Zhou, S.-G. Sun, *Chemical communications* **2009**, 1502–1504.
- [28] Z.-Y. Zhou, N. Tian, Z.-Z. Huang, D.-J. Chen, S.-G. Sun, *Faraday discussions* **2009**, *140*, 81–92.
- [29] X. Huang, Z. Zhao, J. Fan, Y. Tan, N. Zheng, *Journal of the American chemical Society* **2011**, *133*, 4718–4721.
- [30] H.-L. Wu, C.-H. Kuo, M. H. Huang, *Langmuir* **2010**, *26*, 12307–12313.
- [31] H.-G. Liao, Y.-X. Jiang, Z.-Y. Zhou, S.-P. Chen, S.-G. Sun, *Angewandte Chemie International Edition* **2008**, *47*, 9100–9103.
- [32] J. W. Hong, S.-U. Lee, Y. W. Lee, S. W. Han, *Journal of the American Chemical Society* **2012**, *134*, 4565–4568.
- [33] X. Huang, S. Tang, H. Zhang, Z. Zhou, N. Zheng, *Journal of the American Chemical Society* **2009**, *131*, 13916–13917.
- [34] M. H. Huang, P.-H. Lin, *Advanced Functional Materials* **2012**, *22*, 14–24.
- [35] F. Wang, C. Li, L.-D. Sun, H. Wu, T. Ming, J. Wang, J. C. Yu, C.-H. Yan, *Journal of the American Chemical Society* **2011**, *133*, 1106–1111.
- [36] W. Niu, S. Zheng, D. Wang, X. Liu, H. Li, S. Han, J. Chen, Z. Tang, G. Xu, *Journal of the American Chemical Society* **2009**, *131*, 697–703.
- [37] W. Niu, L. Zhang, G. Xu, *Acs Nano* **2010**, *4*, 1987–1996.
- [38] T. K. Sau, C. J. Murphy, *Journal of the American Chemical Society* **2004**, *126*, 8648–8649.
- [39] Y. Yu, Q. Zhang, X. Lu, J. Y. Lee, *The Journal of Physical Chemistry C* **2010**, *114*, 11119–11126.
- [40] W. Niu, Z.-Y. Li, L. Shi, X. Liu, H. Li, S. Han, J. Chen, G. Xu, *Crystal Growth and Design* **2008**, *8*, 4440–4444.

- [41] C. J. Johnson, E. Dujardin, S. A. Davis, C. J. Murphy, S. Mann, *Journal of Materials Chemistry* **2002**, *12*, 1765–1770.
- [42] C. J. DeSantis, A. C. Sue, M. M. Bower, S. E. Skrabalak, *ACS nano* **2012**, *6*, 2617–2628.
- [43] W. Niu, G. Xu, *Nano Today* **2011**, *6*, 265–285.
- [44] M. L. Personick, M. R. Langille, J. Zhang, C. A. Mirkin, *Nano letters* **2011**, *11*, 3394–3398.
- [45] T. Ming, W. Feng, Q. Tang, F. Wang, L. Sun, J. Wang, C. Yan, *Journal of the American Chemical Society* **2009**, *131*, 16350–16351.
- [46] X. Xia, J. Zeng, B. McDearmon, Y. Zheng, Q. Li, Y. Xia, *Angewandte Chemie International Edition* **2011**, *50*, 12542–12546.
- [47] C.-L. Lu, K. S. Prasad, H.-L. Wu, J.-a. A. Ho, M. H. Huang, *Journal of the American Chemical Society* **2010**, *132*, 14546–14553.
- [48] L. Zhang, W. Niu, Z. Li, G. Xu, *Chemical Communications* **2011**, *47*, 10353–10355.
- [49] D. Kim, Y. W. Lee, S. B. Lee, S. W. Han, *Angewandte Chemie International Edition* **2012**, *51*, 159–163.
- [50] Y. Yu, Q. Zhang, B. Liu, J. Y. Lee, *Journal of the American Chemical Society* **2010**, *132*, 18258–18265.
- [51] B. Lim, M. Jiang, J. Tao, P. H. Camargo, Y. Zhu, Y. Xia, *Advanced Functional Materials* **2009**, *19*, 189–200.
- [52] X. Kou, S. Zhang, C.-K. Tsung, M. H. Yeung, Q. Shi, G. D. Stucky, L. Sun, J. Wang, C. Yan, *The Journal of Physical Chemistry B* **2006**, *110*, 16377–16383.
- [53] B. J. Wiley, Y. Xiong, Z.-Y. Li, Y. Yin, Y. Xia, *Nano letters* **2006**, *6*, 765–768.

- [54] E. Carbó-Argibay, B. Rodríguez-González, S. Gómez-Graña, A. Guerrero-Martínez, I. Pastoriza-Santos, J. Pérez-Juste, L. M. Liz-Marzán, *Angewandte Chemie International Edition* **2010**, *49*, 9397–9400.
- [55] H. Katz-Boon, C. J. Rossouw, M. Weyland, A. M. Funston, P. Mulvaney, J. Etheridge, *Nano letters* **2011**, *11*, 273–278.
- [56] A. Chernov, *SOVIET PHYSICS CRYSTALLOGRAPHY USSR* **1972**, *16*, 734.
- [57] J. Li, Y. Zheng, J. Zeng, Y. Xia, *Chemistry—A European Journal* **2012**, *18*, 8150–8156.
- [58] Y. Xiong, H. Cai, B. J. Wiley, J. Wang, M. J. Kim, Y. Xia, *Journal of the American Chemical Society* **2007**, *129*, 3665–3675.
- [59] N. Zettsu, J. M. McLellan, B. Wiley, Y. Yin, Z.-Y. Li, Y. Xia, *Angewandte Chemie International Edition* **2006**, *45*, 1288–1292.
- [60] N. Fan, Y. Yang, W. Wang, L. Zhang, W. Chen, C. Zou, S. Huang, *ACS nano* **2012**, *6*, 4072–4082.
- [61] P. Nolte, S. Andreas, K. Nikolai, J.-P. N. Yun, J. Nicole, D. Helmut, *Nano letters* **2011**, *11*, 4697–4700.
- [62] L. Zhang, J. Zhang, Q. Kuang, S. Xie, Z. Jiang, Z. Xie, L. Zheng, *Journal of the American Chemical Society* **2011**, *133*, 17114–17117.
- [63] T. T. Tran, X. Lu, *The Journal of Physical Chemistry C* **2011**, *115*, 3638–3645.
- [64] D. Y. Kim, S. H. Im, O. O. Park, *Crystal growth & design* **2010**, *10*, 3321–3323.
- [65] G. H. Jeong, M. Kim, Y. W. Lee, W. Choi, W. T. Oh, Q.-H. Park, S. W. Han, *Journal of the American Chemical Society* **2009**, *131*, 1672–1673.

- [66] L. Zhang, D. Chen, Z. Jiang, J. Zhang, S. Xie, Q. Kuang, Z. Xie, L. Zheng, *Nano Research* **2012**, *5*, 181–189.
- [67] Y. Xia, Y. Xiong, B. Lim, S. E. Skrabalak, *Angewandte Chemie International Edition* **2009**, *48*, 60–103.
- [68] I. Pastoriza-Santos, L. M. Liz-Marzán, *Advanced Functional Materials* **2009**, *19*, 679–688.
- [69] N. Tian, Z.-Y. Zhou, S.-G. Sun, *The Journal of Physical Chemistry C* **2008**, *112*, 19801–19817.
- [70] N. Tian, Z.-Y. Zhou, S.-G. Sun, Y. Ding, Z. L. Wang, *science* **2007**, *316*, 732–735.
- [71] M.-C. Daniel, D. Astruc, *Chemical reviews* **2004**, *104*, 293–346.
- [72] M. B. Gawande, V. D. Bonifácio, R. S. Varma, I. D. Nogueira, N. Bundaleski, C. A. A. Ghumman, O. M. Teodoro, P. S. Branco, *Green Chemistry* **2013**, *15*, 1226–1231.
- [73] H. C. Zeng, *Accounts of chemical research* **2013**, *46*, 226–235.
- [74] A. K. Geim, K. S. Novoselov in *Nanoscience and technology: a collection of reviews from nature journals*, World Scientific, **2010**, pp. 11–19.
- [75] V. Georgakilas, A. B. Bourlinos, R. Zboril, T. A. Steriotis, P. Dallas, A. K. Stubos, C. Trapalis, *Chemical Communications* **2010**, *46*, 1766–1768.
- [76] V. Georgakilas, M. Otyepka, A. B. Bourlinos, V. Chandra, N. Kim, K. C. Kemp, P. Hobza, R. Zboril, K. S. Kim, *Chemical reviews* **2012**, *112*, 6156–6214.
- [77] M. Pykal, K. afáová, K. Machalová iková, P. Jureka, A. B. Bourlinos, R. Zboil, M. Otyepka, *The Journal of Physical Chemistry C* **2013**, *117*, 11800–11803.

- [78] R. Zboil, F. Karlick, A. B. Bourlinos, T. A. Steriotis, A. K. Stubos, V. Georgakilas, K. afáová, D. Jank, C. Trapalis, M. Otyepka, *small* **2010**, *6*, 2885–2891.
- [79] M. B. Gawande, P. S. Branco, R. S. Varma, *Chemical Society Reviews* **2013**, *42*, 3371–3393.
- [80] A.-H. Lu, E. e. Salabas, F. Schüth, *Angewandte Chemie International Edition* **2007**, *46*, 1222–1244.
- [81] M. B. Gawande, A. K. Rathi, I. D. Nogueira, R. S. Varma, P. S. Branco, *Green Chemistry* **2013**, *15*, 1895–1899.
- [82] Q. Song, Z. J. Zhang, *Journal of the American Chemical Society* **2004**, *126*, 6164–6168.
- [83] J. Chen, T. Herricks, Y. Xia, *Angewandte Chemie International Edition* **2005**, *44*, 2589–2592.
- [84] G. Salazar-Alvarez, J. Qin, V. Sepelak, I. Bergmann, M. Vasilakaki, K. Trohidou, J. Ardisson, W. Macedo, M. Mikhaylova, M. Muhammed, et al., *Journal of the American Chemical Society* **2008**, *130*, 13234–13239.
- [85] E. Schmidt, A. Vargas, T. Mallat, A. Baiker, *Journal of the american chemical society* **2009**, *131*, 12358–12367.
- [86] Z. Wang, T. Ahmad, M. El-Sayed, *Surface Science* **1997**, *380*, 302–310.
- [87] X.-W. Wei, G.-X. Zhu, Y.-J. Liu, Y.-H. Ni, Y. Song, Z. Xu, *Chemistry of Materials* **2008**, *20*, 6248–6253.
- [88] M. Yamada, S. Kon, M. Miyake, *Chemistry letters* **2005**, *34*, 1050–1051.
- [89] J. Ahmed, S. Sharma, K. V. Ramanujachary, S. E. Lofland, A. K. Ganguli, *Journal of colloid and interface science* **2009**, *336*, 814–819.
- [90] S. A. El-Safty, *Journal of colloid and interface science* **2008**, *319*, 477–488.

- [91] X. Ren, D. Han, D. Chen, F. Tang, *Materials Research Bulletin* **2007**, *42*, 807–813.
- [92] T.-Z. Ren, Z.-Y. Yuan, W. Hu, X. Zou, *Microporous and Mesoporous Materials* **2008**, *112*, 467–473.
- [93] N. J. Suematsu, Y. Ogawa, Y. Yamamoto, T. Yamaguchi, *Journal of colloid and interface science* **2007**, *310*, 648–652.
- [94] L. Wu, C. Y. Jimmy, L. Zhang, X. Wang, S. Li, *Journal of Solid State Chemistry* **2004**, *177*, 3666–3674.
- [95] J.-S. Hu, Y.-G. Guo, H.-P. Liang, L.-J. Wan, L. Jiang, *Journal of the American Chemical Society* **2005**, *127*, 17090–17095.
- [96] M. Jitianu, D. V. Goia, *Journal of Colloid and Interface Science* **2007**, *309*, 78–85.
- [97] H.-M. Bok, S. Kim, S.-H. Yoo, S. K. Kim, S. Park, *Langmuir* **2008**, *24*, 4168–4173.
- [98] H.-M. Bok, K. L. Shuford, S. Kim, S. K. Kim, S. Park, *Nano letters* **2008**, *8*, 2265–2270.
- [99] S. R. Nicewarner-Pena, R. G. Freeman, B. D. Reiss, L. He, D. J. Peña, I. D. Walton, R. Cromer, C. D. Keating, M. J. Natan, *Science* **2001**, *294*, 137–141.
- [100] S. Park, S.-W. Chung, C. A. Mirkin, *Journal of the American Chemical Society* **2004**, *126*, 11772–11773.
- [101] S. Park, J.-H. Lim, S.-W. Chung, C. A. Mirkin, *Science* **2004**, *303*, 348–351.
- [102] W. F. Paxton, K. C. Kistler, C. C. Olmeda, A. Sen, S. K. St. Angelo, Y. Cao, T. E. Mallouk, P. E. Lammert, V. H. Crespi, *Journal of the American Chemical Society* **2004**, *126*, 13424–13431.
- [103] X. Peng, L. Manna, W. Yang, J. Wickham, E. Scher, A. Kadavanich, A. P. Alivisatos, *Nature* **2000**, *404*, 59–61.

- [104] S.-H. Yoo, S. Park, *Advanced Materials* **2007**, *19*, 1612–1615.
- [105] G. Cao, D. Liu, *Advances in colloid and interface science* **2008**, *136*, 45–64.
- [106] T. R. Kline, M. Tian, J. Wang, A. Sen, M. W. Chan, T. E. Mallouk, *Inorganic chemistry* **2006**, *45*, 7555–7565.
- [107] M. Li, T. S. Mayer, J. A. Sioss, C. D. Keating, R. B. Bhiladvala, *Nano letters* **2007**, *7*, 3281–3284.
- [108] Z. Liu, D. Elbert, C.-L. Chien, P. C. Searson, *Nano letters* **2008**, *8*, 2166–2170.
- [109] D. J. Pena, J. K. Mbindyo, A. J. Carado, T. E. Mallouk, C. D. Keating, B. Razavi, T. S. Mayer, *The Journal of Physical Chemistry B* **2002**, *106*, 7458–7462.
- [110] D. Routkevitch, T. Bigioni, M. Moskovits, J. M. Xu, *The Journal of Physical Chemistry* **1996**, *100*, 14037–14047.
- [111] J. A. Sioss, C. D. Keating, *Nano letters* **2005**, *5*, 1779–1783.
- [112] Y. Wu, T. Livneh, Y. X. Zhang, G. Cheng, J. Wang, J. Tang, M. Moskovits, G. D. Stucky, *Nano Letters* **2004**, *4*, 2337–2342.
- [113] X. Qu, L. Omar, T. B. H. Le, L. Tetley, K. Bolton, K. W. Chooi, W. Wang, I. F. Uchegbu, *Langmuir* **2008**, *24*, 9997–10004.
- [114] A. Michailowski, D. AlMawlawi, G. Cheng, M. Moskovits, *Chemical physics letters* **2001**, *349*, 1–5.
- [115] K. B. Shelimov, M. Moskovits, *Chemistry of materials* **2000**, *12*, 250–254.
- [116] T.-Y. Shin, S.-H. Yoo, S. Park, *Chemistry of Materials* **2008**, *20*, 5682–5686.
- [117] R. Xiao, S. I. Cho, R. Liu, S. B. Lee, *Journal of the American Chemical Society* **2007**, *129*, 4483–4489.
- [118] C. M. Lieber, *Solid state communications* **1998**, *107*, 607–616.

- [119] R. E. Smalley, B. I. Yakobson, *Solid state communications* **1998**, *107*, 597–606.
- [120] D. Stuart, A. Haes, C. Yonzon, E. Hicks, R. P. Van Duyne in IEE Proceedings-Nanobiotechnology, *Vol. 152*, IET, **2005**, pp. 13–32.
- [121] J. E. Millstone, S. J. Hurst, G. S. Métraux, J. I. Cutler, C. A. Mirkin, *small* **2009**, *5*, 646–664.
- [122] H. Lee, S. E. Habas, S. Kwekin, D. Butcher, G. A. Somorjai, P. Yang, *Angewandte Chemie International Edition* **2006**, *45*, 7824–7828.
- [123] R. Narayanan, M. A. El-Sayed, *Journal of the American Chemical Society* **2004**, *126*, 7194–7195.
- [124] Y. Zheng, Y. Cheng, Y. Wang, F. Bao, L. Zhou, X. Wei, Y. Zhang, Q. Zheng, *The Journal of Physical Chemistry B* **2006**, *110*, 3093–3097.
- [125] S. K. Gupta, M. Talati, P. K. Jha in Materials Science Forum, *Vol. 570*, Trans Tech Publ, **2008**, pp. 132–137.
- [126] Y. Sun, Y. Xia, *Advanced Materials* **2003**, *15*, 695–699.
- [127] A. Henglein, *Chemical reviews* **1989**, *89*, 1861–1873.
- [128] H. C. Youn, S. Baral, J. H. Fendler, *The Journal of Physical Chemistry* **1988**, *92*, 6320–6327.
- [129] L. Spanhel, H. Weller, A. Henglein, *Journal of the American Chemical Society* **1987**, *109*, 6632–6635.
- [130] C. F. Hoener, K. A. Allan, A. J. Bard, A. Campion, M. A. Fox, T. E. Mallouk, S. E. Webber, J. M. White, *The Journal of Physical Chemistry* **1992**, *96*, 3812–3817.
- [131] I. Honma, T. Sano, H. Komiyama, *The Journal of Physical Chemistry* **1993**, *97*, 6692–6695.

- [132] H. Zhou, H. Sasahara, I. Honma, H. Komiyama, J. W. Haus, *Chemistry of materials* **1994**, *6*, 1534–1541.
- [133] L. Hong, R. Vilar, W. Youming, *Journal of materials science* **1997**, *32*, 5545–5550.
- [134] R. Subramanian, P. Denney, J. Singh, M. Otooni, *Journal of materials science* **1998**, *33*, 3471–3477.
- [135] D. Jang, B. Oh, D. Kim in High-Power Laser Ablation IV, *Vol. 4760*, International Society for Optics and Photonics, **2002**, pp. 1024–1031.
- [136] P. Kumar, R. Kumar, D. Kanjilal, M. Knobel, P. Thakur, K. Chae, *Journal of Vacuum Science & Technology B: Microelectronics and Nanometer Structures Processing Measurement and Phenomena* **2008**, *26*, L36–L40.
- [137] A. C. Dodd, *Powder Technology* **2009**, *196*, 30–35.
- [138] W. Deng, W. Xia, C. Li, Y. Tang, *Journal of Materials Processing Technology* **2009**, *209*, 4521–4526.
- [139] M. Salari, P. Marashi, M. Rezaee, et al., *Journal of alloys and compounds* **2009**, *469*, 386–390.
- [140] R. Sasikumar, R. Arunachalam, *Materials Letters* **2009**, *63*, 2426–2428.
- [141] Y. Wang, K. Cai, X. Yao, *Journal of Solid State Chemistry* **2009**, *182*, 3383–3386.
- [142] S.-H. Yoo, L. Liu, S. Park, *Journal of colloid and interface science* **2009**, *339*, 183–186.
- [143] O. Sneh, R. B. Clark-Phelps, A. R. Londergan, J. Winkler, T. E. Seidel, *Thin solid films* **2002**, *402*, 248–261.
- [144] R. P. Chaudhary, K. Kangasniemi, M. Takahashi, S. K. Mohanty, A. R. Koymen, *Journal of Functional Biomaterials* **2017**, *8*, 46.

- [145] L. Cui, Z.-P. Liu, D.-G. Yu, S.-P. Zhang, S. A. Bligh, N. Zhao, *Colloid and Polymer Science* **2014**, *292*, 2089–2096.
- [146] D. Joseph, Y. S. Huh, Y.-K. Han, *Sensors and Actuators B: Chemical* **2019**, *288*, 120–126.
- [147] D. Liu, H. Zhang, S. Cito, J. Fan, E. Mäkilä, J. Salonen, J. Hirvonen, T. M. Sikanen, D. A. Weitz, H. A. Santos, *Nano Letters* **2017**, *17*, 606–614.
- [148] X. Sun, Y. Li, *Angewandte Chemie International Edition* **2004**, *43*, 597–601.
- [149] R. Ghosh Chaudhuri, S. Paria, *Chemical reviews* **2012**, *112*, 2373–2433.
- [150] A. Pandikumar, S.-P. Lim, S. Jayabal, N. M. Huang, H. N. Lim, R. Ramaraj, *Renewable and Sustainable Energy Reviews* **2016**, *60*, 408–420.
- [151] H.-L. Jiang, T. Akita, Q. Xu, *Chemical Communications* **2011**, *47*, 10999–11001.
- [152] S. Oldenburg, R. Averitt, S. Westcott, N. Halas, *Chemical Physics Letters* **1998**, *288*, 243–247.
- [153] F. Caruso, M. Spasova, V. Salgueiriño-Maceira, L. Liz-Marzán, *Advanced Materials* **2001**, *13*, 1090–1094.
- [154] T. Hartman, C. S. Wondergem, N. Kumar, A. van den Berg, B. M. Weckhuysen, *The journal of physical chemistry letters* **2016**, *7*, 1570–1584.
- [155] J. N. Anker, W. P. Hall, O. Lyandres, N. C. Shah, J. Zhao, R. P. Van Duyne in *Nanoscience and Technology: A Collection of Reviews from Nature Journals*, World Scientific, **2010**, pp. 308–319.
- [156] K. Raemdonck, J. Demeester, S. De Smedt, *Soft Matter* **2009**, *5*, 707–715.
- [157] P. K. Jain, X. Huang, I. H. El-Sayed, M. A. El-Sayed, *Accounts of chemical research* **2008**, *41*, 1578–1586.
- [158] M. R. Jones, K. D. Osberg, R. J. Macfarlane, M. R. Langille, C. A. Mirkin, *Chemical reviews* **2011**, *111*, 3736–3827.

- [159] M. Hu, J. Chen, Z.-Y. Li, L. Au, G. V. Hartland, X. Li, M. Marquez, Y. Xia, *Chemical Society Reviews* **2006**, *35*, 1084–1094.
- [160] M. B. Cortie, A. M. McDonagh, *Chemical reviews* **2011**, *111*, 3713–3735.
- [161] I. Freitag, C. Matthäus, A. Csaki, J. H. Clement, D. Cialla-May, K. Weber, C. Krafft, J. Popp, *Journal of biomedical optics* **2015**, *20*, 055002.
- [162] C.-J. Zhong, H.-y. Park, Core-shell nanoparticles with multiple cores and a method for fabricating them, US Patent 8,343,627, **2013**.
- [163] L. Gutiérrez, R. Costo, C. Grüttner, F. Westphal, N. Gehrke, D. Heinke, A. Fornara, Q. A. Pankhurst, C. Johansson, S. Veintemillas-Verdaguer, et al., *Dalton Transactions* **2015**, *44*, 2943–2952.
- [164] R. Bardhan, S. Mukherjee, N. A. Mirin, S. D. Levit, P. Nordlander, N. J. Halas, *The Journal of Physical Chemistry C* **2010**, *114*, 7378–7383.
- [165] H. Wang, D. W. Brandl, P. Nordlander, N. J. Halas, *Accounts of chemical research* **2007**, *40*, 53–62.
- [166] S. Wang, B. R. Jarrett, S. M. Kauzlarich, A. Y. Louie, *Journal of the American Chemical Society* **2007**, *129*, 3848–3856.
- [167] C. Radloff, N. J. Halas, *Nano letters* **2004**, *4*, 1323–1327.
- [168] J. Ye, B. Van de Broek, R. De Palma, W. Libaers, K. Clays, W. Van Roy, G. Borghs, G. Maes, *Colloids and Surfaces A: Physicochemical and Engineering Aspects* **2008**, *322*, 225–233.
- [169] S. Poovarodom, J. D. Bass, S.-J. Hwang, A. Katz, *Langmuir* **2005**, *21*, 12348–12356.
- [170] L. M. Liz-Marzán, M. Giersig, P. Mulvaney, *Langmuir* **1996**, *12*, 4329–4335.
- [171] Y. Qi, M. Chen, S. Liang, J. Zhao, W. Yang, *Colloids and Surfaces A: Physicochemical and Engineering Aspects* **2007**, *302*, 383–387.

- [172] Y. Qi, M. Chen, S. Liang, W. Yang, J. Zhao, *Applied Surface Science* **2008**, *254*, 1684–1690.
- [173] W. Fu, H. Yang, L. Chang, M. Li, H. Bala, Q. Yu, G. Zou, *Colloids and Surfaces A: Physicochemical and Engineering Aspects* **2005**, *262*, 71–75.
- [174] T. Li, J. Moon, A. A. Morrone, J. J. Mecholsky, D. R. Talham, J. H. Adair, *Langmuir* **1999**, *15*, 4328–4334.
- [175] X. Lu, G. Liang, Z. Sun, W. Zhang, *Materials Science and Engineering: B* **2005**, *117*, 147–152.
- [176] F. Mazaleyrat, M. Ammar, M. Lobue, J.-P. Bonnet, P. Audebert, G.-Y. Wang, Y. Champion, M. Hfÿtch, E. Snoeck, *Journal of alloys and compounds* **2009**, *483*, 473–478.
- [177] Z. Ma, D. Dosev, M. Nichkova, R. K. Dumas, S. J. Gee, B. D. Hammock, K. Liu, I. M. Kennedy, *Journal of magnetism and magnetic materials* **2009**, *321*, 1368–1371.
- [178] M. Kanehara, Y. Watanabe, T. Teranishi, *Journal of nanoscience and nanotechnology* **2009**, *9*, 673–675.
- [179] H. J. Cha, Y. H. Kim, H. G. Cha, Y. S. Kang, *Surface Review and Letters* **2007**, *14*, 693–696.
- [180] M. Ammar, F. Mazaleyrat, J.-P. Bonnet, P. Audebert, A. Brosseau, G. Wang, Y. Champion, *Nanotechnology* **2007**, *18*, 285606.
- [181] M. Alejandro-Arellano, T. Ung, Á. Blanco, P. Mulvaney, L. M. Liz-Marzán, *Pure and applied chemistry* **2000**, *72*, 257–267.
- [182] J. Lee, Y. Lee, J. K. Youn, H. B. Na, T. Yu, H. Kim, S.-M. Lee, Y.-M. Koo, J. H. Kwak, H. G. Park, et al., *Small* **2008**, *4*, 143–152.
- [183] Y.-H. Lien, T.-M. Wu, *Journal of colloid and interface science* **2008**, *326*, 517–521.

- [184] F. G. Aliev, M. A. Correa-Duarte, A. Mamedov, J. W. Ostrander, M. Giersig, L. M. Liz-Marzán, N. A. Kotov, *Advanced materials* **1999**, *11*, 1006–1010.
- [185] R. He, X. You, J. Shao, F. Gao, B. Pan, D. Cui, *Nanotechnology* **2007**, *18*, 315601.
- [186] S. Zhang, X. Li, *Powder technology* **2004**, *141*, 75–79.
- [187] M.-Q. Zhu, J. J. Han, A. D. Li, *Journal of nanoscience and nanotechnology* **2007**, *7*, 2343–2348.
- [188] A. L. Rogach, D. Nagesha, J. W. Ostrander, M. Giersig, N. A. Kotov, *Chemistry of Materials* **2000**, *12*, 2676–2685.
- [189] M. A. Correa-Duarte, M. Giersig, L. M. Liz-Marzán, *Chemical Physics Letters* **1998**, *286*, 497–501.
- [190] Y. Kobayashi, N. Shimizu, K. Misawa, M. Takeda, N. Ohuchi, A. Kasuya, M. Konno, *Surface Engineering* **2008**, *24*, 248–252.
- [191] B. Dong, L. Cao, G. Su, W. Liu, H. Qu, D. Jiang, *Journal of colloid and interface science* **2009**, *339*, 78–82.
- [192] S. Santra, R. Tapeç, N. Theodoropoulou, J. Dobson, A. Hebard, W. Tan, *Langmuir* **2001**, *17*, 2900–2906.
- [193] F. Bao, J.-F. Li, B. Ren, Jian-Lin Yao, R.-A. Gu, Z.-Q. Tian, *The Journal of Physical Chemistry C* **2008**, *112*, 345–350.
- [194] J.-W. Hu, J.-F. Li, B. Ren, D.-Y. Wu, S.-G. Sun, Z.-Q. Tian, *The Journal of Physical Chemistry C* **2007**, *111*, 1105–1112.
- [195] Z. Yang, Y. Li, Z. Li, D. Wu, J. Kang, H. Xu, M. Sun, *The Journal of chemical physics* **2009**, *130*, 234705.
- [196] J.-F. Li, Z.-L. Yang, B. Ren, G.-K. Liu, P.-P. Fang, Y.-X. Jiang, D.-Y. Wu, Z.-Q. Tian, *Langmuir* **2006**, *22*, 10372–10379.
- [197] S. Kumar, S. Zou, *Langmuir* **2007**, *23*, 7365–7371.

- [198] X.-B. Zhang, J.-M. Yan, S. Han, H. Shioyama, Q. Xu, *Journal of the American Chemical Society* **2009**, *131*, 2778–2779.
- [199] N. Zhang, Y. Gao, H. Zhang, X. Feng, H. Cai, Y. Liu, *Colloids and Surfaces B: Biointerfaces* **2010**, *81*, 537–543.
- [200] L. Feng, X. Wu, L. Ren, Y. Xiang, W. He, K. Zhang, W. Zhou, S. Xie, *Chemistry—A European Journal* **2008**, *14*, 9764–9771.
- [201] R. Zanella, A. Sandoval, P. Santiago, V. A. Basiuk, J. M. Saniger, *The Journal of Physical Chemistry B* **2006**, *110*, 8559–8565.
- [202] L. Wang, L. Wang, J. Luo, Q. Fan, M. Suzuki, I. S. Suzuki, M. H. Engelhard, Y. Lin, N. Kim, J. Q. Wang, et al., *The Journal of Physical Chemistry B* **2005**, *109*, 21593–21601.
- [203] C. L. Carnes, K. J. Klabunde, *Chemistry of materials* **2002**, *14*, 1806–1811.
- [204] S. Decker, K. J. Klabunde, *Journal of the American Chemical Society* **1996**, *118*, 12465–12466.
- [205] F. Caruso, *Advanced materials* **2001**, *13*, 11–22.
- [206] S. Phadtare, A. Kumar, V. Vinod, C. Dash, D. V. Palaskar, M. Rao, P. G. Shukla, S. Sivaram, M. Sastry, *Chemistry of materials* **2003**, *15*, 1944–1949.
- [207] P. V. Kamat, B. Shanghavi, *The Journal of Physical Chemistry B* **1997**, *101*, 7675–7679.
- [208] G. Ma, J. He, K. Rajiv, S. Tang, Y. Yang, M. Nogami, *Applied physics letters* **2004**, *84*, 4684–4686.
- [209] A. Mews, A. Eychmüller, M. Giersig, D. Schooss, H. Weller, *The Journal of Physical Chemistry* **1994**, *98*, 934–941.
- [210] S. Balakrishnan, M. J. Bonder, G. C. Hadjipanayis, *Journal of magnetism and magnetic materials* **2009**, *321*, 117–122.

- [211] S. Laurent, D. Forge, M. Port, A. Roch, C. Robic, L. Vander Elst, R. N. Muller, *Chemical reviews* **2008**, *108*, 2064–2110.
- [212] M.-J. Kim, Y.-H. Choa, D. H. Kim, K. H. Kim, *IEEE transactions on magnetics* **2009**, *45*, 2446–2449.
- [213] V. Salgueiriño-Maceira, M. A. Correa-Duarte, *Advanced Materials* **2007**, *19*, 4131–4144.
- [214] L. Qi, J. Ma, H. Cheng, Z. Zhao, *Colloids and Surfaces A: Physicochemical and Engineering Aspects* **1996**, *111*, 195–202.
- [215] A. Kortan, R. Hull, R. L. Opila, M. G. Bawendi, M. L. Steigerwald, P. Carroll, L. E. Brus, *Journal of the American Chemical Society* **1990**, *112*, 1327–1332.
- [216] P. Scodeller, V. Flexer, R. Szamocki, E. Calvo, N. Tognalli, H. Troiani, A. Fainstein, *Journal of the American Chemical Society* **2008**, *130*, 12690–12697.
- [217] N. Sounderya, Y. Zhang, *Recent Patents on Biomedical Engineering* **2008**, *1*, 34–42.
- [218] P. A. Dresco, V. S. Zaitsev, R. J. Gambino, B. Chu, *Langmuir* **1999**, *15*, 1945–1951.
- [219] L. Babes, B. Denizot, G. Tanguy, J. J. Le Jeune, P. Jallet, *Journal of colloid and interface science* **1999**, *212*, 474–482.
- [220] J. P. Zimmer, S.-W. Kim, S. Ohnishi, E. Tanaka, J. V. Frangioni, M. G. Bawendi, *Journal of the American Chemical Society* **2006**, *128*, 2526–2527.
- [221] B. Schreder, T. Schmidt, V. Ptatschek, L. Spanhel, A. Materny, W. Kiefer, *Journal of crystal growth* **2000**, *214*, 782–786.
- [222] A. K. Gupta, M. Gupta, *biomaterials* **2005**, *26*, 3995–4021.

- [223] F. De Menezes, A. Brasil Jr, W. Moreira, L. Barbosa, C. Cesar, R. d. C. Ferreira, P. De Farias, B. Santos, *Microelectronics Journal* **2005**, *36*, 989–991.
- [224] P. De Farias, B. Santos, F. Menezes, A. Brasil Jr, R. Ferreira, M. Motta, A. Castro-Neto, A. Vieira, D. Silva, A. Fontes, et al., *Applied Physics A* **2007**, *89*, 957–961.
- [225] E. Yan, Y. Ding, C. Chen, R. Li, Y. Hu, X. Jiang, *Chemical Communications* **2009**, 2718–2720.
- [226] M. De, P. S. Ghosh, V. M. Rotello, *Advanced Materials* **2008**, *20*, 4225–4241.
- [227] X. Michalet, F. F. Pinaud, L. A. Bentolila, J. M. Tsay, S. Doose, J. J. Li, G. Sundaresan, A. Wu, S. Gambhir, S. Weiss, *science* **2005**, *307*, 538–544.
- [228] J. K. Jaiswal, H. Mattoussi, J. M. Mauro, S. M. Simon, *Nature biotechnology* **2003**, *21*, 47–51.
- [229] A. Radi, D. Pradhan, Y. Sohn, K. Leung, *ACS nano* **2010**, *4*, 1553–1560.
- [230] W. Han, L. Yi, N. Zhao, A. Tang, M. Gao, Z. Tang, *Journal of the American Chemical Society* **2008**, *130*, 13152–13161.
- [231] C.-C. Huang, Z. Yang, H.-T. Chang, *Langmuir* **2004**, *20*, 6089–6092.
- [232] L. Gou, C. J. Murphy, *Nano Letters* **2003**, *3*, 231–234.
- [233] X. Wang, T. Yang, K. Jiao, *Biosensors and Bioelectronics* **2009**, *25*, 668–673.
- [234] Y. Wu, P. Jiang, M. Jiang, *Nanotechnology* **2009**, *20*, 10.
- [235] M. Min, C. Kim, H. Lee, *Journal of Molecular Catalysis A: Chemical* **2010**, *333*, 6–10.
- [236] Z. Libor, Q. Zhang, *Materials Chemistry and Physics* **2009**, *114*, 902–907.
- [237] Y. Qu, R. Cheng, Q. Su, X. Duan, *Journal of the American Chemical Society* **2011**, *133*, 16730–16733.

- [238] B. Törngren, K. Akitsu, A. Ylinen, S. Sandén, H. Jiang, J. Ruokolainen, M. Komatsu, T. Hamamura, J. Nakazaki, T. Kubo, et al., *Journal of colloid and interface science* **2014**, *427*, 54–61.
- [239] P. Yu, Y. Yao, J. Wu, X. Niu, A. L. Rogach, Z. Wang, *Scientific reports* **2017**, *7*, 1–10.
- [240] M. Wang, X. Pang, D. Zheng, Y. He, L. Sun, C. Lin, Z. Lin, *Journal of Materials Chemistry A* **2016**, *4*, 7190–7199.
- [241] J. Li, S. K. Cushing, J. Bright, F. Meng, T. R. Senty, P. Zheng, A. D. Bristow, N. Wu, *Acs Catalysis* **2013**, *3*, 47–51.
- [242] T. Ghodselahi, H. Zahrabi, M. H. Saani, M. Vesaghi, *The Journal of Physical Chemistry C* **2011**, *115*, 22126–22130.
- [243] M. Navas, R. Soni, *Plasmonics* **2015**, *10*, 681–690.
- [244] T.-H. Chen, R.-D. Jean, K.-C. Chiu, C.-H. Chen, D.-M. Liu, *Applied Physics Letters* **2012**, *100*, 223101.
- [245] A. Steinbrück, O. Stranik, A. Csaki, W. Fritzsche, *Analytical and bioanalytical chemistry* **2011**, *401*, 1241.
- [246] Q. Tian, J. Hu, Y. Zhu, R. Zou, Z. Chen, S. Yang, R. Li, Q. Su, Y. Han, X. Liu, *Journal of the American Chemical Society* **2013**, *135*, 8571–8577.
- [247] B. Xu, Y. Ju, Y. Cui, G. Song, Y. Iwase, A. Hosoi, Y. Morita, *Langmuir* **2014**, *30*, 7789–7797.
- [248] Z. Zhou, Y. Sun, J. Shen, J. Wei, C. Yu, B. Kong, W. Liu, H. Yang, S. Yang, W. Wang, *Biomaterials* **2014**, *35*, 7470–7478.
- [249] L. P. Qian, L. H. Zhou, H.-P. Too, G.-M. Chow, *Journal of Nanoparticle Research* **2011**, *13*, 499–510.
- [250] P. Yuan, Y. H. Lee, M. K. Gnanasammandhan, Z. Guan, Y. Zhang, Q.-H. Xu, *Nanoscale* **2012**, *4*, 5132–5137.

- [251] M. Kumagai, T. K. Sarma, H. Cabral, S. Kaida, M. Sekino, N. Herlambang, K. Osada, M. R. Kano, N. Nishiyama, K. Kataoka, *Macromolecular rapid communications* **2010**, *31*, 1521–1528.
- [252] J. E. Wijnhoven, W. L. Vos, *Science* **1998**, *281*, 802–804.
- [253] T. Sugama, B. Lipford, *Journal of materials science* **1997**, *32*, 3523–3534.
- [254] D. Zhao, J. Feng, Q. Huo, N. Melosh, G. H. Fredrickson, B. F. Chmelka, G. D. Stucky, *science* **1998**, *279*, 548–552.
- [255] K. Sakanishi, H.-u. Hasuo, M. Kishino, I. Mochida, O. Okuma, *Energy & fuels* **1996**, *10*, 216–219.
- [256] J. P. Ansermet, E. Baeriswyl, *Journal of materials science* **1994**, *29*, 2841–2846.
- [257] J. Hu, M. Chen, X. Fang, L. Wu, *Chemical Society Reviews* **2011**, *40*, 5472–5491.
- [258] J. Liu, S. Z. Qiao, S. Budi Hartono, G. Q. Lu, *Angewandte Chemie International Edition* **2010**, *49*, 4981–4985.
- [259] F. Zhang, N. Wu, J. Zhu, J. Zhao, G.-j. Weng, J.-j. Li, J.-w. Zhao, *Sensors and Actuators B: Chemical* **2018**, *271*, 174–182.
- [260] J. Zhu, N. Wu, F. Zhang, X. Li, J. Li, J. Zhao, *Spectrochimica Acta Part A: Molecular and Biomolecular Spectroscopy* **2018**, *204*, 754–762.
- [261] X. W. Lou, L. A. Archer, Z. Yang, *Advanced Materials* **2008**, *20*, 3987–4019.
- [262] A. Cao, R. Lu, G. Veser, *Physical Chemistry Chemical Physics* **2010**, *12*, 13499–13510.
- [263] Q. Zhang, W. Wang, J. Goebel, Y. Yin, *Nano Today* **2009**, *4*, 494–507.
- [264] J. C. Park, H. Song, *Nano Research* **2011**, *4*, 33–49.
- [265] J. Liu, S. Z. Qiao, Q. H. Hu, G. Q. Lu, *Small* **2011**, *7*, 425–443.

- [266] Y. Zhao, L. Jiang, *Advanced Materials* **2009**, *21*, 3621–3638.
- [267] Y. Sun, B. Mayers, Y. Xia, *Advanced Materials* **2003**, *15*, 641–646.
- [268] Y. Yin, R. M. Rioux, C. K. Erdonmez, S. Hughes, G. A. Somorjai, A. P. Alivisatos, *Science* **2004**, *304*, 711–714.
- [269] A. G. da Silva, T. S. Rodrigues, S. J. Haigh, P. H. Camargo, *Chemical Communications* **2017**, *53*, 7135–7148.
- [270] X. Xia, Y. Wang, A. Ruditskiy, Y. Xia, *Advanced Materials* **2013**, *25*, 6313–6333.
- [271] Y. Sun, Y. Xia, *Journal of the American Chemical Society* **2004**, *126*, 3892–3901.
- [272] G. Aragay, F. Pino, A. Merkoçi, *Chemical reviews* **2012**, *112*, 5317–5338.
- [273] R. M. Crooks, M. Zhao, L. Sun, V. Chechik, L. K. Yeung, *Accounts of chemical research* **2001**, *34*, 181–190.
- [274] D. Astruc, F. Lu, J. R. Aranzaes, *Angewandte Chemie International Edition* **2005**, *44*, 7852–7872.
- [275] S. H. Joo, S. J. Choi, I. Oh, J. Kwak, Z. Liu, O. Terasaki, R. Ryoo, *Nature* **2001**, *412*, 169–172.
- [276] M. I. Stockman, *Physical review letters* **2004**, *93*, 137404.
- [277] J. L. West, N. J. Halas, *Annual review of biomedical engineering* **2003**, *5*, 285–292.
- [278] U. Simon, G. Schön in *Handbook of nanostructured materials and nanotechnology*, Elsevier, **2000**, pp. 131–178.
- [279] G. Schön, U. Simon, *Colloid and Polymer Science* **1995**, *273*, 202–218.
- [280] T. Nann in First International IEEE Conference on Polymers and Adhesives in Microelectronics and Photonics. Incorporating POLY, PEP & Adhesives in Electronics. Proceedings (Cat. No. 01TH8592), IEEE, **2001**, pp. 49–53.

- [281] R. Cauchois, M. Saadaoui, A. Yakoub, K. Inal, B. Dubois-Bonvalot, J.-C. Fidalgo in, **2011**.
- [282] P. K. Jain, K. S. Lee, I. H. El-Sayed, M. A. El-Sayed, *The journal of physical chemistry B* **2006**, *110*, 7238–7248.
- [283] D. W. Grainger, D. G. Castner, *Advanced Materials* **2008**, *20*, 867–877.
- [284] M. Singh, S. Manikandan, A. Kumaraguru, *Research Journal of Nanoscience and Nanotechnology* **2011**, *1*, 1–11.
- [285] U. Phromsuwan, C. Sirisathitkul, Y. Sirisathitkul, B. Uyyanonvara, P. Muneesawang, *Journal of Magnetism* **2013**, *18*, 311–316.
- [286] W. Voit, W. Zapka, L. Belova, K. Rao, *IEE Proceedings-Science Measurement and Technology* **2003**, *150*, 252–256.
- [287] B. Tian, X. Zheng, T. J. Kempa, Y. Fang, N. Yu, G. Yu, J. Huang, C. M. Lieber, *nature* **2007**, *449*, 885–889.
- [288] M. Grätzel, *Journal of photochemistry and photobiology C: Photochemistry Reviews* **2003**, *4*, 145–153.
- [289] B. Nowack, T. D. Bucheli, *Environmental pollution* **2007**, *150*, 5–22.
- [290] S. J. Klaine, P. J. Alvarez, G. E. Batley, T. F. Fernandes, R. D. Handy, D. Y. Lyon, S. Mahendra, M. J. McLaughlin, J. R. Lead, *Environmental Toxicology and Chemistry: An International Journal* **2008**, *27*, 1825–1851.
- [291] W.-x. Zhang, *Journal of nanoparticle Research* **2003**, *5*, 323–332.
- [292] E. Prodan, C. Radloff, N. J. Halas, P. Nordlander, *science* **2003**, *302*, 419–422.
- [293] P. V. Kamat, Photophysical, photochemical and photocatalytic aspects of metal nanoparticles, **2002**.
- [294] R. L. McCreery, *Raman spectroscopy for chemical analysis, Vol. 225*, John Wiley & Sons, **2005**.

- [295] B. Pettinger, Adsorption at Electrode Surface, **1992**.
- [296] M. G. Albrecht, J. A. Creighton, *Journal of the american chemical society* **1977**, *99*, 5215–5217.
- [297] D. L. Jeanmaire, R. P. Van Duyne, *Journal of electroanalytical chemistry and interfacial electrochemistry* **1977**, *84*, 1–20.
- [298] M. Moskovits, *Reviews of modern physics* **1985**, *57*, 783.
- [299] A. Campion, P. Kambhampati, *Chemical society reviews* **1998**, *27*, 241–250.
- [300] A. Otto, I. Mrozek, H. Grabhorn, W. Akemann, *Journal of Physics: Condensed Matter* **1992**, *4*, 1143.
- [301] M. Moskovits, *The Journal of Chemical Physics* **1978**, *69*, 4159–4161.
- [302] S. Nie, S. R. Emory, *science* **1997**, *275*, 1102–1106.
- [303] M. D. Sonntag, J. M. Klingsporn, A. B. Zrimsek, B. Sharma, L. K. Ruvuna, R. P. Van Duyne, *Chemical Society Reviews* **2014**, *43*, 1230–1247.
- [304] K. Kneipp, Y. Wang, H. Kneipp, L. T. Perelman, I. Itzkan, R. R. Dasari, M. S. Feld, *Physical review letters* **1997**, *78*, 1667.
- [305] S. Pande, S. K. Ghosh, S. Praharaj, S. Panigrahi, S. Basu, S. Jana, A. Pal, T. Tsukuda, T. Pal, *The Journal of Physical Chemistry C* **2007**, *111*, 10806–10813.
- [306] B. Rodriguez-González, A. Burrows, M. Watanabe, C. J. Kiely, L. M. L. Marzán, *Journal of Materials Chemistry* **2005**, *15*, 1755–1759.
- [307] R. Jiang, H. Chen, L. Shao, Q. Li, J. Wang, *Advanced Materials* **2012**, *24*, OP200–OP207.
- [308] G. P. Kumar, S. Shruthi, B. Vibha, B. A. Reddy, T. K. Kundu, C. Narayana, *The Journal of Physical Chemistry C* **2007**, *111*, 4388–4392.
- [309] L. Song, K. Mao, X. Zhou, J. Hu, *Talanta* **2016**, *146*, 285–290.

- [310] W. Shen, X. Lin, C. Jiang, C. Li, H. Lin, J. Huang, S. Wang, G. Liu, X. Yan, Q. Zhong, et al., *Angewandte Chemie International Edition* **2015**, *54*, 7308–7312.
- [311] B. S. Galabov, T. Dudev, *Vibrational intensities*, Elsevier, **1996**.
- [312] M. Kerker, D.-S. Wang, H. Chew, *Applied optics* **1980**, *19*, 4159–4174.
- [313] S.-Y. Ding, J. Yi, J.-F. Li, B. Ren, D.-Y. Wu, R. Panneerselvam, Z.-Q. Tian, *Nature Reviews Materials* **2016**, *1*, 1–16.
- [314] R. Rojas, F. Claro, *The Journal of chemical physics* **1993**, *98*, 998–1006.
- [315] G. V. Naik, V. M. Shalaev, A. Boltasseva, *Advanced Materials* **2013**, *25*, 3264–3294.
- [316] A. Boltasseva, H. A. Atwater, *Science* **2011**, *331*, 290–291.
- [317] K. A. Willets, R. P. Van Duyne, *Annu. Rev. Phys. Chem.* **2007**, *58*, 267–297.
- [318] P. Johnson, R. Christy, *Physical review B* **1974**, *9*, 5056.
- [319] P. B. Johnson, R.-W. Christy, *Physical review B* **1972**, *6*, 4370.
- [320] E. D. Palik, *Handbook of optical constants of solids, Vol. 3*, Academic press, **1998**.
- [321] S. A. Maier, *Plasmonics: fundamentals and applications*, Springer Science & Business Media, **2007**.
- [322] K. Kosuda, J. Bingham, K. Wustholz, R. Van Duyne, *Andrews D* **2011**, 263–301.
- [323] P. L. Stiles, J. A. Dieringer, N. C. Shah, R. P. Van Duyne, *Annu. Rev. Anal. Chem.* **2008**, *1*, 601–626.
- [324] H. Raether in *Surface plasmons on smooth and rough surfaces and on gratings*, Springer, **1988**, pp. 4–39.
- [325] A. Vivoni, R. L. Birke, R. Foucault, J. R. Lombardi, *The Journal of Physical Chemistry B* **2003**, *107*, 5547–5557.

- [326] Z. Q. Tian, *Faraday Discuss.* **2006**, *132*, 309–319.
- [327] D.-Y. Wu, B. Ren, Y.-X. Jiang, X. Xu, Z.-Q. Tian, *The Journal of Physical Chemistry A* **2002**, *106*, 9042–9052.
- [328] D. Roy, T. Furtak, *The Journal of chemical physics* **1984**, *81*, 4168–4175.
- [329] D. W. Silverstein, L. Jensen, *The Journal of chemical physics* **2012**, *136*, 064111.
- [330] L. Zhao, L. Jensen, G. C. Schatz, *Journal of the American chemical society* **2006**, *128*, 2911–2919.
- [331] D. Wu, M. Hayashi, S. Lin, Z. Tian, *Spectrochimica Acta Part A: Molecular and Biomolecular Spectroscopy* **2004**, *60*, 137–146.
- [332] D.-Y. Wu, X.-M. Liu, S. Duan, X. Xu, B. Ren, S.-H. Lin, Z.-Q. Tian, *The Journal of Physical Chemistry C* **2008**, *112*, 4195–4204.
- [333] J. F. Arenas, J. Soto, I. L. Tocón, D. J. Fernández, J. C. Otero, J. I. Marcos, *The Journal of chemical physics* **2002**, *116*, 7207–7216.
- [334] J. F. Arenas, M. S. Woolley, J. C. Otero, J. I. Marcos, *The Journal of Physical Chemistry* **1996**, *100*, 3199–3206.
- [335] J. R. Lombardi, R. L. Birke, *The Journal of chemical physics* **2007**, *126*, 244709.
- [336] J. L. Payton, S. M. Morton, J. E. Moore, L. Jensen, *Accounts of chemical research* **2014**, *47*, 88–99.
- [337] J. R. Lombardi, R. L. Birke, T. Lu, J. Xu, *The Journal of chemical physics* **1986**, *84*, 4174–4180.
- [338] S.-Y. Ding, B.-J. Liu, Q.-N. Jiang, D.-Y. Wu, B. Ren, X. Xu, Z.-Q. Tian, *Chemical Communications* **2012**, *48*, 4962–4964.
- [339] J.-F. Li, Y.-F. Huang, S. Duan, R. Pang, D.-Y. Wu, B. Ren, X. Xu, Z.-Q. Tian, *Physical Chemistry Chemical Physics* **2010**, *12*, 2493–2502.

- [340] H. Yui, *Analytical and bioanalytical chemistry* **2010**, *397*, 1181–1190.
- [341] Z. Liu, S.-Y. Ding, Z.-B. Chen, X. Wang, J.-H. Tian, J. R. Anema, X.-S. Zhou, D.-Y. Wu, B.-W. Mao, X. Xu, et al., *Nature communications* **2011**, *2*, 1–6.
- [342] M. Galperin, M. A. Ratner, A. Nitzan, *The Journal of chemical physics* **2009**, *130*, 144109.
- [343] R. Matsushita, M. Kiguchi, *Physical Chemistry Chemical Physics* **2015**, *17*, 21254–21260.
- [344] T. Bora, *Noble and Precious Metals-Properties Nanoscale Effects and Applications* **2018**.
- [345] E. Le Ru, E. Blackie, M. Meyer, P. G. Etchegoin, *The Journal of Physical Chemistry C* **2007**, *111*, 13794–13803.
- [346] L. Vigdeman, E. R. Zubarev, *Chemistry of Materials* **2013**, *25*, 1450–1457.
- [347] E. Ringe, J. Zhang, M. R. Langille, K. Sohn, C. Cobley, L. Au, Y. Xia, C. A. Mirkin, J. Huang, L. D. Marks, et al., *MRS Online Proceedings Library Archive* **2009**, *1208*.
- [348] T. El-Brolosy, T. Abdallah, M. B. Mohamed, S. Abdallah, K. Easawi, S. Negm, H. Talaat, *The European Physical Journal Special Topics* **2008**, *153*, 361–364.
- [349] C. J. Orendorff, L. Gearheart, N. R. Jana, C. J. Murphy, *Physical Chemistry Chemical Physics* **2006**, *8*, 165–170.
- [350] B. F. Leo, S. Chen, Y. Kyo, K.-L. Herpoldt, N. J. Terrill, I. E. Dunlop, D. S. McPhail, M. S. Shaffer, S. Schwander, A. Gow, et al., *Environmental science & technology* **2013**, *47*, 11232–11240.
- [351] A. K. Samal, L. Polavarapu, S. Rodal-Cedeira, L. M. Liz-Marzán, J. Pérez-Juste, I. Pastoriza-Santos, *Langmuir* **2013**, *29*, 15076–15082.

- [352] Y. Yang, J. Liu, Z.-W. Fu, D. Qin, *Journal of the American Chemical Society* **2014**, *136*, 8153–8156.
- [353] J. Jackson, S. Westcott, L. Hirsch, J. West, N. Halas, *Applied Physics Letters* **2003**, *82*, 257–259.
- [354] L. Lu, G. Burkey, I. Halaciuga, D. V. Goia, *Journal of colloid and interface science* **2013**, *392*, 90–95.
- [355] K.-i. Yoshida, T. Itoh, H. Tamaru, V. Biju, M. Ishikawa, Y. Ozaki, *Physical Review B* **2010**, *81*, 115406.
- [356] L. K. Ausman, G. C. Schatz, *The Journal of chemical physics* **2009**, *131*, 084708.
- [357] E. Le Ru, P. Etchegoin, *Chemical Physics Letters* **2006**, *423*, 63–66.
- [358] E. Le Ru, P. Etchegoin, *Principles of Surface-Enhanced Raman Spectroscopy: and related plasmonic effects*, Elsevier, **2008**.
- [359] E. Le Ru, P. Etchegoin, M. Meyer, *The Journal of chemical physics* **2006**, *125*, 204701.
- [360] A. Nitzan, L. Brus, *The Journal of Chemical Physics* **1981**, *75*, 2205–2214.
- [361] R. Zhang, Y. Zhang, Z. Dong, S. Jiang, C. Zhang, L. Chen, L. Zhang, Y. Liao, J. Aizpurua, Y. e. Luo, et al., *Nature* **2013**, *498*, 82–86.
- [362] A. Shiohara, Y. Wang, L. M. Liz-Marzán, *Journal of Photochemistry and Photobiology C: Photochemistry Reviews* **2014**, *21*, 2–25.
- [363] P. Aravind, H. Metiu, *Surface science* **1983**, *124*, 506–528.
- [364] J. M. McMahon, S. Li, L. K. Ausman, G. C. Schatz, *The Journal of Physical Chemistry C* **2012**, *116*, 1627–1637.
- [365] H. Wei, H. Xu, *Nanoscale* **2013**, *5*, 10794–10805.
- [366] V. M. Shalaev, A. K. Sarychev, *Physical Review B* **1998**, *57*, 13265.

- [367] A. Moreau, C. Cirac, J. J. Mock, R. T. Hill, Q. Wang, B. J. Wiley, A. Chilkoti, D. R. Smith, *Nature* **2012**, *492*, 86–89.
- [368] S. L. Kleinman, R. R. Frontiera, A.-I. Henry, J. A. Dieringer, R. P. Van Duyne, *Physical Chemistry Chemical Physics* **2013**, *15*, 21–36.
- [369] H. Ko, S. Singamaneni, V. V. Tsukruk, *Small* **2008**, *4*, 1576–1599.
- [370] Z. Zhu, H. Meng, W. Liu, X. Liu, J. Gong, X. Qiu, L. Jiang, D. Wang, Z. Tang, *Angewandte Chemie International Edition* **2011**, *50*, 1593–1596.
- [371] P. Estrela, N. Bhalla, P. Jolly, N. Formisano, P. Estrela, *Essays in Biochemistry* **2016**, *60*, 1–8.
- [372] B. R. Eggins, *An Introduction to Biosensors*, John Wiley, **1996**.
- [373] E.-H. Yoo, S.-Y. Lee, *Sensors* **2010**, *10*, 4558–4576.
- [374] G. S. Nunes, J.-L. Marty in *Immobilization of Enzymes and Cells*, Springer, **2006**, pp. 239–250.
- [375] B. J. Sanghavi, O. S. Wolfbeis, T. Hirsch, N. S. Swami, *Microchimica Acta* **2015**, *182*, 1–41.
- [376] H. Freiser, *Ion-selective electrodes in analytical chemistry*, Springer Science & Business Media, **2012**.
- [377] E. Honarmand, M. H. Motaghedifard, M. Ghamari, *RSC advances* **2014**, *4*, 35511–35521.
- [378] H. Maaoui, F. Teodoresu, Q. Wang, G.-H. Pan, A. Addad, R. Chtourou, S. Szunerits, R. Boukherroub, *Sensors* **2016**, *16*, 1720.
- [379] W. Liu, H. Zhang, B. Yang, Z. Li, L. Lei, X. Zhang, *Journal of Electroanalytical Chemistry* **2015**, *749*, 62–67.
- [380] D. B. Rao, *Electrochemistry for environmental protection*, Discovery Publishing House, **2001**.
- [381] G. Henrion, *Zeitschrift für Chemie* **1987**, *27*, 384–384.

- [382] J.-H. Lee, K. J. Gibson, G. Chen, Y. Weizmann, *Nature communications* **2015**, *6*, 7571.
- [383] X. Zhuo, X. Zhu, Q. Li, Z. Yang, J. Wang, *ACS nano* **2015**, *9*, 7523–7535.
- [384] K. Park, H. Koerner, R. A. Vaia, *Nano letters* **2010**, *10*, 1433–1439.
- [385] B. P. Khanal, E. R. Zubarev, *Journal of the American Chemical Society* **2008**, *130*, 12634–12635.
- [386] Q. Li, X. Zhuo, S. Li, Q. Ruan, Q.-H. Xu, J. Wang, *Advanced Optical Materials* **2015**, *3*, 801–812.
- [387] N. R. Jana, L. Gearheart, C. J. Murphy, *Chemical Communications-Cambridge* **2001**, 617–618.
- [388] Q. Zhang, N. Large, H. Wang, *ACS applied materials & interfaces* **2014**, *6*, 17255–17267.
- [389] J. E. Millstone, S. Park, K. L. Shuford, L. Qin, G. C. Schatz, C. A. Mirkin, *Journal of the American Chemical Society* **2005**, *127*, 5312–5313.
- [390] J. Zhang, C. Feng, Y. Deng, L. Liu, Y. Wu, B. Shen, C. Zhong, W. Hu, *Chemistry of Materials* **2014**, *26*, 1213–1218.
- [391] C. Crowell, *Solid-State Electronics* **1965**, *8*, 395–399.
- [392] D. Mihalcea, P. Piot, et al., *Proceedings of LINAC08 Victoria Canada* **2008**, *TUP106*, 652–654.
- [393] E. Smith, G. Dent, *Modern Raman spectroscopy: a practical approach*, John Wiley & Sons, **2019**.
- [394] J. Stock, M. Orna, *Electrochemistry: past and present*, American Chemical Society, **1989**.
- [395] M. Tsuji, N. Miyamae, S. Lim, K. Kimura, X. Zhang, S. Hikino, M. Nishio, *Crystal growth & design* **2006**, *6*, 1801–1807.
- [396] K. M. Mayer, J. H. Hafner, *Chemical reviews* **2011**, *111*, 3828–3857.

- [397] N. J. Halas, S. Lal, W.-S. Chang, S. Link, P. Nordlander, *Chemical reviews* **2011**, *111*, 3913–3961.
- [398] V. Amendola, R. Pilot, M. Frascioni, O. M. Maragò, M. A. Iat, *Journal of Physics: Condensed Matter* **2017**, *29*, 203002.
- [399] E. Petryayeva, U. J. Krull, *Analytica chimica acta* **2011**, *706*, 8–24.
- [400] K. A. Willets, *Progress in surface science* **2012**, *87*, 209–220.
- [401] M. Liu, P. Guyot-Sionnest, *The Journal of Physical Chemistry B* **2004**, *108*, 5882–5888.
- [402] M. M. Treacy, *Microscopy and Microanalysis* **2011**, *17*, 847–858.
- [403] S. Ristig, O. Prymak, K. Loza, M. Gocyla, W. Meyer-Zaika, M. Heggen, D. Raabe, M. Epple, *Journal of Materials Chemistry B* **2015**, *3*, 4654–4662.
- [404] M. Van Hove, G. Somorjai, *Surface Science* **1980**, *92*, 489–518.
- [405] R. Jin, Y. C. Cao, E. Hao, G. S. Métraux, G. C. Schatz, C. A. Mirkin, *Nature* **2003**, *425*, 487–490.
- [406] J. Zeng, Y. Zheng, M. Rycenga, J. Tao, Z.-Y. Li, Q. Zhang, Y. Zhu, Y. Xia, *Journal of the American Chemical Society* **2010**, *132*, 8552–8553.
- [407] A. Adamson, *A Textbook of Physical Chemistry*, 3rd ed., Academic Press, Orlando, **1986**.
- [408] Y. Ma, W. Li, E. C. Cho, Z. Li, T. Yu, J. Zeng, Z. Xie, Y. Xia, *ACS nano* **2010**, *4*, 6725–6734.
- [409] S.-W. Lee, S.-H. Chang, Y.-S. Lai, C.-C. Lin, C.-M. Tsai, Y.-C. Lee, J.-C. Chen, C.-L. Huang, *Materials* **2014**, *7*, 7781–7798.
- [410] T. Ghosh, B. Satpati, *The Journal of Physical Chemistry C* **2013**, *117*, 10825–10833.
- [411] C. S. Kumar, *UV-VIS and photoluminescence spectroscopy for nanomaterials characterization*, Springer, **2013**.

- [412] G. Wiederrecht, *Handbook of nanoscale optics and electronics*, Academic Press, **2010**.
- [413] Q. Abbas, *Journal of Nanomaterials & Molecular Nanotechnology* **2019**, *8*, 1000268.
- [414] G. Keresztury, J. Chalmers, P. Griffith, *Raman Spectroscopy: Theory in Handbook of Vibrational Spectroscopy*, vol. 1, **2002**.
- [415] M. Fleischmann, P. Hendra, A. McQuillan, *Chemical physics letters* **1974**, *26*.
- [416] Y. Song, T. Miao, P. Zhang, C. Bi, H. Xia, D. Wang, X. Tao, *Nanoscale* **2015**, *7*, 8405–8415.
- [417] S. P. Hastings, P. Swanglap, Z. Qian, Y. Fang, S.-J. Park, S. Link, N. Engheta, Z. Fakhraai, *ACS nano* **2014**, *8*, 9025–9034.
- [418] E. Nalbant Esenturk, A. Hight Walker, *Journal of Raman Spectroscopy: An International Journal for Original Work in all Aspects of Raman Spectroscopy Including Higher Order Processes and also Brillouin and Rayleigh Scattering* **2009**, *40*, 86–91.
- [419] G. M. Hale, M. R. Querry, *Applied optics* **1973**, *12*, 555–563.
- [420] Y. Sun, Y. Yin, B. T. Mayers, T. Herricks, Y. Xia, *Chemistry of Materials* **2002**, *14*, 4736–4745.
- [421] R. Gans, *Annalen der Physik* **1912**, *342*, 881–900.
- [422] S. Eustis, M. A. El-Sayed, *Journal of Applied Physics* **2006**, *100*, 044324.
- [423] H. Wang, N. J. Halas, *Advanced Materials* **2008**, *20*, 820–825.
- [424] M. Noginov, G. Zhu, V. Gavrilenko, *Optics express* **2007**, *15*, 15648–15655.
- [425] J. Renger, S. Grafström, L. M. Eng, V. Deckert, *JOSA A* **2004**, *21*, 1362–1367.

- [426] W.-q. Ma, Y. Fang, G.-l. Hao, W.-g. Wang, *Chinese Journal of Chemical Physics* **2010**, *23*, 659–663.
- [427] T. Bürgi, *Nanoscale* **2015**, *7*, 15553–15567.
- [428] I. Persaud, W. E. Grossman, *Journal of Raman spectroscopy* **1993**, *24*, 107–112.
- [429] J. Hu, B. Zhao, W. Xu, B. Li, Y. Fan, *Spectrochimica Acta Part A: Molecular and Biomolecular Spectroscopy* **2002**, *58*, 2827–2834.
- [430] R. Li, H. Li, S. Pan, K. Liu, S. Hu, L. Pan, Y. Guo, S. Wu, X. Li, J. Liu, *Journal of Materials Research* **2013**, *28*, 3401–3407.
- [431] A. Maity, A. Maiti, B. Satpati, A. Patsha, S. Dhara, T. K. Chini, *The Journal of Physical Chemistry C* **2016**, *120*, 27003–27012.
- [432] C. Zhu, G. Meng, P. Zheng, Q. Huang, Z. Li, X. Hu, X. Wang, Z. Huang, F. Li, N. Wu, *Advanced Materials* **2016**, *28*, 4871–4876.
- [433] C. Zhu, G. Meng, Q. Huang, X. Wang, Y. Qian, X. Hu, H. Tang, N. Wu, *Nano Research* **2015**, *8*, 957–966.
- [434] C. Kong, J. Lv, S. Sun, X. Song, Z. Yang, *RSC Advances* **2014**, *4*, 27074–27077.
- [435] C. J. Murphy, A. M. Gole, S. E. Hunyadi, J. W. Stone, P. N. Sisco, A. Alkilany, B. E. Kinard, P. Hankins, *Chemical Communications* **2008**, 544–557.
- [436] A. Kudelski, *Chemical Physics Letters* **2005**, *414*, 271–275.
- [437] W. Song, W. Li, Y. Cheng, H. Jia, G. Zhao, Y. Zhou, B. Yang, W. Xu, W. Tian, B. Zhao, *Journal of Raman Spectroscopy: An International Journal for Original Work in all Aspects of Raman Spectroscopy Including Higher Order Processes and also Brillouin and Rayleigh Scattering* **2006**, *37*, 755–761.

- [438] D. Lee, S. Yoon, *The Journal of Physical Chemistry C* **2016**, *120*, 20642–20650.
- [439] X. Dong, J. Zhou, X. Liu, D. Lin, L. Zha, *Journal of Raman Spectroscopy* **2014**, *45*, 431–437.
- [440] Z. A. Nima, Y. R. Davletshin, F. Watanabe, K. M. Alghazali, J. C. Kumaradas, A. S. Biris, *RSC advances* **2017**, *7*, 53164–53171.
- [441] S. Kishore, J. Nelson, J. H. Adair, P. Eklund, *Journal of Alloys and Compounds* **2005**, *389*, 234–242.
- [442] A. Klinkova, P. De Luna, C.-T. Dinh, O. Voznyy, E. M. Larin, E. Kumacheva, E. H. Sargent, *Acs Catalysis* **2016**, *6*, 8115–8120.
- [443] Y. Sun, Z. Tao, J. Chen, T. Herricks, Y. Xia, *Journal of the American Chemical Society* **2004**, *126*, 5940–5941.
- [444] J. Gao, Z. Tian, *Spectrochimica Acta part A: Molecular and Biomolecular Spectroscopy* **1997**, *53*, 1595–1600.
- [445] J.-W. Hu, Y. Zhang, J.-F. Li, Z. Liu, B. Ren, S.-G. Sun, Z.-Q. Tian, T. Lian, *Chemical Physics Letters* **2005**, *408*, 354–359.
- [446] A. J. Bard, L. R. Faulkner, J. Leddy, C. G. Zoski, *Electrochemical methods: fundamentals and applications, Vol. 2*, Wiley New York, **1980**.
- [447] P. Zanello, C. Nervi, F. F. De Biani, *Inorganic electrochemistry: theory, practice and application*, Royal Society of Chemistry, **2011**.
- [448] F. G. Cottrell, *Zeitschrift für Physikalische Chemie* **1903**, *42*, 385–431.
- [449] X. Cai, K. Kalcher, C. Neuhold, B. Ogorevc, *Talanta* **1994**, *41*, 407–413.
- [450] K.-C. Lin, H. Lin, P. Chou, *The Journal of rheumatology* **2000**, *27*, 1501–1505.

- [451] R. J. Johnson, D.-H. Kang, D. Feig, S. Kivlighn, J. Kanellis, S. Watanabe, K. R. Tuttle, B. Rodriguez-Iturbe, J. Herrera-Acosta, M. Mazzali, *Hypertension* **2003**, *41*, 1183–1190.
- [452] B. A. Eipper, R. E. Mains, C. C. Glembotski, *Proceedings of the National Academy of Sciences* **1983**, *80*, 5144–5148.
- [453] A. C. Carr, S. Maggini, *Nutrients* **2017**, *9*, 1211.
- [454] J. Du, J. J. Cullen, G. R. Buettner, *Biochimica et Biophysica Acta (BBA)-Reviews on Cancer* **2012**, *1826*, 443–457.
- [455] A. Montel-Hagen, S. Kinet, N. Manel, C. Mongellaz, R. Prohaska, J.-L. Battini, J. Delaunay, M. Sitbon, N. Taylor, *Cell* **2008**, *132*, 1039–1048.
- [456] J.-M. Zen, J.-S. Tang, *Analytical Chemistry* **1995**, *67*, 1892–1895.
- [457] M. J. Bos, P. J. Koudstaal, A. Hofman, J. C. Witteman, M. M. Breteler, *Stroke* **2006**, *37*, 1503–1507.
- [458] D. J. Griffiths, Introduction to electrodynamics, **2005**.
- [459] R. Causon, *Journal of Chromatography B: Biomedical Sciences and Applications* **1997**, *689*, 175–180.
- [460] N. Murugan, M. B. Chan-Park, A. K. Sundramoorthy, *Journal of The Electrochemical Society* **2019**, *166*, B3163–B3170.
- [461] K. Income, N. Ratnarathorn, N. Khamchaiyo, C. Srisuvo, L. Ruckthong, W. Dungchai, *International journal of analytical chemistry* **2019**, *2019*.
- [462] R. Ahmad, N. Tripathy, N. K. Jang, G. Khang, Y.-B. Hahn, *Sensors and Actuators B: Chemical* **2015**, *206*, 146–151.
- [463] N. Chauhan, C. S. Pundir, *Analytical biochemistry* **2011**, *413*, 97–103.
- [464] Y. Zhao, X. Yan, Z. Kang, P. Lin, X. Fang, Y. Lei, S. Ma, Y. Zhang, *Microchimica Acta* **2013**, *180*, 759–766.
- [465] K. Jindal, M. Tomar, V. Gupta, *Analyst* **2013**, *138*, 4353–4362.

- [466] R. Ahmad, N. Tripathy, M.-S. Ahn, Y.-B. Hahn, *Scientific reports* **2017**, *7*, 46475.
- [467] A. Gutiérrez, M. L. Lozano, L. Galicia, N. F. Ferreyra, G. A. Rivas, *Electroanalysis* **2014**, *26*, 2191–2196.
- [468] M. Lin, H. Huang, Y. Liu, C. Liang, S. Fei, X. Chen, C. Ni, *Nanotechnology* **2013**, *24*, 065501.
- [469] S. M. Ghoreishi, M. Behpour, M. H. M. Fard, *Journal of Solid State Electrochemistry* **2012**, *16*, 179–189.
- [470] J. B. Raoof, R. Ojani, M. Amiri-Aref, M. Baghayeri, *Sensors and Actuators B: Chemical* **2012**, *166*, 508–518.
- [471] F. Li, J. Li, Y. Feng, L. Yang, Z. Du, *Sensors and actuators B: Chemical* **2011**, *157*, 110–114.
- [472] X. Zuo, N. Li, H. Zhang, *Journal of Materials Science* **2012**, *47*, 2731–2735.
- [473] X. Zuo, H. Zhang, N. Li, *Sensors and Actuators B: Chemical* **2012**, *161*, 1074–1079.
- [474] V. Ganesan, P. K. Rastogi, R. Gupta, M. T. Meredith, S. D. Minter, *Electrochimica Acta* **2013**, *105*, 31–39.
- [475] S. Pakapongpan, J. P. Mensing, D. Phokharatkul, T. Lomas, A. Tuantranont, *Electrochimica Acta* **2014**, *133*, 294–301.
- [476] C. Zhou, Y. Shi, J. Luo, L. Zhang, D. Xiao, *Journal of Materials Chemistry B* **2014**, *2*, 4122–4129.
- [477] Y. Liu, Z. Su, Y. Zhang, L. Chen, T. Gu, S. Huang, Y. Liu, L. Sun, Q. Xie, S. Yao, *Journal of Electroanalytical Chemistry* **2013**, *709*, 19–25.
- [478] A. Ambrosi, A. Morrin, M. R. Smyth, A. J. Killard, *Analytica Chimica Acta* **2008**, *609*, 37–43.

- [479] W. Kit-Anan, A. Olarnwanich, C. Sriprachuabwong, C. Karuwan, A. Tu-antranont, A. Wisitsoraat, W. Srituravanich, A. Pimpin, *Journal of Electroanalytical Chemistry* **2012**, *685*, 72–78.
- [480] H. Zhang, F. Huang, S. Xu, Y. Xia, W. Huang, Z. Li, *Electrochemistry communications* **2013**, *30*, 46–50.
- [481] C.-J. Weng, Y.-L. Chen, C.-M. Chien, S.-C. Hsu, Y.-S. Jhuo, J.-M. Yeh, C.-F. Dai, *Electrochimica Acta* **2013**, *95*, 162–169.
- [482] M. Govindasamy, V. Mani, S.-M. Chen, A. Sathiyar, J. P. Merlin, G. Boopathy, *Int. J. Electrochem. Sci* **2016**, *11*, e10814.
- [483] L. Shao, X. Wang, B. Yang, Q. Wang, Q. Tian, Z. Ji, J. Zhang, *Electrochimica Acta* **2017**, *255*, 286–297.
- [484] S. Majumder, B. Satpati, S. Kumar, S. Banerjee, *ACS Applied Nano Materials* **2018**, *1*, 3945–3955.
- [485] T. Skotheim, *Handbook of Conducting Polymers [Vol 1-2]*. **1986**.
- [486] P. Andersson, R. Forchheimer, P. Tehrani, M. Berggren, *Advanced Functional Materials* **2007**, *17*, 3074–3082.
- [487] Y. Liu, T. Cui, *Solid-state electronics* **2005**, *49*, 445–448.
- [488] A. Habib, C. Ondeck, P. Chaudhary, M. Bockstaller, M. McHenry, *Journal of Applied Physics* **2008**, *103*, 07A307.
- [489] Y. Wang, S. Gao, W.-H. Ye, H. S. Yoon, Y.-Y. Yang, *Nature materials* **2006**, *5*, 791–796.
- [490] S. Kayal, R. V. Ramanujan, *Journal of nanoscience and nanotechnology* **2010**, *10*, 5527–5539.
- [491] C. He, D. Liu, W. Lin, *ACS nano* **2015**, *9*, 991–1003.
- [492] K. C. Kwon, J. H. Ryu, J.-H. Lee, E. J. Lee, I. C. Kwon, K. Kim, J. Lee, *Advanced materials* **2014**, *26*, 6436–6441.

- [493] L. Rodriguez-Lorenzo, L. Fabris, R. A. Alvarez-Puebla, *Analytica chimica acta* **2012**, *745*, 10–23.
- [494] M. Kahraman, E. R. Mullen, A. Korkmaz, S. Wachsmann-Hogiu, *Nanophotonics* **2017**, *6*, 831–852.
- [495] A. S. De Silva Indrasekara, L. Fabris, *Bioanalysis* **2015**, *7*, 263–278.
- [496] L. Fabris, *ChemNanoMat* **2016**, *2*, 249–258.
- [497] Y. Zhang, S. Schlücker in *Confocal Raman Microscopy*, Springer, **2018**, pp. 347–379.
- [498] J. Feng, L. Xu, G. Cui, X. Wu, W. Ma, H. Kuang, C. Xu, *Biosensors and Bioelectronics* **2016**, *81*, 138–142.
- [499] A. Li, L. Tang, D. Song, S. Song, W. Ma, L. Xu, H. Kuang, X. Wu, L. Liu, X. Chen, et al., *Nanoscale* **2016**, *8*, 1873–1878.
- [500] V. L. Schmit, R. Martoglio, B. Scott, A. D. Strickland, K. T. Carron, *Journal of the American Chemical Society* **2012**, *134*, 59–62.
- [501] Y. Zhu, H. Kuang, L. Xu, W. Ma, C. Peng, Y. Hua, L. Wang, C. Xu, *Journal of Materials Chemistry* **2012**, *22*, 2387–2391.
- [502] G. Bodelón, V. Montes-Garca, V. López-Puente, E. H. Hill, C. Hamon, M. N. Sanz-Ortiz, S. Rodal-Cedeira, C. Costas, S. Celiksoy, I. Pérez-Juste, et al., *Nature materials* **2016**, *15*, 1203–1211.
- [503] L. Xu, H. Yin, W. Ma, H. Kuang, L. Wang, C. Xu, *Biosensors and Bioelectronics* **2015**, *67*, 472–476.
- [504] X. Wu, L. Tang, W. Ma, L. Xu, L. Liu, H. Kuang, C. Xu, *RSC Advances* **2015**, *5*, 81802–81807.
- [505] W. Ma, M. Sun, L. Xu, L. Wang, H. Kuang, C. Xu, *Chemical communications* **2013**, *49*, 4989–4991.

- [506] A. I. Radu, O. Ryabchykov, T. W. Bocklitz, U. Huebner, K. Weber, D. Cialla-May, J. Popp, *Analyst* **2016**, *141*, 4447–4455.
- [507] S. Patze, U. Huebner, F. Liebold, K. Weber, D. Cialla-May, J. Popp, *Analytica chimica acta* **2017**, *949*, 1–7.